NUMERICAL SOLUTIONS OF THE NAVIER-STOKES EQUATIONS FOR THE SUPERSONIC LAMINAR FLOW OVER A TWO-DIMENSIONAL COMPRESSION CORNER

by James E. Carter

Langley Research Center
Hampton, Va. 23365

NATIONAL AERONAUTICS AND SPACE ADMINISTRATION • WASHINGTON, D. C. • JULY 1972

1. Report No. NASA TR R-385	2. Government Accession No.	3. Recipient's Catalog No.
4. Title and Subtitle NUMERICAL SOLUTIONS OF THE NAVIER-STOKES EQUATIONS FOR THE SUPERSONIC LAMINAR FLOW OVER A TWO-DIMENSIONAL COMPRESSION CORNER		5. Report Date July 1972 6. Performing Organization Code
7. Author(s) James E. Carter		8. Performing Organization Report No. L-8306
9. Performing Organization Name and Address NASA Langley Research Center Hampton, Va. 23365		10. Work Unit No. 136-13-05-01 11. Contract or Grant No.
12. Sponsoring Agency Name and Address National Aeronautics and Space Administration Washington, D.C. 20546		13. Type of Report and Period Covered Technical Report 14. Sponsoring Agency Code

15. Supplementary Notes The information presented herein is based in part upon a thesis entitled "Numerical Solution of the Supersonic, Laminar Flow Over a Two-Dimensional Compression Corner" submitted in partial fulfillment of the requirements for the degree of Doctor of Philosophy in Aerospace Engineering, Virginia Polytechnic Institute and State University, Blacksburg, Virginia, August 1971.

16. Abstract

Numerical solutions have been obtained for the supersonic, laminar flow over a two-dimensional compression corner. These solutions were obtained as steady-state solutions to the unsteady Navier-Stokes equations using the finite-difference method of Brailovskaya, which has second-order accuracy in the spatial coordinates. Good agreement was obtained between the computed results and the wall pressure distributions measured experimentally by Lewis, Kubota, and Lees for Mach numbers of 4 and 6.06, and respective Reynolds numbers, based on free-stream conditions and the distance from the leading edge to the corner, of 6.8×10^4 and 1.5×10^5. In those calculations, as well as in others, sufficient resolution was obtained to show the streamline pattern in the separation bubble. Upstream boundary conditions to the compression-corner flow were provided by numerically solving the unsteady Navier-Stokes equations for the flat-plate flow field, beginning at the leading edge. The compression-corner flow field was enclosed by a computational boundary with the unknown boundary conditions supplied by extrapolation from internally computed points. Numerical tests were performed to deduce that the magnitude of the errors introduced by the extrapolation was small.

Calculations were made to show the effect of ramp angle and wall suction on the interaction flow field. The pressure distributions obtained in the present calculations, including a case of incipient separation, were plotted together by using the free-interaction scaling of Stewartson and Williams. A good correlation of the numerical results was found, but only fair agreement was found between this correlation and the universal pressure distribution found numerically by Stewartson and Williams.

17. Key Words (Suggested by Author(s))	18. Distribution Statement
Navier-Stokes equations Numerical analysis Shock-boundary-layer interaction Supersonic flow	Unclassified – Unlimited

19. Security Classif. (of this report)	20. Security Classif. (of this page)	21. No. of Pages	22. Price*
Unclassified	Unclassified	81	$3.00

*For sale by the National Technical Information Service, Springfield, Virginia 22151

CONTENTS

NUMERICAL SOLUTIONS OF THE NAVIER-STOKES EQUATIONS FOR THE SUPERSONIC LAMINAR FLOW OVER A TWO-DIMENSIONAL COMPRESSION CORNER*

By James E. Carter
Langley Research Center

SUMMARY

Numerical solutions have been obtained for the supersonic, laminar flow over a two-dimensional compression corner. These solutions were obtained as steady-state solutions to the unsteady Navier-Stokes equations using the finite-difference method of Brailovskaya, which has second-order accuracy in the spatial coordinates. Good agreement was obtained between the computed results and the wall pressure distributions measured experimentally by Lewis, Kubota, and Lees for Mach numbers of 4 and 6.06, and respective Reynolds numbers, based on free-stream conditions and the distance from the leading edge to the corner, of 6.8×10^4 and 1.5×10^5. In those calculations, as well as in others, sufficient resolution was obtained to show the streamline pattern in the separation bubble. Upstream boundary conditions to the compression-corner flow were provided by numerically solving the unsteady Navier-Stokes equations for the flat-plate flow field, beginning at the leading edge. The compression-corner flow field was enclosed by a computational boundary with the unknown boundary conditions supplied by extrapolation from internally computed points. Numerical tests were performed to deduce that the magnitude of the errors introduced by the extrapolation was small.

Calculations were made to show the effect of ramp angle and wall suction on the interaction flow field. The pressure distributions obtained in the present calculations, including a case of incipient separation, were plotted together by using the free-interaction scaling of Stewartson and Williams. A good correlation of the numerical results was found, but only fair agreement was found between this correlation and the universal pressure distribution found numerically by Stewartson and Williams.

---

* The information presented herein is based in part upon a thesis entitled "Numerical Solution of the Supersonic, Laminar Flow Over a Two-Dimensional Compression Corner" submitted in partial fulfillment of the requirements for the degree of Doctor of Philosophy in Aerospace Engineering, Virginia Polytechnic Institute and State University, Blacksburg, Virginia, August 1971.

INTRODUCTION

A problem that has interested fluid dynamicists for a number of years is the supersonic flow over a flat plate followed by a ramp. The pressure rise generated by the ramp extends upstream along the flat plate and results in a complex interaction between the boundary layer and the outer inviscid stream. This interaction leads to flow separation for certain ranges of the Mach number, Reynolds number, and ramp angle. The purpose of the present investigation was to obtain numerical solutions to the finite-difference form of the Navier-Stokes equations for the laminar flow over a two-dimensional compression corner. In addition to its theoretical interest, this problem is of practical importance in predicting the pressure and heat loads in a wing-flap juncture on a supersonic aircraft. When flow separation occurs, reduced flap effectiveness results, and in the reattachment region the surface heating may become severe.

A schematic diagram of the supersonic flow over a compression corner is shown in figure 1. The adverse pressure gradient generated by the ramp thickens the approaching boundary layer. The inner part of the boundary layer near the surface may have an insufficient total pressure and thus may separate from the surface since it cannot overcome the adverse pressure gradient. The separated boundary layer now becomes a free shear layer external to a steady, recirculating inner flow near the corner. The boundary between the shear layer and recirculation region is logically referred to as a dividing streamline. Farther downstream the shear layer impinges on the ramp in the reattachment region; the flow in the boundary layer then continues to accelerate until the boundary layer reaches a minimum thickness at the "neck." Downstream of the neck, the boundary layer returns to a normal state of weak interaction at the new Mach number.

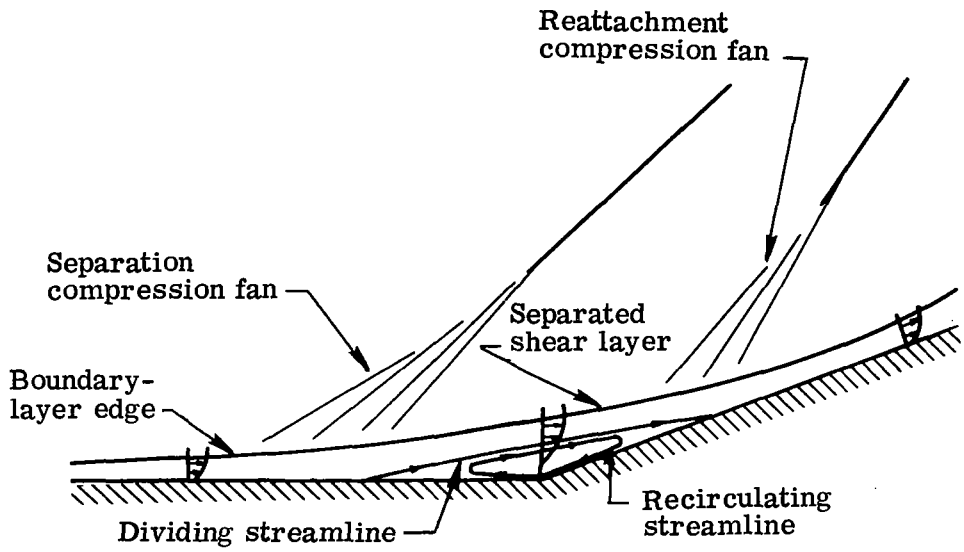

Figure 1.- Schematic diagram of a supersonic flow field in a compression corner.

A direct method of including the upstream influence in flow fields involving large interaction between the viscous and inviscid flow is to treat the full Navier-Stokes equations. Treatment of the Navier-Stokes equations avoids the uniqueness questions inherent in the boundary-layer interaction approach. The accuracy is probably improved since, for example, a solution of the Navier-Stokes equations is required in the immediate vicinity of a sharp corner as mentioned by Van Dyke (ref. 1). In addition, numerical solutions to the Navier-Stokes equations, although still limited by computer size and speed, serve as benchmark solutions for comparison with approximate but more expedient methods.

In the present investigation, the unsteady Navier-Stokes equations are solved by the explicit finite-difference scheme of Brailovskaya (ref. 2). Including the unsteady terms in the Navier-Stokes equations results in a parabolic system of partial differential equations and in a well-posed, initial-value—boundary-value problem. As indicated by Crocco (ref. 3), the inclusion of time in the equations allows the solution to progress naturally from an initial guess to an asymptotic state, which is the solution to the steady equations. In the present investigation, it was assumed that a steady solution exists for the compression-corner flow field.

BACKGROUND

Boundary-Layer Methods

Previous theoretical treatments of this problem have been made with the boundary-layer equations to describe the separation of a supersonic flow, and these methods are applicable to the compression-corner flow field. Three of these methods are capable of obtaining a solution in the reattachment region as well as in the separation region. These three methods are the integral methods of Lees and Reeves (ref. 4), and Nielsen, Goodwin, and Kuhn (ref. 5), and the finite-difference method of Reyhner and Flügge-Lotz (ref. 6). Although these methods differ in detail, their success in this problem is based on several features which they have in common, and hence they will be discussed collectively. Numerical comparisons of these methods with available experimental data have been made by Murphy (ref. 7) and, to a lesser extent, by Hill (ref. 8).

Standard procedures for solving the boundary-layer equations utilize forward-marching techniques with a known pressure distribution. Such a procedure is not applicable to the compression-corner flow field since the pressure distribution is not known a priori. As a result, these methods make repeated iterations in order to obtain a unique solution which properly accounts for the upstream influence of the corner.

This iterative procedure is initiated at an arbitrary point upstream of the corner by introducing either a small increment in the pressure, as in the methods of Lees and Reeves and that of Nielsen et al. or by subjecting the boundary layer to a small adverse

pressure gradient, as in the method of Reyhner and Flügge-Lotz. The resulting pressure distribution is computed from the Prandtl-Meyer relation which relates the pressure to the local flow inclination at the boundary-layer edge. Both techniques initiate an amplifying process. As the pressure increases, the boundary-layer thickness and slope increases, and, in turn, causes the pressure to increase further by an amount given by the Prandtl-Meyer equation. This process culminates in separation of the flow which relieves the pressure gradient, and therefore the downstream flow approaches a constant-pressure region (a plateau).

Once the plateau region is reached, the disturbance that induced the separation (for example, an incident shock or compression ramp) is introduced. An infinite family of solutions can be found by varying the strength of the disturbance (alternately, the disturbance strength can be held constant and the upstream point of interaction varied). Uniqueness is established by imposing downstream compatibility conditions and solving iteratively until these conditions are satisfied. The downstream compatibility condition in the methods of Nielsen et al. and Reyhner and Flügge-Lotz is that $\frac{dp}{dx} = \frac{d^2p}{dx^2} = 0$ at the same point, whereas in the method of Lees and Reeves the downstream solution is required to approach the flat-plate solution.

A somewhat different approach has been taken by Stewartson and Williams (ref. 9), who found a universal solution to the boundary-layer equations for the region from the start of the interaction to a point just downstream of separation. The existence of a universal solution was suggested by the pressure correlation discovered experimentally by Chapman, Kuehn, and Larson (ref. 10) and has been verified more recently by Lewis, Kubota, and Lees (ref. 11). They observed that in a supersonic flow field, the initial pressure rise through separation to the plateau value was independent of the details of the disturbing mechanism (and hence is referred to as a "free interaction"), whether it be, for example, an incident shock, a forward-facing step, or a ramp. Stewartson and Williams use the method of matched asymptotic expansions to show that the length scale of the free-interaction region is $R_{\infty,x_0}^{-3/8}$ where R_{∞,x_0} is the Reynolds number based on free-stream conditions and the length from the leading edge to the start of the interaction. This scaling was the same as that found earlier by Gadd (ref. 12) by a more approximate method. From the expansion procedure it becomes apparent that an inner boundary layer of constant density and large velocity perturbation is the key feature of the free-interaction zone. The idea of an inner boundary layer, that is, a region where the disturbances to the viscous forces are comparable with the disturbances to the inertial forces, was originated by Lighthill (ref. 13) in studying the interaction between the boundary layer and a weak shock. Stewartson and Williams obtained a universal pressure distribution for the free-interaction region by solving the incompressible boundary-layer equations for the inner

region subjected to novel boundary condition. Only fair agreement was obtained between their theoretical result and an experimental wall pressure distribution obtained by Chapman et al. (ref. 10).

Numerical Solution of Navier-Stokes Equations

In the last several years the volume of literature has increased rapidly on the solution of various problems by treating the finite-difference form of the unsteady Navier-Stokes equations. Recently, Cheng (ref. 14) reviewed the literature and reported most of the investigations which have been made. Several numerical investigations have been made for the flow over a rearward-facing step. Allen and Cheng (ref. 15) obtained numerical solutions for this flow field for a Reynolds number, based on the base half-height and the inflow conditions, of less than 1000, and a Mach number range from 2 to 4. The entire flow field was enclosed by a computational boundary, and the flow conditions were either known or had to be approximated along this boundary. Allen and Cheng used a modification of the explicit, time-dependent method introduced by Brailovskaya (ref. 2). Because of the low Reynolds number and low value of density which occurs in the recirculation region behind the step, they modified the Brailovskaya scheme to eliminate the dependence of the time step on the kinematic viscosity coefficient. This work has been extended by Ross and Cheng (ref. 16) to include variable viscosity and base injection. The results obtained by Allen and Cheng and by Ross and Cheng appear to be qualitatively correct since the characteristic features of the base flow region are evident. The quantitative results are yet to be verified by experiment since no experiments have been performed for the low Reynolds numbers used in these calculations.

Roache and Mueller (ref. 17) reported calculations for both compressible and incompressible flow over a rearward-facing step. They used the first-order windward difference scheme which is known to suffer from a diffusive truncation error. Unfortunately, it is difficult to assess the effects of this truncation error in a complicated flow-field calculation. Carter (ref. 18) made numerical studies of Burger's equation, which is a simple one-dimensional model of the Navier-Stokes equations, and showed that the windward scheme is less accurate than either the Brailovskaya or a Lax-Wendroff* difference scheme.

Victoria and Steiger (ref. 19) extended the original Crocco finite-difference scheme to two dimensions and solved the unsteady Navier-Stokes equations for the supersonic flow over a rearward-facing step. Good agreement was obtained between the numerical results and those found experimentally by Batt and Kubota (ref. 20).

---

* A Lax-Wendroff difference technique is referred to here as an explicit method which has temporal and spatial truncation errors of second order.

MacCormack (ref. 21) has made calculations for the solution of a shock impinging on a laminar flat-plate boundary layer. In obtaining solutions to this problem, he modified a second-order finite-difference scheme which he had introduced earlier (see MacCormack (ref. 22)) for the problem of hypervelocity impact cratering. MacCormack's original method is a two-step Lax-Wendroff difference technique which alternately uses forward and backward differences for the convection terms. This scheme was modified in the incident-shock problem by splitting the governing equations into two sets – one for the x-derivatives and one for the y-derivatives. The advantage of the split system is that the computation proceeds with larger time increments since the stability criterion is less stringent. By using the split system, the required time step is the minimum time increment of that found by applying the usual Courant-Friedrichs-Lewy conditions individually to the x and y subset of equations.

MacCormack presented results for an incident oblique shock onto a flat boundary layer at $M_\infty = 2.0$ for which Hakkinen et al. (ref. 23) have made experimental measurements. The Reynolds number at the intersection of the shock wave and the flat plate, based on the length from the leading edge and free-stream conditions, was approximately 3×10^5. In general, the agreement between predicted and measured wall pressure and skin-friction distributions is good, although the x-grid spacing in the separation region is too coarse for adequate resolution.

SYMBOLS

C constant of proportionality in linear viscosity law defined in equation (34)

C_f skin-friction coefficient, $\dfrac{\tau}{\frac{1}{2}\rho_\infty u_\infty^2}$

$C_{f,o}$ skin-friction coefficient, $\dfrac{\tau}{\frac{1}{2}\rho_o u_o^2}$

$C_{p,o}$ pressure coefficient, $\dfrac{p - p_o}{\frac{1}{2}\rho_o u_o^2}$

c speed of sound

c_p specific heat at constant pressure

c_v specific heat at constant volume

E total energy

e	internal energy
G	amplification matrix
g	eigenvalue of amplification matrix G
k	thermal conductivity
j,k	indices for x- and y-direction, respectively
L	distance along flat plate from leading edge used in reference Reynolds number
M	Mach number
N_{Pr}	Prandtl number
P	Curle correlation pressure
p	pressure
$\tilde{p}_2$	Stewartson and Williams' correlation pressure
$p_{t,2}$	total pressure behind a normal shock
R	gas constant in equation of state
R_Δ	Reynolds number, $\frac{\rho_\infty u_\infty \Delta}{\mu_\infty}$
$R_{\infty,L}$	Reynolds number, $\frac{\rho_\infty u_\infty L}{\mu_\infty}$
$R_{\infty,x}$	Reynolds number, $\frac{\rho_\infty u_\infty x}{\mu_\infty}$
R_{∞,x_c}	Reynolds number, $\frac{\rho_\infty u_\infty x_c}{\mu_\infty}$
R_{o,x_o}	Reynolds number, $\frac{\rho_o u_o x_o}{\mu_o}$

S_o	empirical constant in Sutherland viscosity law, for air $S = 198.6^{o}$ R
T	temperature
$\overline{T}_{aw}$	constant adiabatic wall temperature given in equation (38)
$T_{o,\infty}$	free-stream stagnation temperature
t	time
Δt	time increment
u	velocity component parallel to flat plate
u',v'	velocity components parallel and normal to ramp
$\overline{V}_{\infty}$	rarefaction parameter
v	velocity component normal to flat plate
X	skewed coordinate parallel to ramp; Curle correlation length
$\tilde{X}$	Stewartson and Williams' correlation length
x,y	Cartesian coordinates parallel and normal to flat plate
Δx	distance between two successive grid points in x-direction
Y	skewed coordinate normal to flat plate
Δy	distance between two successive grid points in y-direction
α	ramp angle
β_D	angle between dividing streamline and wall

β_u angle between $u = 0$ locus and wall

γ ratio of specific heats, c_p/c_v

Δ denotes either Δx or Δy

δ boundary-layer thickness

δ^* displacement thickness defined in equation (37)

μ viscosity coefficient

μ_B bulk viscosity coefficient

ρ density

τ shear stress

φ dependent variable

$\bar{\chi}_\infty$ weak-interaction parameter, $M_\infty^3\sqrt{\frac{C_\infty}{R_{\infty,x}}}$

ψ nondimensional stream function

Subscripts:

c corner

e edge of boundary layer

o start of compression-corner interaction

r reference

w wall

∞ free stream

Superscripts:

*	temporarily used to denote nondimensional quantities
n	number of time cycles

METHOD

Governing Equations

The governing equations that describe the motion of a viscous heat-conducting fluid are the Navier-Stokes equations which are given as follows for two-dimensional unsteady flow with respect to the Cartesian coordinates, x and y.

Continuity:

$$\frac{\partial \rho}{\partial t} + \frac{\partial \rho u}{\partial x} + \frac{\partial \rho v}{\partial y} = 0 \tag{1}$$

x-momentum:

$$\frac{\partial \rho u}{\partial t} + \frac{\partial \left(p + \rho u^2\right)}{\partial x} + \frac{\partial \rho uv}{\partial y} = \frac{\partial \tau_{xx}}{\partial x} + \frac{\partial \tau_{xy}}{\partial y} \tag{2}$$

y-momentum:

$$\frac{\partial \rho v}{\partial t} + \frac{\partial \rho uv}{\partial x} + \frac{\partial \left(p + \rho v^2\right)}{\partial y} = \frac{\partial \tau_{yx}}{\partial x} + \frac{\partial \tau_{yy}}{\partial y} \tag{3}$$

Energy:

$$\frac{\partial E}{\partial t} + \frac{\partial u(E + p)}{\partial x} + \frac{\partial v(E + p)}{\partial y} = \frac{\partial}{\partial x}\left(k \frac{\partial T}{\partial x}\right) + \frac{\partial}{\partial y}\left(k \frac{\partial T}{\partial y}\right) + \frac{\partial}{\partial x}\left(u\tau_{xx} + v\tau_{xy}\right) + \frac{\partial}{\partial y}\left(u\tau_{xy} + v\tau_{yy}\right) \tag{4}$$

where

$$\left.\begin{aligned} \tau_{xx} &= 2\mu \frac{\partial u}{\partial x} + \left(\mu_B - \frac{2}{3}\mu\right)\left(\frac{\partial u}{\partial x} + \frac{\partial v}{\partial y}\right) \\ \tau_{xy} &= \tau_{yx} = \mu\left(\frac{\partial u}{\partial y} + \frac{\partial v}{\partial x}\right) \end{aligned}\right\}$$

(Equations continued on next page)

$$\left.\begin{aligned} \tau_{yy} &= 2\mu \frac{\partial v}{\partial y} + \left(\mu_B - \frac{2}{3}\mu\right)\left(\frac{\partial u}{\partial x} + \frac{\partial v}{\partial y}\right) \\ E &= \rho\left(e + \frac{u^2 + v^2}{2}\right) \end{aligned}\right\} \tag{5}$$

In addition to these equations which express the conservation of mass, momentum, and energy, it is necessary to include a state equation which, for a perfect gas, is given by

$$p = \rho RT \tag{6}$$

The viscosity coefficient is a function of temperature and is adequately approximated by Sutherland's semiempirical equation

$$\frac{\mu}{\mu_r} = \frac{T_r + S_o}{T + S_o}\left(\frac{T}{T_r}\right)^{3/2} \tag{7}$$

where the constant S_o has been experimentally determined to be 198.6° R for air.

From equations (1) to (7) six equations in the six unknowns, u, v, T, ρ, p, and μ are provided if the bulk viscosity coefficient μ_B is set equal to zero. The effects of the bulk viscosity coefficient are important in sound propagation and shock-wave structure, as discussed by Vincenti and Kruger (ref. 24). In the present investigation it is neglected since the grid spacing used in the region of the shock is too coarse to allow resolution of the shock structure.

The variables in equations (1) to (7) may be nondimensionalized as follows:

$$\left.\begin{aligned} x^* &= \frac{x}{L} & v^* &= \frac{v}{u_\infty} & T^* &= \frac{c_p T}{u_\infty^2} \\ y^* &= \frac{y}{L} & \rho^* &= \frac{\rho}{\rho_\infty} & E^* &= \frac{E}{\rho_\infty u_\infty^2} \\ u^* &= \frac{u}{u_\infty} & p^* &= \frac{p}{\rho_\infty u_\infty^2} & \mu^* &= \frac{\mu}{\mu_\infty} \end{aligned}\right\} \tag{8}$$

The resulting system of nondimensionalized differential equations may be conveniently written in vector form as

$$\frac{\partial w^*}{\partial t^*} + \frac{\partial F^*}{\partial x^*} + \frac{\partial G^*}{\partial y^*} = S^* \tag{9}$$

where

$$w^* = \begin{Bmatrix} \rho^* \\ \rho^* u^* \\ \rho^* v^* \\ E^* \end{Bmatrix} \qquad F^* = \begin{Bmatrix} \rho^* u^* \\ p^* + \rho^* u^{*2} \\ \rho^* u^* v^* \\ u^*(E^* + p^*) \end{Bmatrix} \qquad G^* = \begin{Bmatrix} \rho^* v^* \\ \rho^* u^* v^* \\ p^* + \rho^* v^{*2} \\ v^*(E^* + p^*) \end{Bmatrix} \tag{10}$$

$$S^* = \frac{1}{R_{\infty,L}} \begin{Bmatrix} 0 \\ \dfrac{\partial \tau_{xx}^*}{\partial x^*} + \dfrac{\partial \tau_{xy}^*}{\partial y^*} \\ \dfrac{\partial \tau_{xy}^*}{\partial x^*} + \dfrac{\partial \tau_{yy}^*}{\partial y^*} \\ \dfrac{1}{N_{Pr}} \left[\dfrac{\partial}{\partial x^*} \left(\mu^* \dfrac{\partial T^*}{\partial x^*} \right) + \dfrac{\partial}{\partial y^*} \left(\mu^* \dfrac{\partial T^*}{\partial y^*} \right) \right] + \dfrac{\partial}{\partial x^*} \left(u^* \tau_{xx}^* + v^* \tau_{xy}^* \right) \\ + \dfrac{\partial}{\partial y^*} \left(u^* \tau_{xy}^* + v^* \tau_{yy}^* \right) \end{Bmatrix} \tag{11}$$

and

$$\left.\begin{aligned} \tau_{xx}^* &= 2\mu^* \frac{\partial u^*}{\partial x^*} - \frac{2\mu^*}{3} \left(\frac{\partial u^*}{\partial x^*} + \frac{\partial v^*}{\partial y^*} \right) \\ \tau_{xy}^* &= \mu^* \left(\frac{\partial u^*}{\partial y^*} + \frac{\partial v^*}{\partial x^*} \right) \\ \tau_{yy}^* &= 2\mu^* \frac{\partial v^*}{\partial y^*} - \frac{2\mu^*}{3} \left(\frac{\partial u^*}{\partial x^*} + \frac{\partial v^*}{\partial y^*} \right) \end{aligned}\right\} \tag{12}$$

with the Reynolds number $R_{\infty,L} = \dfrac{\rho_\infty u_\infty L}{\mu_\infty}$ and Prandtl number $N_{Pr} = \dfrac{c_p \mu}{k}$. In the present analysis, except as otherwise noted, the Prandtl number is maintained at a constant value of 0.72, which is the experimentally determined value for diatomic gases at moderate temperatures. The nondimensionalized Sutherland relation becomes

$$\mu^* = \left[\frac{\dfrac{1}{(\gamma - 1)M_\infty^2} + S^*}{T^* + S^*} \right] \left[(\gamma - 1) M_\infty^2 T^* \right]^{3/2} \tag{13}$$

where M_∞ is the free-stream Mach number and the constant S^* is given by the equation

$$S^* = \frac{S_0}{(\gamma - 1)M_\infty^2 T_\infty} \tag{14}$$

It is observed that when the Sutherland viscosity is used, the dimensional free-stream static temperature is not eliminated from the governing equations and therefore must be specified in each calculation. The nondimensionalized state equation becomes

$$p^* = \frac{\gamma - 1}{\gamma} \rho^* T^* \tag{15}$$

At this point the asterisk notation will be dropped with the understanding that all quantities are nondimensional unless otherwise indicated.

Finite-Difference Technique

The finite-difference scheme chosen in the present investigation is the two-step explicit scheme proposed by Brailovskaya (ref. 2). Comparisons of steady-state solutions with solutions to Burger's equation (model of the Navier-Stokes equations) are presented by Carter (ref. 18) between the Brailovskaya scheme, which has a truncation error of $0(\Delta t + \Delta x^2)$, and a Lax-Wendroff scheme with truncation error of $0(\Delta t^2 + \Delta x^2)$. Both schemes yield results of comparable accuracy near the asymptotic steady-state solution. Additional comparisons are presented by Carter (ref. 18) between solutions of the Navier-Stokes equations for a flat-plate flow field using the Brailovskaya scheme, and solutions obtained by Thommen (ref. 25) using a Lax-Wendroff scheme. Only small differences were found and hence it was concluded that these two schemes result in comparable accuracy for obtaining steady solutions to the Navier-Stokes equations. The Brailovskaya scheme was chosen since the same grid is used for both time steps and therefore this scheme should be more efficient. In addition, variable grid was used for some of the calculations in the present investigation, and the Brailovskaya scheme is easier to modify to take noncentral differences into account.

Application of the Brailovskaya scheme to equation (9) with $t = n\,\Delta t$, $x = j\,\Delta x$, and $y = k\,\Delta y$ results in the following difference equations where the grid spacing has been assumed to be constant in the x- and y-directions:

$$\left.\begin{aligned}
\frac{\bar{w}_{j,k}^{n+1} - w_{j,k}^{n}}{\Delta t} &= -\left(\frac{F_{j+1,k}^{n} - F_{j-1,k}^{n}}{2\,\Delta x} + \frac{G_{j,k+1}^{n} - G_{j,k-1}^{n}}{2\,\Delta y} - S_{j,k}^{n}\right) + 0(\Delta t + \Delta x^2 + \Delta y^2) \\
\frac{w_{j,k}^{n+1} - w_{j,k}^{n}}{\Delta t} &= -\left(\frac{\bar{F}_{j+1,k}^{n+1} - \bar{F}_{j-1,k}^{n+1}}{2\,\Delta x} + \frac{\bar{G}_{j,k+1}^{n+1} - \bar{G}_{j,k-1}^{n+1}}{2\,\Delta y} - S_{j,k}^{n}\right) + 0(\Delta t + \Delta x^2 + \Delta y^2)
\end{aligned}\right\} \tag{16}$$

In the first step, a temporary value of w $\left(\text{denoted by } \bar{w}^{n+1}_{j,k}\right)$ is calculated at the new time step; this value is improved in the second step by reevaluating the convection term with the temporary values of w, the stress term S being repeated from the first step. The usual linearized stability analysis suggests that this two-step scheme is conditionally stable regardless of the magnitude of the Reynolds number. At the completion of each step the desired unknowns are computed from the vector w by the following equations:

$$\left.\begin{aligned} \rho &= w_1 \\ u &= \frac{w_2}{w_1} \\ v &= \frac{w_3}{w_1} \\ T &= \gamma\left\{\frac{w_4}{w_1} - \frac{1}{2}\left[\left(\frac{w_2}{w_1}\right)^2 + \left(\frac{w_3}{w_1}\right)^2\right]\right\} \end{aligned}\right\} \tag{17}$$

where the subscripts denote the elements of the column vector w. In equations (16) the viscous stress and heat conduction derivatives are contained in the term $S^n_{j,k}$. In the present investigation these terms were treated in their expanded form and approximated by central-difference quotients of second-order accuracy. For example, the shear term was approximated for constant grid spacing by

$$\left[\frac{\partial}{\partial y}\left(\mu\frac{\partial u}{\partial y}\right)\right]_{j,k} = \left(\frac{\partial \mu}{\partial y}\frac{\partial u}{\partial y} + \mu\frac{\partial^2 u}{\partial y^2}\right)_{j,k}$$

$$= \left(\frac{\mu_{j,k+1} - \mu_{j,k-1}}{2\,\Delta y}\right)\left(\frac{u_{j,k+1} - u_{j,k-1}}{2\,\Delta y}\right) + \mu_{j,k}\left(\frac{u_{j,k+1} - 2u_{j,k} + u_{j,k-1}}{\Delta y^2}\right) + 0(\Delta y^2) \tag{18}$$

An alternate procedure for this term is that used by Brailovskaya (ref. 2) and is written as

$$\left[\frac{\partial}{\partial y}\left(\mu\frac{\partial u}{\partial y}\right)\right]_{j,k} = \frac{\left(\mu\frac{\partial u}{\partial y}\right)_{j,k+1/2} - \left(\mu\frac{\partial u}{\partial y}\right)_{j,k-1/2}}{\Delta y}$$

$$= \frac{\left(\mu_{j,k} + \mu_{j,k+1}\right)\left(u_{j,k+1} - u_{j,k}\right) - \left(\mu_{j,k} + \mu_{j,k-1}\right)\left(u_{j,k} - u_{j,k-1}\right)}{2\,\Delta y^2} + 0(\Delta y^2) \tag{19}$$

These approximations both result in the same order of truncation error; however, the expanded form (eq. (18)) is more efficient to use with variable grid and the skewed coordinate transformation which is used in the present investigation.

The Brailovskaya finite-difference scheme is conditionally stable since the maximum time increment by which the solution may be advanced at any time step is dependent on the spatial grid size as well as the solution itself. An approximate analysis which yields an estimate of the maximum time increment is that of von Neumann which consists of examining the linearized difference equations for the amplification of short wavelength disturbances of small amplitude. Allen (ref. 26) presented a von Neumann stability analysis, based on a technique given by Richtmyer (ref. 27), for the Brailovskaya scheme applied to the inviscid equations. The resulting stability criterion was found to be the CFL (Courant-Friedrichs-Lewy) limit which is

$$\Delta t \leqq \frac{1}{\frac{|u|}{\Delta x} + \frac{|v|}{\Delta y} + c\sqrt{\frac{1}{\Delta x^2} + \frac{1}{\Delta y^2}}} \tag{20}$$

This restriction on the value of Δt is a necessary condition for stability of the finite-difference solution of the Navier-Stokes equations if the calculations are made in inviscid regions. Near the body surface where the viscous effects are predominant, a stability limit on Δt can be found which results from considering the viscous terms and is

$$\Delta t \leqq \frac{0.5 N_{Pr} R_{\infty,L}}{\gamma\left(\frac{\mu}{\rho}\right)\left(\frac{1}{\Delta x^2} + \frac{1}{\Delta y^2}\right)} \tag{21}$$

The details of the analysis which yields these stability criteria are presented in appendix A. In performing the calculations, the minimum value of Δt given by equations (20) and (21) was used.

Variable Grid

Many flow fields contain regions which differ significantly in their characteristic lengths, and therefore difficulty is encountered in attempting to solve such flow fields with a uniform grid mesh. In the present investigation this particular problem arose in solving for the supersonic flow over a flat plate. As the distance x increases from the leading edge, the boundary layer thickens like $x^{1/2}$, whereas the region bounded by the shock wave grows approximately like x. The net effect is that with increasing x, the viscous effects are confined to a smaller fraction of the distance from the wall to the shock wave. Since the variations in the inviscid shock layer are much less than those in the boundary layer, it is necessary to use a variable grid in order to attain maximum efficiency with the finite-difference mesh.

A variable grid can be established either by transforming the independent variables with a suitable stretching function or by varying the grid in the physical plane. Skoglund

et al. (ref. 28) used a logarithmic coordinate transformation to open the grid in the region away from the intersection of an incident shock wave with a flat-plate boundary layer. Cebeci, Smith, and Mosinskis (ref. 29) expanded the grid at a constant rate away from the wall in their analysis of the turbulent boundary layer flowing over the body surface. In the present case, the latter technique of imposing a variable grid was used and the following difference quotients are easily derived from Taylor series along with their respective truncation errors:

$$\left.\frac{\partial \varphi}{\partial x}\right|_{j,k} = \frac{\Delta x_2^2 \varphi_{j+1,k} - \Delta x_1^2 \varphi_{j-1,k} + \left(\Delta x_1^2 - \Delta x_2^2\right)\varphi_{j,k}}{\Delta x_1 \, \Delta x_2 \left(\Delta x_1 + \Delta x_2\right)}$$

$$- \frac{\Delta x_1 \, \Delta x_2}{6} \left.\frac{\partial^3 \varphi}{\partial x^3}\right|_{j,k} + 0(\Delta^3) \tag{22}$$

$$\left.\frac{\partial^2 \varphi}{\partial x^2}\right|_{j,k} = \frac{\Delta x_2 \varphi_{j+1,k} - \left(\Delta x_1 + \Delta x_2\right)\varphi_{j,k} + \Delta x_1 \varphi_{j-1,k}}{\frac{\Delta x_1 \, \Delta x_2}{2}\left(\Delta x_1 + \Delta x_2\right)}$$

$$- \left(\frac{\Delta x_1 - \Delta x_2}{3}\right) \left.\frac{\partial^2 \varphi}{\partial x^3}\right|_{j,k} + 0(\Delta^2) \tag{23}$$

$$\left.\frac{\partial^2 \varphi}{\partial x \, \partial y}\right|_{j,k} = \frac{\varphi_{j+1,k+1} - \varphi_{j+1,k-1} + \varphi_{j-1,k-1} - \varphi_{j-1,k+1}}{\left(\Delta x_1 + \Delta x_2\right)\left(\Delta y_1 + \Delta y_2\right)}$$

$$- \left(\frac{\Delta x_1 - \Delta x_2}{2}\right) \left.\frac{\partial^3 \varphi}{\partial x^2 \, \partial y}\right|_{j,k} - \left(\frac{\Delta y_1 - \Delta y_2}{2}\right) \left.\frac{\partial^3 \varphi}{\partial x \, \partial y^2}\right|_{j,k} + 0(\Delta^2) \tag{24}$$

where

$$\left.\begin{aligned} \Delta x_1 &= x_{j+1} - x_j \\ \Delta x_2 &= x_j - x_{j-1} \\ \Delta y_1 &= y_{k+1} - y_k \\ \Delta y_2 &= y_k - y_{k-1} \end{aligned}\right\} \tag{25}$$

Skewed Coordinate System

Burstein (ref. 30) computed the inviscid supersonic flow in a channel which contained a compression ramp and utilized a Cartesian coordinate system throughout the flow field. The procedure resulted in extensive interpolation on the ramp since there the grid

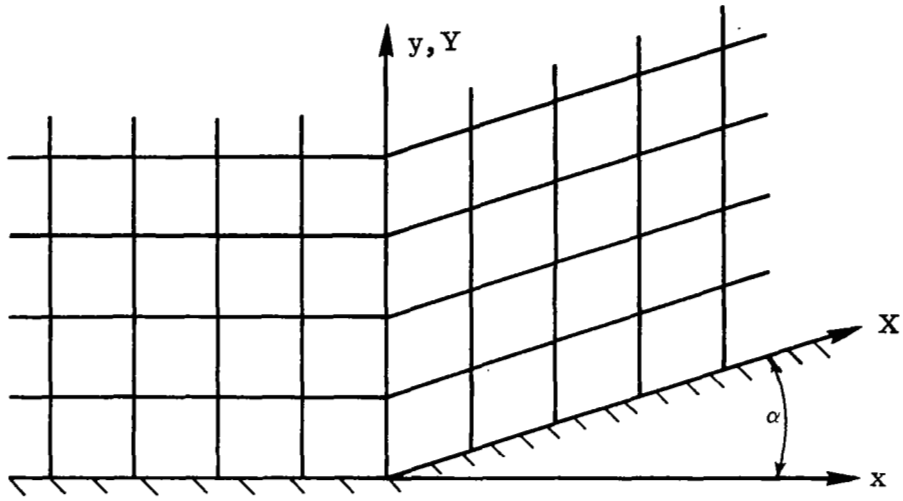

Figure 2.- Skewed coordinate system.

points do not coincide with the ramp surface. This problem can be avoided by using a skewed coordinate system on the ramp as shown in figure 2. The skewed and Cartesian coordinate systems are related by

$$\left.\begin{aligned} X &= x \sec \alpha \\ Y &= y - x \tan \alpha \end{aligned}\right\} \tag{26}$$

The equations relating the derivatives with respect to the Cartesian coordinates (x,y) and those of the skewed coordinates (X,Y) are

$$\left.\begin{aligned} \frac{\partial}{\partial x} &= \sec \alpha \frac{\partial}{\partial X} - \tan \alpha \frac{\partial}{\partial Y} \\ \frac{\partial}{\partial y} &= \frac{\partial}{\partial Y} \\ \frac{\partial^2}{\partial x^2} &= \sec^2 \alpha \frac{\partial^2}{\partial X^2} - 2 \sec \alpha \tan \alpha \frac{\partial^2}{\partial X \, \partial Y} + \tan^2 \alpha \frac{\partial^2}{\partial Y^2} \\ \frac{\partial^2}{\partial y^2} &= \frac{\partial^2}{\partial Y^2} \\ \frac{\partial^2}{\partial x \, \partial y} &= \sec \alpha \frac{\partial^2}{\partial X \, \partial Y} - \tan \alpha \frac{\partial^2}{\partial Y^2} \end{aligned}\right\} \tag{27}$$

As shown in figure 2, the Cartesian and skewed coordinates are used along the flat plate and ramp, respectively; however, special consideration has to be given to the interface between the two systems located at $x = X = 0$. In particular, the derivatives with respect to x (or X) require special treatment in order to maintain second-order accuracy when the difference equations are formulated along the interface. These difference expressions are obtained in the usual manner from Taylor series expansions and are presented in appendix B.

Flat-Plate Boundary Conditions

Figure 3 shows a schematic diagram of the flat-plate flow field at the leading edge. The flow field to be computed is enclosed in a box as shown in figure 3. The free-stream conditions are specified along the upstream boundary and also the outer boundary, provided it is located outside of the leading-edge shock wave. Along the downstream boundary, the flow variables are unknown and must be evaluated from the oncoming flow. In the present calculations, quadratic extrapolation of the flow variables in the x-direction was used continuously to update the downstream boundary conditions. The wall boundary conditions are specified as shown in figure 3. It is observed that the wall pressure is unknown and must be evaluated from the neighboring flow field. Since the wall forms a

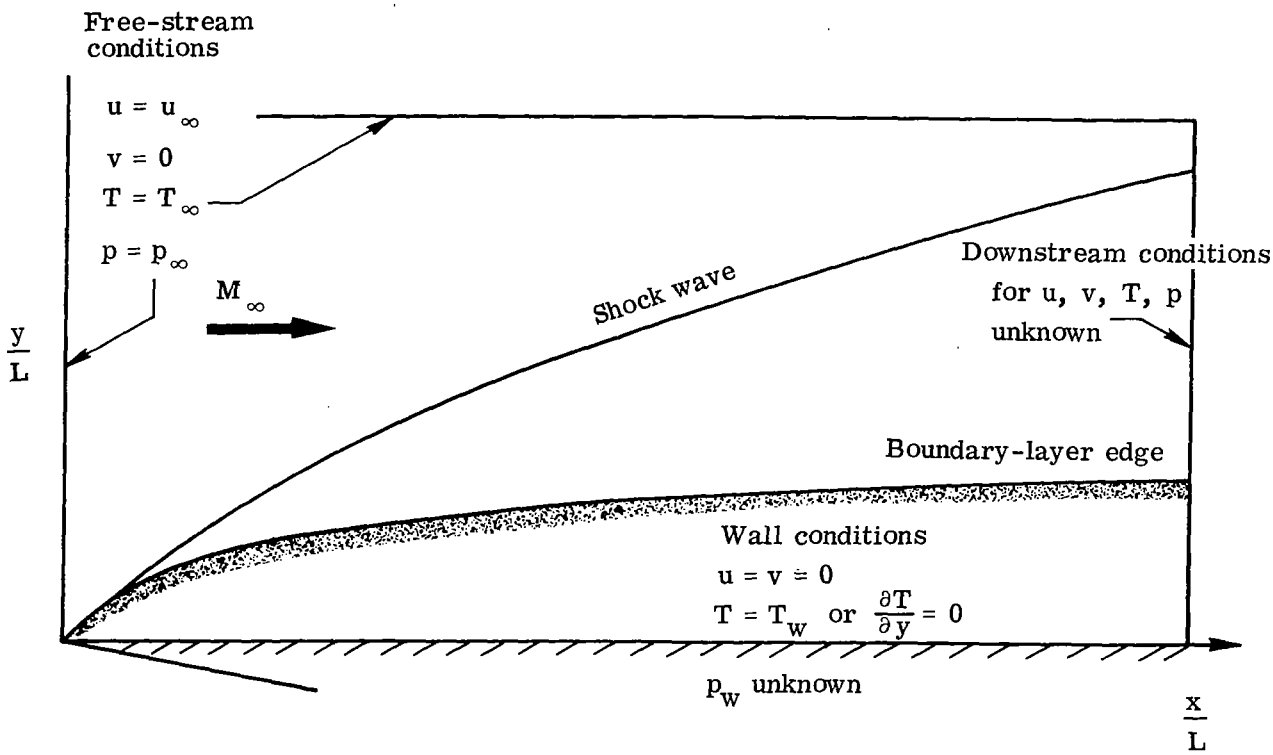

Figure 3.- Schematic diagram of the flat plate flow field and computational boundaries.

boundary of the grid system, the central difference formulation of the equations cannot be used there to find the pressure as is done away from the wall. Different methods of computing the wall pressure and numerical tests of the downstream boundary conditions are discussed in the section "Results and Discussion."

An obvious simplification in these boundary conditions is neglect of the velocity slip and temperature jump that occur at the wall near the leading edge. These effects are important in the merged-layer region (shock wave not distinct from boundary layer) which extends from the leading edge downstream to $\overline{V}_\infty \approx 0.15$ where

$$\overline{V}_\infty = M_\infty \sqrt{\frac{C_\infty}{R_{\infty,x}}} \tag{28}$$

according to measurements made by McCroskey, Bogdonoff, and McDougall (ref. 31). Downstream of the merged layer for supersonic Mach numbers is the weak-interaction region in which the effects of slip and temperature jump are negligible. Because of the higher Reynolds number range, it is the weak-interaction region that is of interest in this investigation; hence, for simplicity, the details of the rarefaction in the relatively small merged-layer region are assumed to have only a local effect. This assumption was verified a posteriori by comparing the numerical solution with results obtained from weak-interaction theory and similar solutions to the boundary-layer equations.

Compression-Corner Boundary Conditions

Figure 4 shows a schematic diagram of the computational box used in the compression-corner calculations with the boundary conditions indicated on the respective faces of the box. These boundary conditions are the same as those used in the flat-plate calculations except for those on the outer boundary. In order to reduce the computer requirements of the calculations, the outer boundary was placed between the wall and the leading-edge shock wave. Placing the outer boundary in the disturbed part of the flow field requires that extrapolation be used continuously to update the flow variables since the conditions are unknown along this boundary. For the present calculations, the extrapolation on the outer boundary was based on the approximate simple-wave character of the outer inviscid flow field. The procedure used in this extrapolation can be described in the following manner. At the completion of each step of the two-step Brailovskaya difference scheme, the inclinations of the steady left-running characteristics were computed along the first row of grid points inside the outer boundary. If the flow is assumed to be of the simple-wave type, these characteristics were linearly extended to the top row of grid points. The flow properties are invariant along straight characteristics; therefore, the unknowns at the top grid points were found from linear interpolation of those values assumed to be constant on the characteristics at the next to top row.

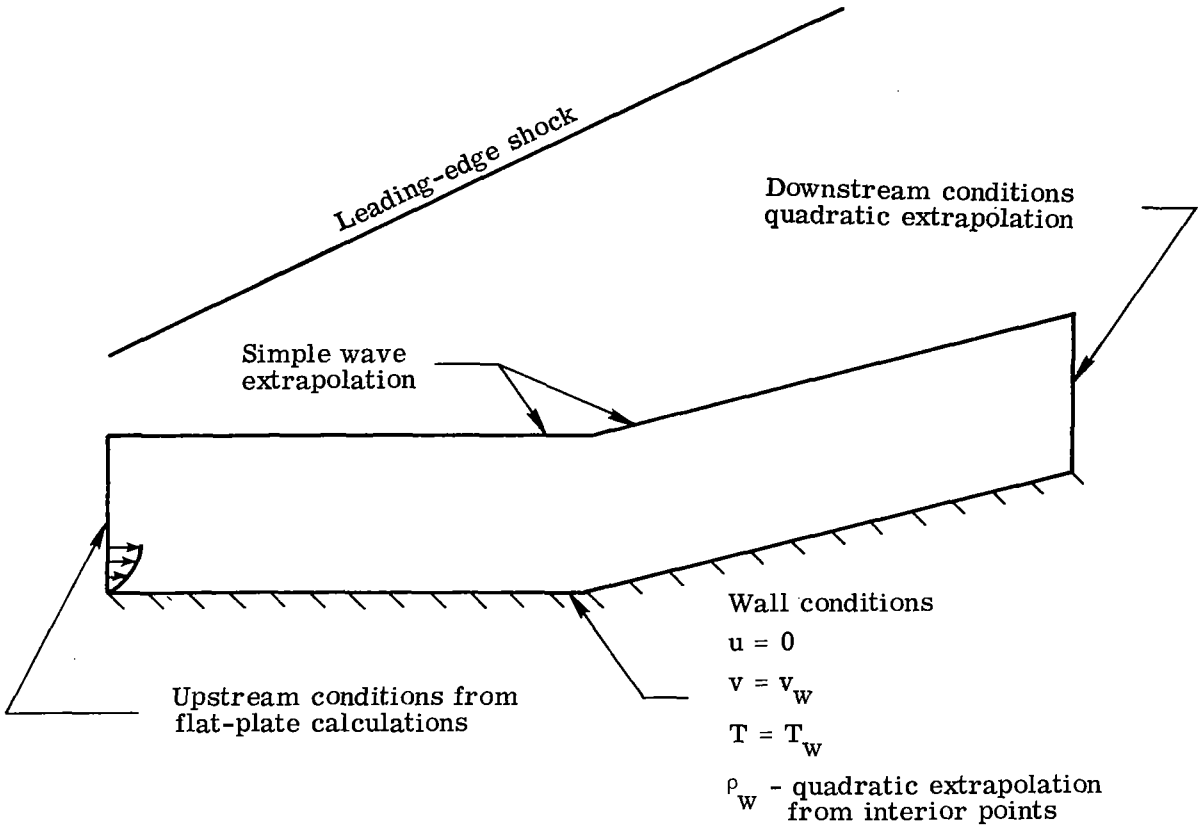

Figure 4.- Schematic diagram showing the computational box and boundary conditions for the compression-corner calculations.

The flow field along the outer boundary is of the simple-wave type provided that

(a) The strength of the reflected waves from both the leading-edge shock and the vorticity layers generated by the leading-edge shock is negligible, and

(b) The coalescence of the compression waves from the corner flow occurs beyond the outer boundary.

It is reasonable to assume that the first condition is satisfied based on the success of the shock-expansion technique, which ignores these effects. Waldman and Probstein (ref. 32) showed that the strength of a reflected wave at a shock is less than 1 percent of the incident wave for $\gamma = 1.4$, free-stream Mach numbers less than 4, and flow deflection angles less than 10°. Even for an infinite Mach number, the strength increases to only 14 percent for deflection angles less than 44°. The vorticity generated by the leading-edge shock is negligible since its curvature is very small for the present conditions. Satisfaction of the second condition had to be verified a posteriori, although one would expect the shock formation point to occur at distances greater than two or three boundary-layer thicknesses, which was the typical position of the outer boundary. Clearly, this assumption is limited by Mach number since as the free-stream Mach number increases, the

separation and reattachment shocks lie closer to the surface, as has been discussed by Holden (ref. 33).

RESULTS AND DISCUSSION

$M_\infty = 3.0$ Flat-Plate Calculations

Calculations were made for the supersonic, viscous flow over a flat plate with the following free-stream conditions:

$$M_\infty = 3.0 \qquad R_{\infty,L} = 10^3 \qquad N_{Pr} = 0.72 \qquad \gamma = 1.4$$

The Sutherland viscosity law was used with the dimensional free-stream temperature chosen at 390° R. The initial conditions were chosen to be that of a flat plate impulsively accelerated to free-stream conditions. Free-stream boundary conditions were enforced along $x = 0$ (with the exception of the grid point located at $y = 0$ where the wall conditions were imposed) and along the outer boundary as shown in figure 3. The boundary conditions along the wall $y = 0$ are given by

$$\left.\begin{aligned} u(x,0) &= v(x,0) = 0 \\ T(x,0) &= T_{o,\infty} = \frac{1}{(\gamma - 1)M_\infty^2}\left(1 + \frac{\gamma - 1}{2} M_\infty^2\right) \end{aligned}\right\} \tag{29}$$

an isothermal wall being assumed. The density at the wall was found by quadratic extrapolation in the y-direction according to the relation

$$\rho(x,y) = \rho_w(x) + \rho_1(x)\, y + \rho_2(x)\, y^2$$

with the quantities ρ_w, ρ_1, and ρ_2 evaluated with the latest known values of the density at the points $y = \Delta y$, $2\,\Delta y$, and $3\,\Delta y$ at each x-station. Other methods of finding the wall density or pressure (only one of these two quantities is needed for the isothermal condition since the other is determined from the state equation) are discussed later in this section. The values of the dependent variables along the downstream boundary, which was placed at $x/L = 1.5$, were continuously updated by quadratic extrapolation in the x-direction. Numerical tests on the effect of this approximation are also discussed later in this section.

Computed results for different grid sizes.- The calculations outlined were made for three different grid sizes in order to obtain a measure of the required resolution. For the isothermal condition it was found necessary to have equal grid spacing in the x- and y-directions in the immediate vicinity of the leading edge so that numerical instability would not result in a divergent solution. It should be noted that there are inconsistencies in the literature with respect to this point. For similar calculations, Kurzrock (ref. 34) observed the same result as found here, whereas MacCormack (ref. 21), in

computing the supersonic flow over an adiabatic sharp-edged plate, used a grid spacing ratio $\Delta x = 40\,\Delta y$ and did not encounter numerical instability. Thommen's calculations (ref. 25) were also for an adiabatic flat plate, but unlike MacCormack, he observed that for $\Delta x = 2\,\Delta y$, an instability resulted that was eliminated for $\Delta x = \Delta y$.

In the present calculations the grid spacing was set equal to 0.05, 0.025, and 0.015. In the first two cases the grid was maintained constant throughout the computational box, but in the third case only $\Delta y/L$ was held constant at 0.015, whereas $\Delta x/L$ was varied as follows in order to reduce the number of x grid points from 100 to 66:

$$\left.\begin{aligned} \frac{\Delta x}{L} &= 0.015 \qquad \left(0 \leqq \frac{x}{L} \leqq 0.15\right) \\ \frac{\Delta x}{L} &= 0.020 \qquad \left(0.15 \leqq \frac{x}{L} \leqq 0.25\right) \\ \frac{\Delta x}{L} &= 0.025 \qquad \left(0.25 \leqq \frac{x}{L} \leqq 1.5\right) \end{aligned}\right\} \tag{30}$$

The converged results for the three grid sizes are presented in figures 5, 6, and 7. The effects of the coarseness of the grid and incorrect wall boundary conditions in the leading-edge region are clearly shown in figure 5 by the large oscillations in the wall pressure near the leading edge. These oscillations disappear closest to the leading edge for the 0.015-grid solution; further downstream, the oscillations disappear in the 0.025-grid solution as these results approach the 0.015-grid results. The results obtained with 0.05 grid differ significantly from the finer grid results. For the leading-edge calculations the parameter which determines the effective resolution of the calculations is the grid-spacing Reynolds number $R_\Delta = \frac{\rho_\infty u_\infty \Delta}{\mu_\infty}$. These calculations were made for $R_\Delta = 15$, 25, and 50 for the three respective grid sizes. Numerical instability resulted when the same flow field was calculated with $R_\Delta = 250$. Therefore, for the leading-edge calculation, there appears to be an upper bound on the grid-spacing Reynolds number in order to achieve stable results.

Figure 7 shows profiles of u/u_∞, v/u_∞, T/T_∞, and ρ/ρ_∞ at $x/L = 1.0$ $\left(R_{\infty,x} = 10^3\right)$. The extrapolation at the downstream boundary $x/L = 1.5$ introduces slight errors, and therefore it was desired to make the comparisons upstream of the influence of this effect. In figure 7 the distinctive features of the flow are evident. The boundary-layer edge is at $y/L \approx 0.25$ with the leading-edge shock located at $y/L \approx 0.57$; thus, $x/L = 1.0$ is downstream of the merged region. This result is expected since $\overline{V}_\infty = 0.083$ at this position and, as indicated previously, the downstream extent of the merged region is $\overline{V}_\infty \approx 0.15$. In figure 7(c) the slightly negative wall temperature gradient indicates that heat is being transferred from the wall to the stream. This result is expected since the adiabatic wall temperature for $N_{Pr} = 0.72$ is less than the free-stream total temperature which was the isothermal wall condition chosen here.

Convergence of the calculated results with decreasing grid size is evident in the profiles at $x/L = 1.0$ shown in figure 7. Observing the boundary-layer part of these profiles, it appears that it is necessary to use approximately 15 grid points in the boundary layer for adequate resolution. This result should be general and is used as a guideline throughout the present investigation. Cheng (ref. 14) determined qualitatively from truncation-error considerations of Burger's equation that for second-order accurate schemes, a minimum of 20 or 30 grid points are required per characteristic viscous dimension for adequate resolution. Thommen and Magnus (ref. 35) concluded from their numerical study of Burger's equation that only 5 grid points would be required per boundary-layer thickness.

The effect of the grid refinement is more significant near the shock wave as shown in figures 7(b) and 7(d) for the profiles of normal velocity and density. The 0.015-grid spacing eliminates most of the oscillation in the shock transition region, whereas the 0.025-grid size results in significant oscillation. Naturally, this shock smearing places some upper bound on the grid spacing; however, as the calculations are extended downstream, this grid criterion can be relaxed somewhat since the leading-edge shock weakens, and the shock layer thickens and allows more distance for the oscillations to damp out before entering the boundary layer.

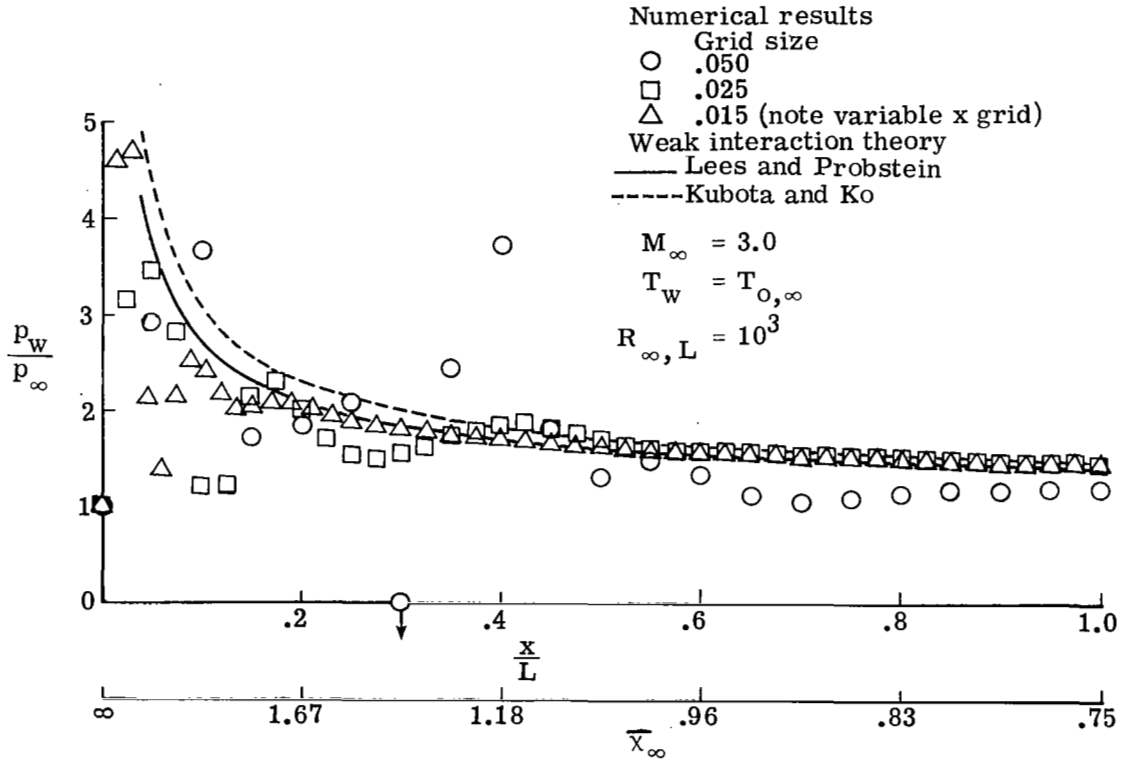

Figure 5.- Comparison of wall pressure distribution for different grid sizes with weak interaction theory.

Comparison with weak-interaction theory.- Shown for comparison in figure 5 is the wall pressure predicted by the second-order weak-interaction analyses of Lees and Probstein (ref. 36) and Kubota and Ko (ref. 37). The analysis of Lees and Probstein is based on a Taylor series expansion of the induced pressure in powers of $d\delta^*/dx$ with the coefficients in this expansion determined from the tangent-wedge approximation. The weak-interaction analysis of Kubota and Ko is somewhat similar in that it is based on a series expansion in powers of $\bar{\chi}_\infty$ where

$$\bar{\chi}_\infty = M_\infty^3 \sqrt{\frac{C}{R_{\infty,x}}} \tag{31}$$

with the coefficients in the series determined by substitution into the integral boundary-layer equations of Lees and Reeves (ref. 4). In addition, the equations given by Kubota and Ko (ref. 37) were for $N_{Pr} = 1.0$ and an adiabatic wall. With $N_{Pr} = 1.0$ the approximate recovery factor is 1.0 and results in an adiabatic wall temperature equal to the free-stream total temperature, the assumed wall temperature in the present calculations. As seen in figure 5, both theories give good results in comparison with the present numerical results. The Lees and Probstein (ref. 36) theory slightly underpredicts the

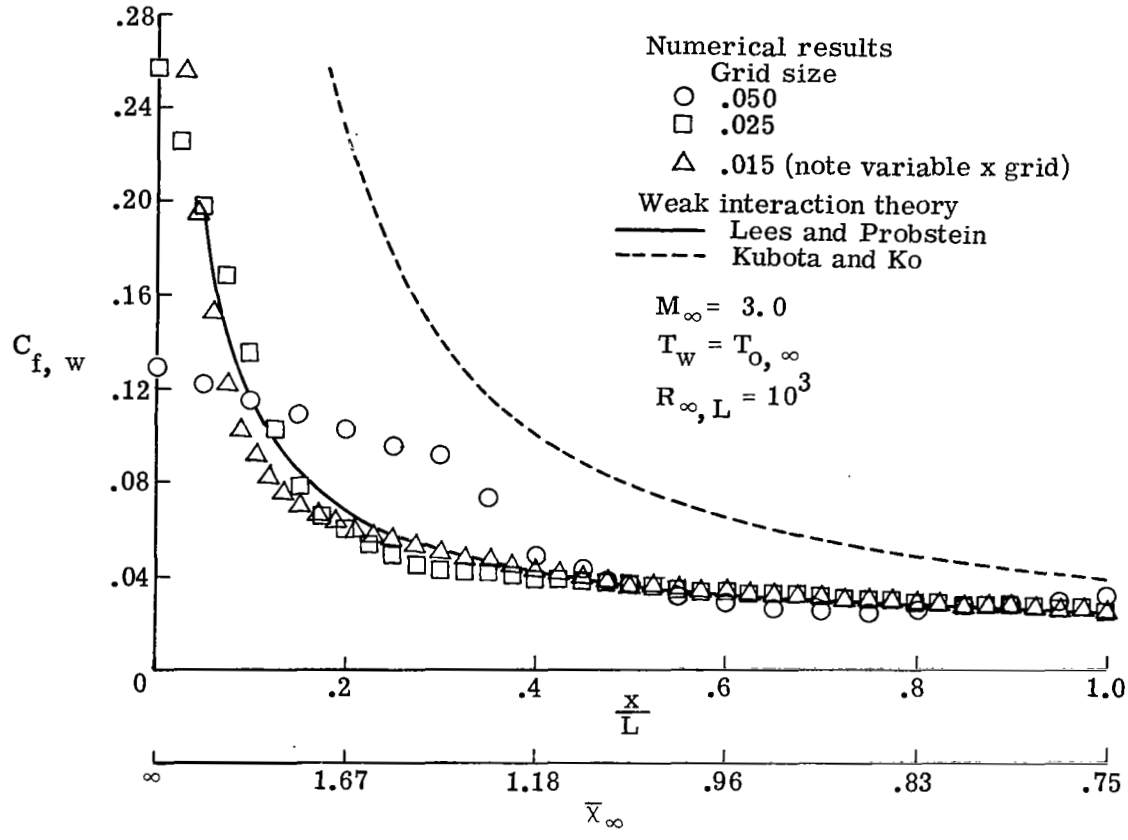

Figure 6.- Comparison of wall skin-friction distribution for different grid sizes with weak interaction theory.

induced pressure which is consistent with the comparisons made by Kubota and Ko (ref. 37). However, a much greater disagreement is shown in figure 6 where the wall skin-friction coefficient written as

$$C_{f,w} = \frac{\tau_w}{\frac{1}{2}\rho_\infty u_\infty^2} \tag{32}$$

is plotted against x/L and the interaction parameter $\bar{\chi}_\infty$. Excellent agreement is obtained between the Lees and Probstein analysis and the numerical results, but the agreement is much poorer between these results and the Kubota and Ko analysis. The difference is unexplained, although downstream the agreement improves considerably, as shown by Carter (ref. 18).

Comparison with similar solutions.- Shown for comparison in figure 7 are the zero-pressure-gradient similar solutions of the boundary-layer equations for the specific flow conditions prescribed here. In order to convert the similar-solution results given in tabular form by Low (ref. 38) from the nondimensional Blasius variables to the present nondimensional variables, it is necessary to specify u, ρ, and T at the boundary-layer edge as well as $u = v = 0$ and $T = T_w$ at the wall. Rather than choose free-stream conditions for the outer-edge conditions as would be consistent with first-order boundary-layer theory, the edge conditions were chosen from the present results obtained from the Navier-Stokes equations. This choice was made by assuming that the wall pressure ratio $p_w/p_\infty = 1.425$ was constant throughout the boundary layer. This pressure and the edge temperature $T_e/T_\infty = 1.171$, taken from figure 7(c), gives the edge density $\rho_e/\rho_\infty = 1.221$. From figure 7(a) the edge velocity is $u_e/u_\infty = 0.95$. This procedure obviously forces the agreement of the Navier-Stokes and boundary-layer equation solutions at the boundary-layer edge; however, the good agreement elsewhere indicates the correctness of the present results. The effect of the negative pressure gradient is seen in figure 7(a) since the u-component of velocity is greater at a given y-position for the Navier-Stokes results than that for the zero-pressure-gradient similar solution. In addition to the differences due to pressure gradient, it was also found that the Chapman-Rubesin (ref. 39) form of the linear viscosity law used in the similar solutions introduced a slight error. This viscosity law is given by

$$\frac{\mu}{\mu_r} = C\frac{T}{T_r} \tag{33}$$

where

$$C = \frac{T_r + S_o}{T_w + S_o}\sqrt{\frac{T_w}{T_r}} \tag{34}$$

At the wall the linear result is forced to agree with that given by the Sutherland relation. Inserting the Chapman-Rubesin viscosity law into the Navier-Stokes calculations reduced

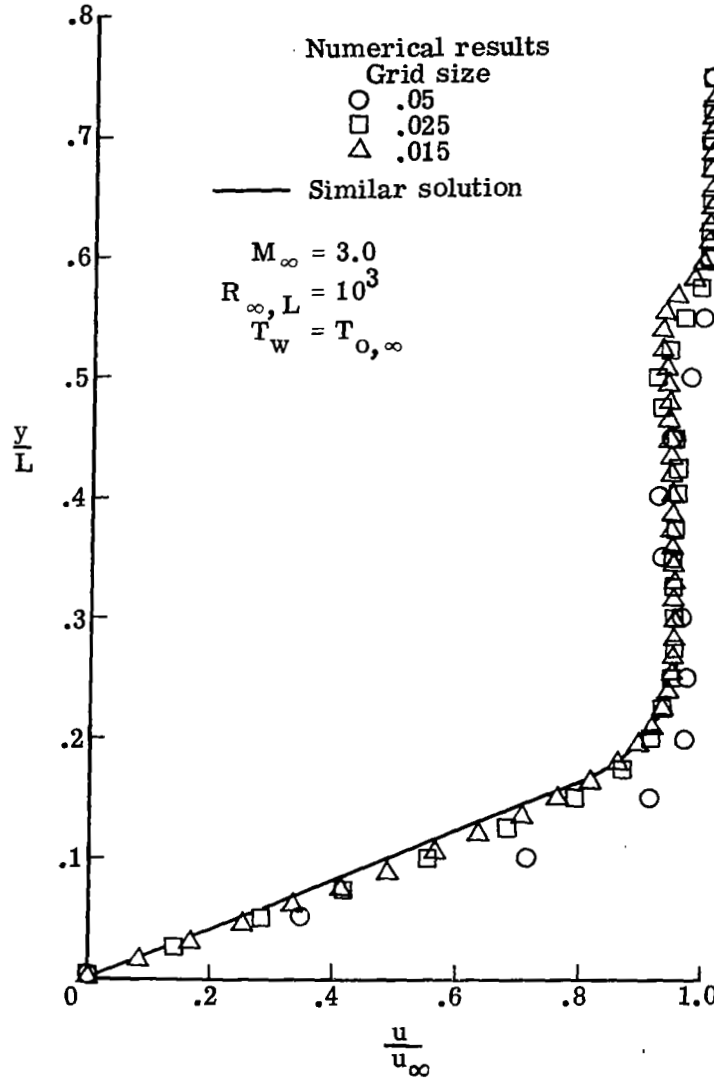

(a) u component of velocity.

Figure 7.- Profiles of flow properties at $\frac{x}{L} = 1.0$ $\left(R_{\infty,x} = 10^3\right)$ for different grid sizes with comparison to similar solutions.

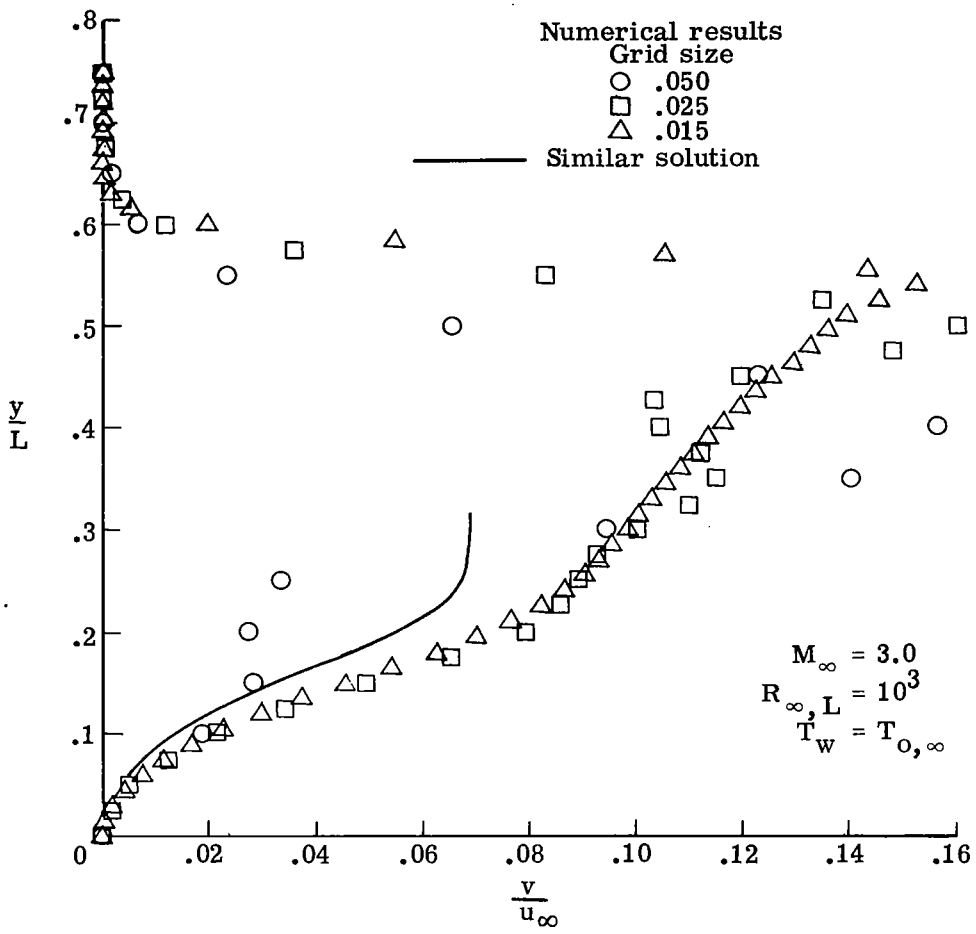

(b) v component of velocity.

Figure 7.- Continued.

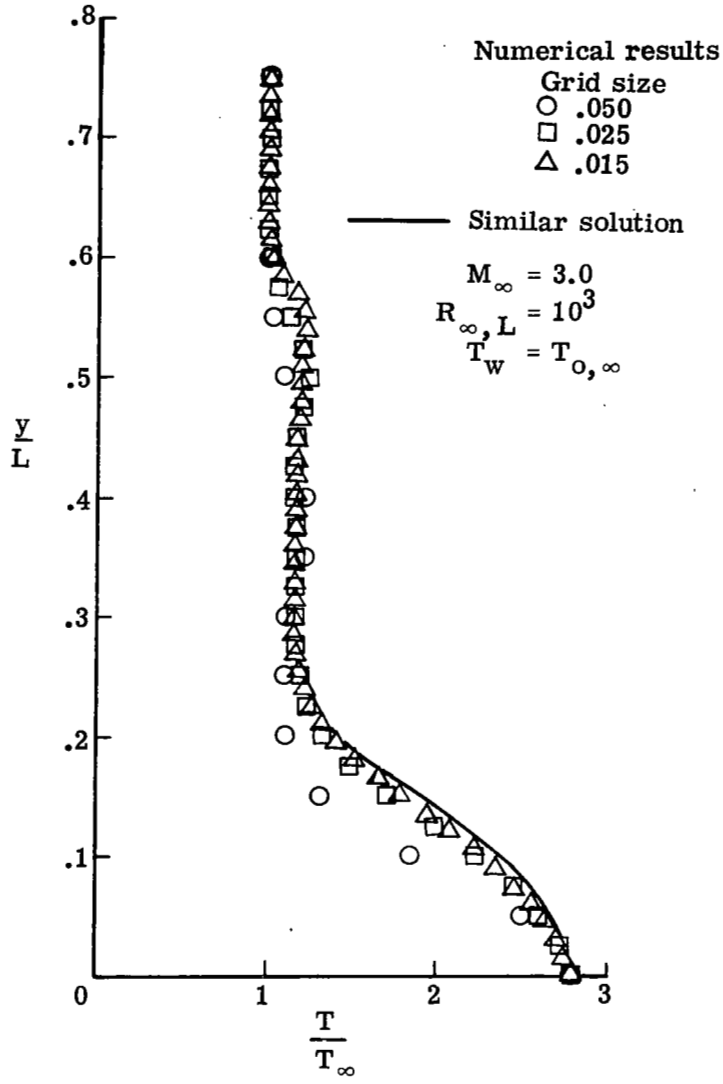

(c) Temperature.

Figure 7.- Continued

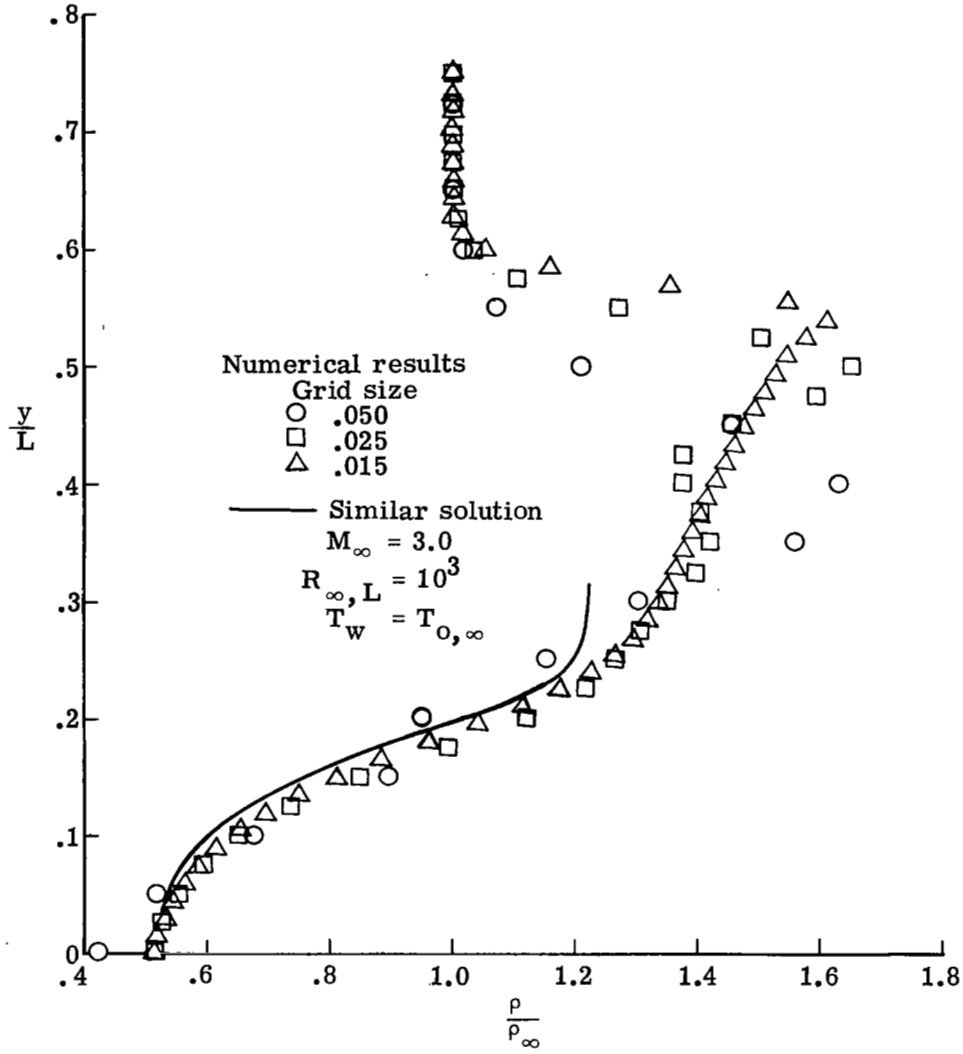

(d) Density.

Figure 7.- Concluded.

the differences between the Navier-Stokes results and the similar solutions by several percent.

Computation rate.- It is convenient at this point to discuss the computer time used to perform the present calculations. The large demands for both computer time and storage which are required for these calculations are the main drawback to the present approach. The computational rate of the present program as applied to the flat-plate flow field was found to be 2.75×10^6 grid points/hour on the Control Data 6600 computer at the Langley Research Center. At this rate the program can execute 10^3 time cycles through a field of 2750 grid points in 1 hour of machine time.

The number of cycles required for convergence of the calculations discussed were approximately 500, 900, and 1300 for the grid sizes of 0.05, 0.025, and 0.015. In all three cases the initial conditions were assumed to be those of a flat plate impulsively accelerated to free-stream conditions. The required computer times for these calculations for the respective grid sizes were 0.175, 0.82, and 2.12 hours on the Control Data 6600 computer. For the flat-plate calculations, the two velocity components at the downstream end of the calculation were the slowest of the dependent variables to converge. Convergence was assumed when their values ceased to change in the fifth significant digit. As is typical of results obtained by the time-dependent technique, the solution varies rapidly at the start, and is followed by a slowly varying monotonic approach to convergence.

Different methods of computing wall pressure.- Several techniques for updating the fluid density (or pressure) at the wall were tested on the leading-edge flat-plate flow field discussed previously. This calculation provides a severe test of the various numerical methods because of the large gradients near the leading edge.

The techniques that were used fall into two categories: extrapolation from interior points, and evaluation of the equations at the wall with one-sided difference quotients. As was indicated previously, quadratic extrapolation of the density from the three grid points above the wall and the subsequent evaluation of the pressure from the state equation gave the best results. Linear extrapolation of the density resulted in an unstable calculation. This result is not surprising since linear extrapolation introduces an error of $0(\Delta^2)$ in the dependent variable, whereas the difference scheme computes the dependent variable with a higher order error of $0(\Delta^3)$, as can be seen in equation (16). Quadratic extrapolation admits a third-order error and hence is consistent with the difference scheme. In addition to the density extrapolation, quadratic extrapolation was also attempted with p and with $p + \rho v^2$ to find the wall pressure. Both of these attempts produced unstable calculations.

In principle, it would seem to be preferable to use either the continuity or y-momentum equation to determine either the density or pressure at the wall. Evaluated at the wall, the continuity equation becomes

$$\frac{\partial \rho}{\partial t} = -\frac{\partial \rho v}{\partial y} \tag{35}$$

Similarly, the y-momentum equation is given by

$$\frac{\partial p + \rho v^2}{\partial y} = \frac{1}{R_{\infty,L}}\left[\mu\left(\frac{4}{3}\frac{\partial^2 v}{\partial y 2} + \frac{1}{3}\frac{\partial^2 u}{\partial x\, \partial y}\right) + \frac{4}{3}\frac{\partial \mu}{\partial y}\frac{\partial v}{\partial y}\right] \tag{36}$$

Equation (35) or (36) is evaluated to find ρ or p at the wall, respectively, by using suitable second-order one-sided difference quotients for the spatial derivatives and a first-order forward time-difference quotient for $\partial\rho/\partial t$. The calculations were unstable when the y-momentum equation was used to evaluate p_w; for the same calculations, use of the continuity equation to find ρ_w resulted in a converged solution although large oscillations occurred near the wall. Figure 8 shows a comparison of the pressure distributions at $x/L = 1.0$ obtained by using extrapolation and the continuity equation to find ρ_w. In both calculations the grid spacing was $\frac{\Delta x}{L} = \frac{\Delta y}{L} = 0.025$. Using the continuity equation to find ρ_w results in a pressure distribution with large oscillations whose amplitude decreases away from the wall. Clearly, the extrapolation technique is preferable.

Numerical tests on downstream boundary conditions.- The use of extrapolation in x continuously to update the flow variables at the downstream boundary presumably approximates the effect of a flat plate which extends far downstream. Naturally, the questions arise: What is the degree of inaccuracy introduced by this approximation and what is the extent of its upstream influence through the subsonic part of the boundary layer? It is desired to extend the present calculations downstream to higher Reynolds numbers by using the present downstream conditions as upstream conditions for the next calculation. If the extrapolation introduces sizable upstream errors, then such a procedure would not be efficient because of the large degree of overlapping required for the computational boxes. Callens (ref. 40) discussed the use of such a procedure and suggested that overlapping would reduce the effect of the errors due to extrapolation; however, he did not indicate the magnitude or upstream extent of these errors.

A numerical test was performed on the calculations discussed previously in this section to answer these questions. Calculations were made by use of the 0.025 grid for three computational boxes, one of which enclosed the other two. The results of these calculations are shown in figure 9, where the x-extent of each calculation is given. Both the wall pressure and the pressure along $y/L = 0.225$, which is above the sonic line and near the boundary-layer edge, are plotted against x/L in order to compare the effect of the error on both a subsonic and supersonic region. The "bump" in the pressure distribution along $y/L = 0.225$ is part of the oscillations that result from the smearing of the shock wave by the finite-difference scheme. The results shown in figure 9 indicate

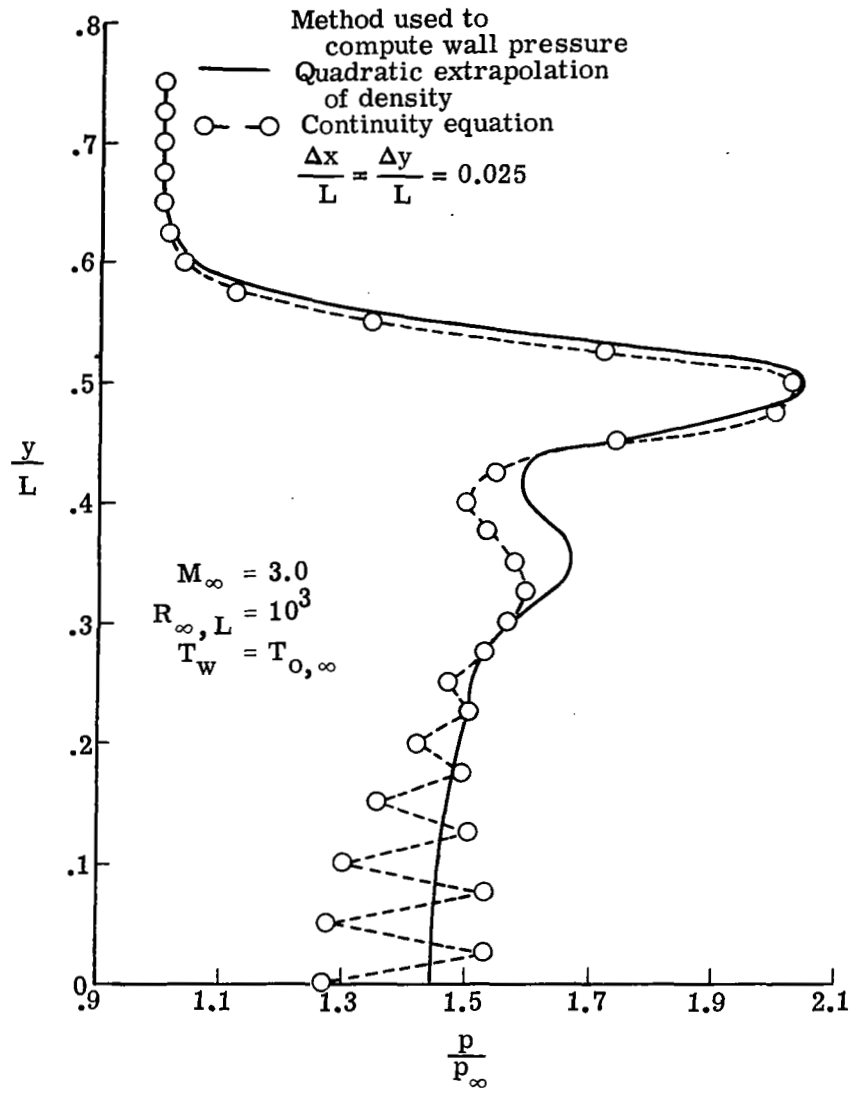

Figure 8.- Comparison of pressure profiles at $\frac{x}{L} = 1.0$ $\left(R_{\infty,x} = 10^3\right)$ using the continuity equation and quadratic extrapolation of the density to continuously update the wall pressure.

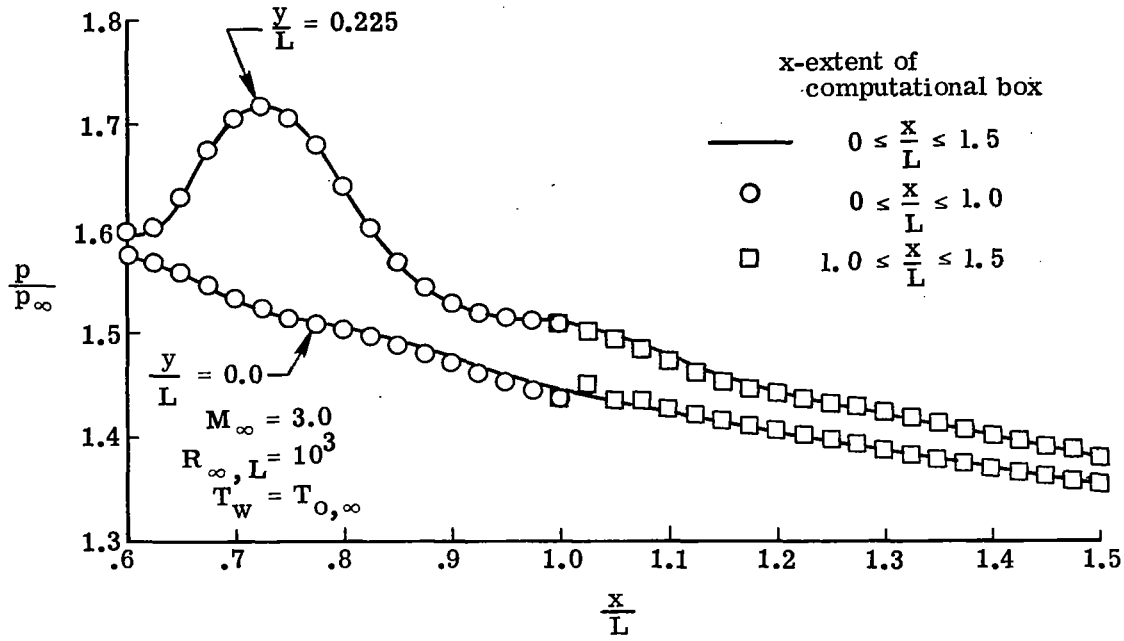

Figure 9.- Effects of downstream extrapolation on streamwise pressure distribution near the downstream boundary.

that an error of about 1 percent in the wall pressure occurs at $x/L = 1.0$ where the quadratic extrapolation was made. This error is propagated upstream through the subsonic part of the boundary layer and disappears within approximately 10 grid points. The effect of the extrapolation on the pressure along $y/L = 0.225$ is considerably smaller although a slight error is detectable. This error is attributed to the fact that the point $x/L = 1.0$, $y/L = 0.225$ is slightly within the zone of influence of the boundary layer which is altered by extrapolation errors.

The second aspect of the test calculations is to determine the effect of using extrapolated conditions as upstream boundary conditions for a downstream flat-plate calculation. Figure 9 shows that the wall pressure quickly recovers to the correct solution, whereas the slight error in the upstream pressure along $y/L = 0.225$ persists even farther downstream as is typical of inviscid flow.

The important point to be made here is that the use of extrapolation introduces only small errors of limited upstream extent. It is presumed that as the calculations extend farther downstream, these errors will become less since the gradients in the x-direction become smaller. In addition, it does not appear to be necessary to overlap the computational boxes since the extrapolation errors are quickly damped out.

Extension to higher Reynolds numbers.- The present results were extended downstream to higher Reynolds numbers by using the downstream conditions at $x/L = 1.0$ as upstream boundary conditions as was discussed in the previous section. In this manner

the calculations can be made for any Reynolds number desired. Instead of using a rectangular computational box as was done in the leading-edge calculations, a trapezoidal box was used with the outer boundary of the downstream box inclined at an angle slightly larger than the leading-edge shock-wave angle at the interface. The expansion waves generated by the displacement thickness weaken the shock, and its position therefore moves farther inside the computational box. Use of the trapezoidal box avoids the needless calculations in the free stream that are required for the rectangular box and also allows free-stream conditions to be specified along the outer boundary.

The calculations were made from $x/L = 1.0$ $\left(R_{\infty,x} = 10^3\right)$ to $x/L = 6.0$ $\left(R_{\infty,x} = 6.0 \times 10^3\right)$ by use of the trapezoidal computational box with the outer boundary inclined at an angle of 29° with respect to the free stream. The grid spacing in the y-direction along the inclined boundary was increased at a constant rate of 20 percent from 0.025 to 0.055. Since the grid spacing in the x-direction is determined by the y-spacing along the inclined boundary, the resulting x-grid increased from 0.025 to 0.1. Figure 10 shows a flow-field map deduced from the leading-edge and downstream flat-plate calculations. The characteristic features of the supersonic flat-plate flow field are shown: the boundary-layer-induced shock wave, displacement thickness, streamline

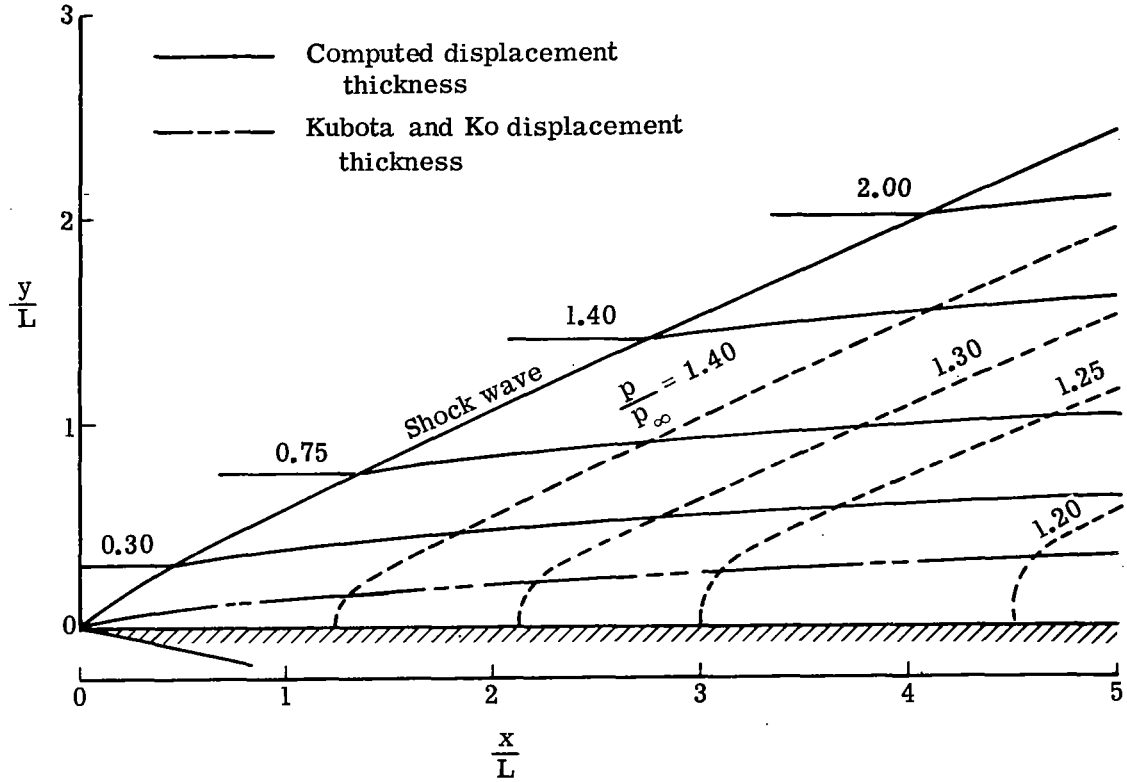

Figure 10.- Computed flow field over a flat plate with $M_\infty = 3.0$ and $T_w = T_{o,\infty}$.

pattern, and contours of constant pressure. The displacement thickness was computed by using the trapezoidal rule to evaluate

$$\delta^* = \int_0^{\delta} \left[1 - \frac{\rho u}{(\rho u)_\delta}\right] dy \tag{37}$$

It was observed that the u-velocity component reaches a local maximum near the boundary-layer edge, as can be seen in figure 7(a). By denoting this value as u_e, δ was taken as the value of y where $u = 0.99u_e$. Also shown in figure 10 is the excellent agreement obtained between the calculated displacement thickness and that given by the Kubota and Ko weak-interaction theory applied to the present flow field. The finite-difference scheme smears the shock over several grid spaces (the actual number depends on the grid size), and therefore the discrete shock wave shown in figure 10 is an estimate deduced from the pressure distributions. It was found that the scatter in the locus of estimated shock points was always no more than one x- or y-grid spacing. The pressure contours correctly indicate both the relatively constant nature of the pressure in the boundary layer and the constant slope that is characteristic of simple-wave flow in the inviscid part of the flow field. The inclination of the pressure contours differ from that of the Mach lines by less than 0.5° in the inviscid part of the flow exclusive of the immediate neighborhood of the shock.

$M_\infty = 6.06$ Flat-Plate Calculations

In the compression-corner calculations, which will be described in the next section, comparison is made with the experimental measurements of Lewis, Kubota, and Lees (ref. 11). The upstream boundary conditions for this calculation were computed by use of five tandem computational boxes which extend from the leading edge to $x/L = 10.0$ $\left(R_{\infty,x} = 10^5\right)$, as shown in figure 11. Greater use was made of variable grid in these calculations than in the $M_\infty = 3.0$ calculations, as shown in the table given in figure 11. Variable grid in both the x- and y-directions was imposed by varying the respective grid spacing at a constant rate, the rate being 10 percent or less. The effect of variable grid is easily seen in figure 11 since the first four boxes have approximately the same number of grid points, but their respective sizes increase considerably with downstream distance. As seen in figure 11, no overlap of the computational boxes was used as was previously found to be acceptable.

For these calculations, $M_\infty = 6.06$ and the free-stream static temperature was 88° R. The wall-temperature boundary condition was assumed to be best approximated by an isothermal condition since longitudinal conduction occurred in the experimental model. (See ref. 41.) If the recovery factor is assumed to be equal to $\sqrt{N_{Pr}}$, it is found from the oblique shock equations that the recovery temperature only changes by 2 percent from the flat plate to the ramp; thereby, the use of an isothermal condition is further

Box	Grid points	$\left(\frac{\Delta x}{L}\right)_{min}$	$\left(\frac{\Delta x}{L}\right)_{max}$	$\left(\frac{\Delta y}{L}\right)_{min}$	$\left(\frac{\Delta y}{L}\right)_{max}$
I	1271	0.0025	0.0025	0.0025	0.0025
II	1182	.00357	.0153	.0025	.0090
III	1182	.0153	.104	.0050	.0353
IV	1182	.100	.143	.0135	.0528
V	1947	.144	.220	.0270	.0724

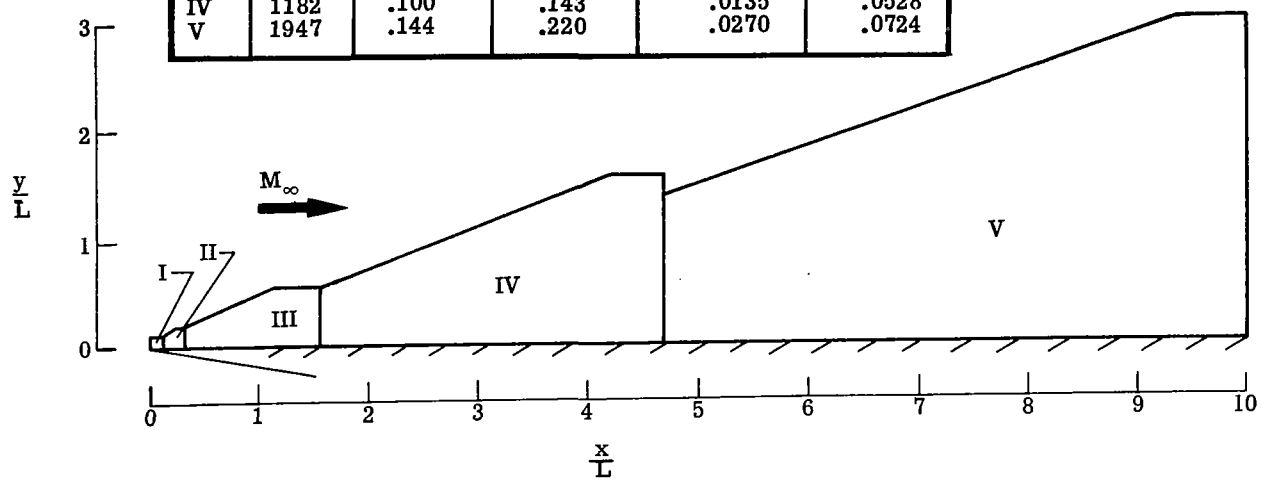

Figure 11.- Schematic diagram of the computational boxes used to compute the $M_\infty = 6.06$ flat-plate flow field.

justified. The constant wall temperature is denoted by $\overline{T}_{aw}$ and is given by

$$T_w = \overline{T}_{aw} = \frac{1}{(\gamma - 1)M_\infty^2}\left(1 + \frac{\gamma - 1}{2}\sqrt{N_{Pr}}\,M_\infty^2\right) \tag{38}$$

The results obtained here are similar in nature to those computed for $M_\infty = 3.0$ and therefore only a short discussion will be given. Figure 12 gives a flow-field map showing the shock wave, streamlines, pressure contours, and displacement thickness. It is seen in figure 12 that the shock position found numerically is in excellent agreement with that found by Lewis et al. (ref. 41) from pitot pressure measurements. Also shown is the displacement thickness predicted by the Kubota and Ko weak-interaction analysis, which is slightly larger than the computed displacement thickness. Correspondingly, the estimate of the induced pressure based on the Kubota and Ko analysis is slightly larger than that found in the present investigation, as shown in figure 13. It is presumed that both of these differences are due to the fact that the Kubota and Ko analysis assumed that $N_{Pr} = 1$. This value yields a higher recovery temperature that results in a thicker boundary layer and greater induced pressure. In figures 13 and 14, it is observed that the induced pressure and the skin friction found by solving the Navier-Stokes equations has slight oscillations near $x/L = 1.6$ and $x/L = 4.75$. These oscillations are non-physical and result from the use of extrapolation at the downstream boundary as was previously discussed. Also shown in figure 13 is the wall pressure measured by Lewis

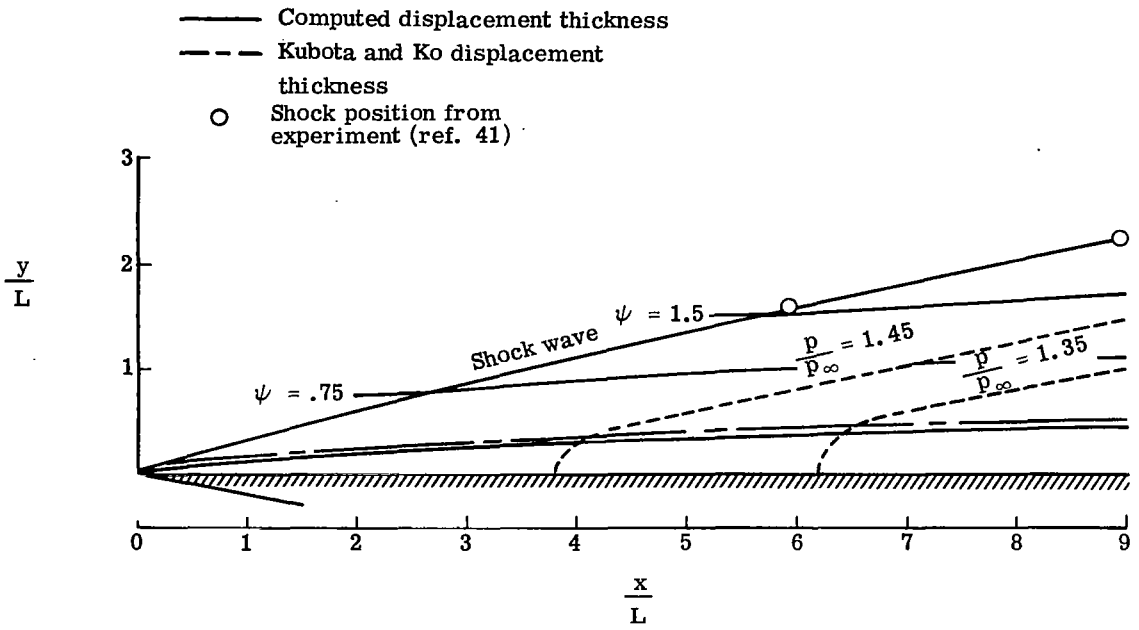

Figure 12.- Computed flow field over a flat plate with $M_\infty = 6.06$ and $T_w = \bar{T}_{aw}$.

et al. at $R_{\infty,x} = 7.5 \times 10^4$ and it is seen to be 7 percent higher than that found numerically or that given by weak-interaction theory.

Figure 14 shows the wall skin-friction coefficient plotted against x/L and the viscous interaction parameter $\bar{\chi}_\infty$. The agreement between the Lees and Probstein weak-interaction analysis and the present results is excellent, whereas the Kubota and Ko analysis overpredicts the increase in skin friction, as was found in the $M_\infty = 3.0$ comparisons. Also shown for comparison is the similar solution skin-friction distribution, which is less than the other results since ignoring the favorable pressure gradient results in a thicker boundary layer and reduced skin friction.

Figure 15 shows a comparison of pitot pressure from the present results with that measured by Lewis et al. at $R_{\infty,x} = 7.5 \times 10^4$, and it is seen that the agreement is only fair. Inadequate numerical resolution is not the cause of the differences shown in figure 15 since the calculated results changed by less than 1 percent when the grid spacing was halved in the direction normal to the plate.

Figure 16 shows a similar comparison of the numerical and experimental Mach number profile at the same x-station. The Mach number has been normalized by the edge value which was determined to be 5.56 in the experiment and 5.66 from the numerical solution. Similarly, the distance normal to the plate has been nondimensionalized by the boundary-layer thickness which is defined in figure 15 and is the same definition as that used by Lewis et al. The numerical and experimental values of the boundary-layer

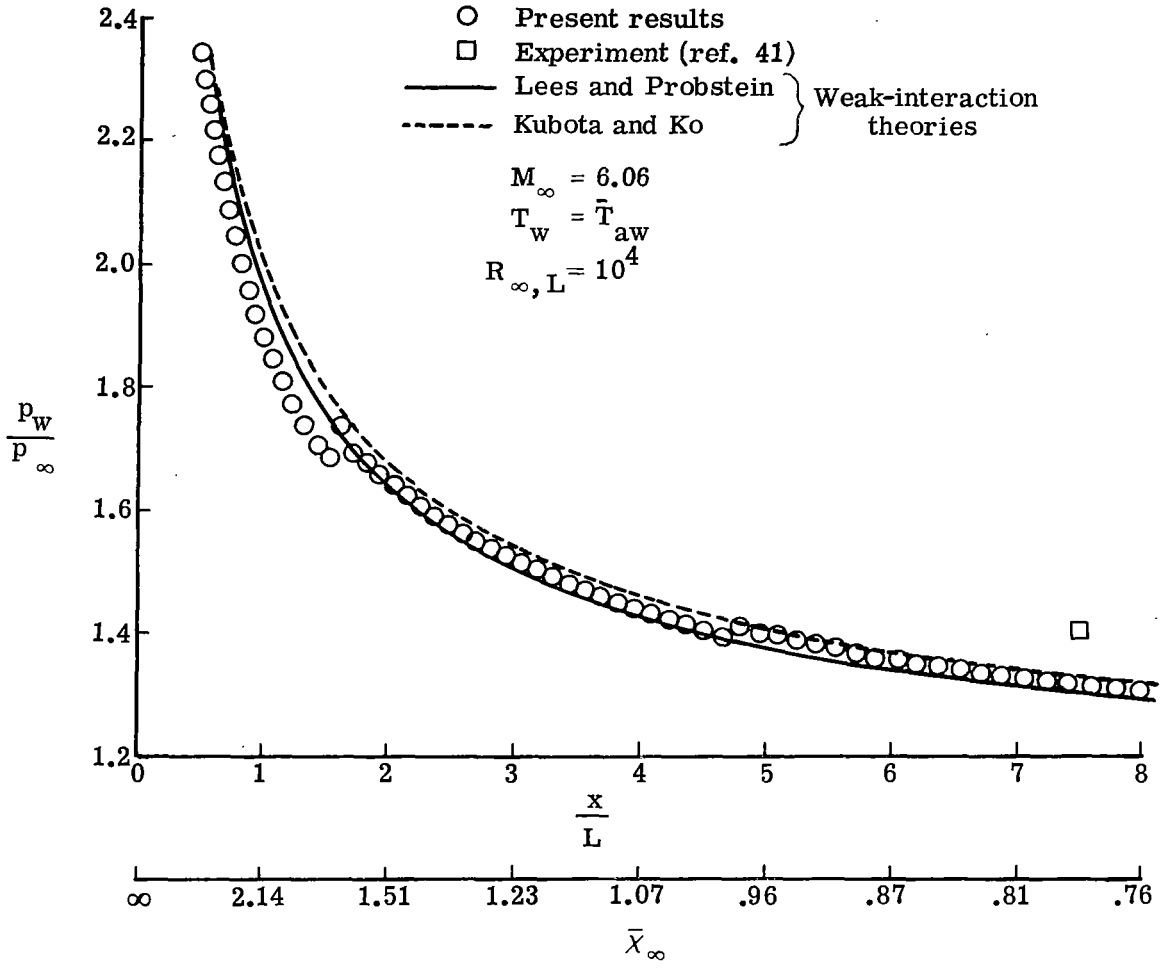

Figure 13.- Comparison of wall pressure distribution with weak,interaction theories.

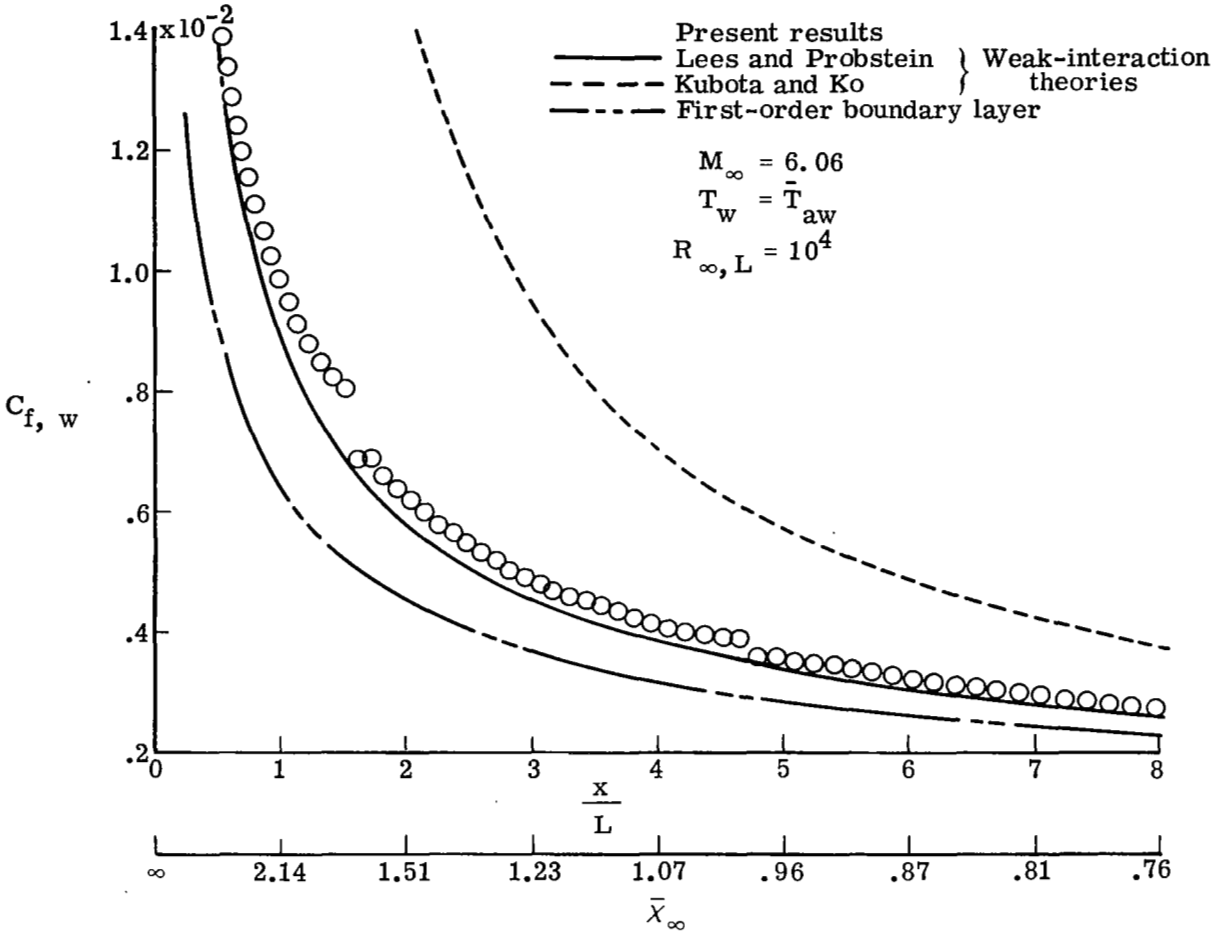

Figure 14.- Comparison of wall skin-friction distribution with weak-interaction theories.

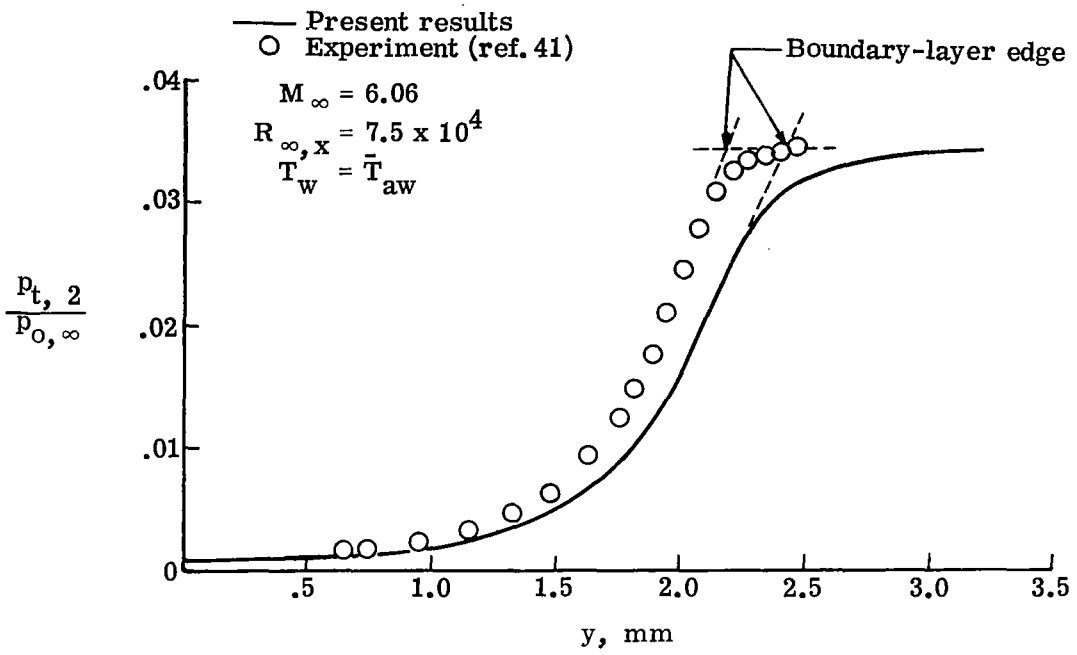

Figure 15.- Comparison of theoretical and experimental pitot pressure profile.

thickness are 2.31 mm (0.095 inch) and 2.18 mm (0.086 inch), respectively. The agreement of the two profiles shown in figure 16 is excellent. Plotting the profile data in this manner enhances the agreement, but it should be noted that the improved agreement in figure 16 is better than that shown in figure 15 because M/M_e is less sensitive than $p_{t,2}/p_{0,\infty}$. For Mach numbers near 5, a 1-percent error in Mach number amplifies to a 2-percent error in $p_{t,2}/p_{0,\infty}$.

$M_\infty = 3.0$ Compression-Corner Calculations

The $M_\infty = 3.0$ flat-plate calculations which were made downstream to $R_{\infty,x} = 6.0 \times 10^3$ were used as upstream boundary conditions for the compression-corner calculations with the corner located so that the Reynolds number based on free-stream conditions and the distance from the leading edge to the corner is $R_{\infty,x_c} = 1.68 \times 10^4$. The outer position of the computational box was located at $y/x_c = 0.0868$ which is approximately one-half of the shock-layer thickness and twice the boundary-layer thickness at the upstream boundary. The computational box extended downstream to $x/x_c = 1.99$. The total number of grid points used was 2156 (77 in the x-direction and 28 in the y-direction); thereby a constant grid spacing in the x- and y-directions of 0.0214 and 0.00321, respectively, resulted. For the compression-corner calculations, the computational rate was 2.25×10^6 grid points/hour on the Control Data 6600 computer. This rate was a decrease of approximately 20 percent from that found for the flat-plate calculations and was due to the extra calculations needed at the coordinate system interface and for the simple-wave extrapolation. The same convergence criterion was applied that was

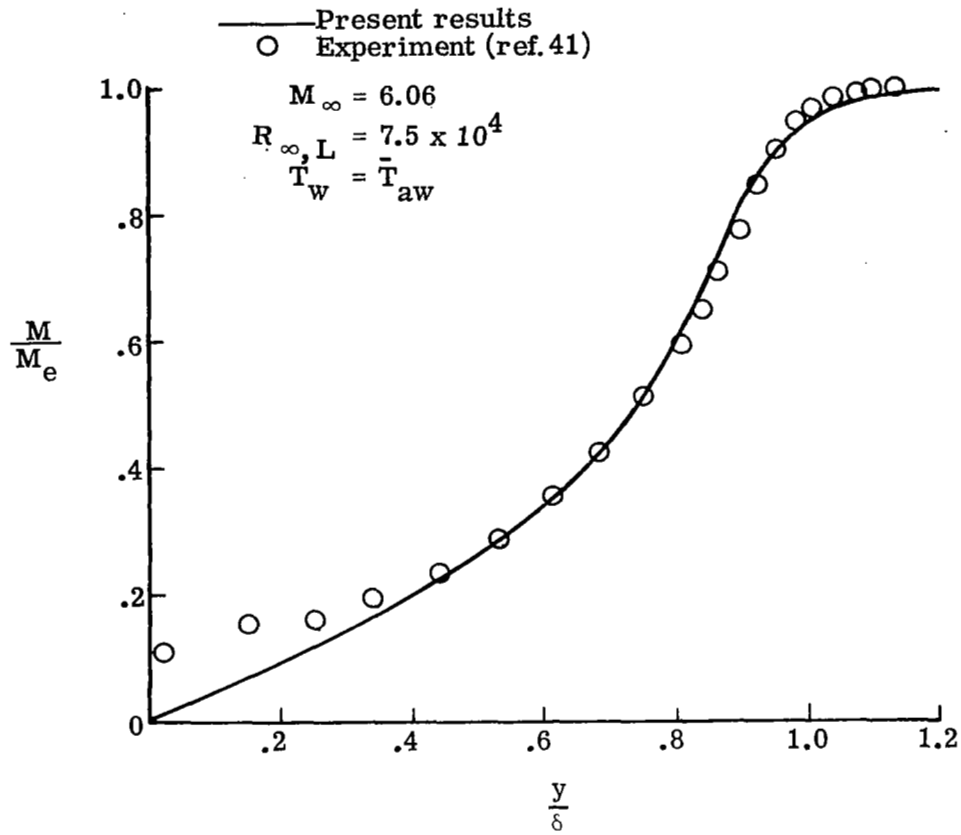

Figure 16.- Comparison of theoretical and experimental Mach number profile.

used in the flat-plate calculations. The compression-corner calculations to be discussed in the remainder of this section typically required 1500 to 3000 time cycles to converge, depending on the initial conditions.

The resulting wall pressure distributions for $T_W = T_{O,\infty}$ and $\alpha = 5.0^O$, 7.5^O, and 10.0^O are shown in figure 17, where the flat-plate distribution is based on the Lees and Probstein weak-interaction theory. It is seen that the pressure continues to decrease for some distance from the upstream position of the computational box; thereby, it is indicated that all the upstream influence of the compression corner is contained. Flow separation occurred in the 10.0^O case; and the points of separation and reattachment are denoted by S and R, respectively. It is observed that two more inflection points occur in the wall pressure distribution in the separated case than in the unseparated cases. These inflection points are the onset of the plateau region which occurs when the extent of separation is greater. The overshoot of the pressure above the inviscid level is expected since further downstream the static pressure will decrease because of the influx of streamlines having lower stagnation pressure due to shock losses.

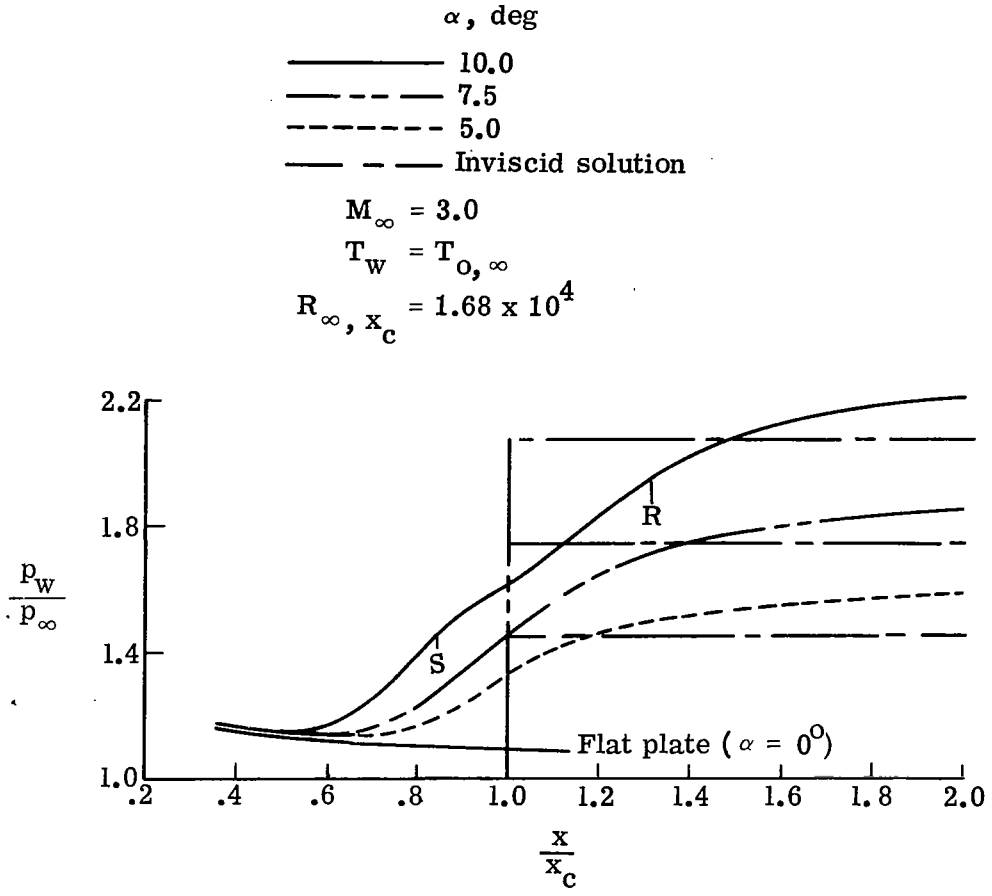

Figure 17.- Comparison of wall pressure distributions for ramp angles of 5.0°, 7.5°, and 10.0°.

Figure 18 shows the variation of the displacement thickness measured normal to the surface. The same definition of displacement thickness that was used in the flat-plate calculations is used here; however, the edge quantities are taken as those just inside of the outer boundary of the computational box. Plotting the displacement thickness in this manner gives a clear indication of the effect of the compression process on the boundary layer. Near the upstream boundary, the displacement thickness is seen to be in good agreement with that predicted by Kubota and Ko weak-interaction theory for a flat plate. Farther downstream, the upstream effects of the corner result in a rapid increase in the displacement thickness with it reaching a maximum at the corner. Past the corner, the boundary-layer edge approaches the surface until a minimum thickness is reached at the neck, after which the boundary layer continues to grow in a weak-interaction flow field at a new Mach number. It should be noted that at the corner, the displacement thickness was computed with respect to both surfaces, but the two values did not differ to within the plotting accuracy of figure 18.

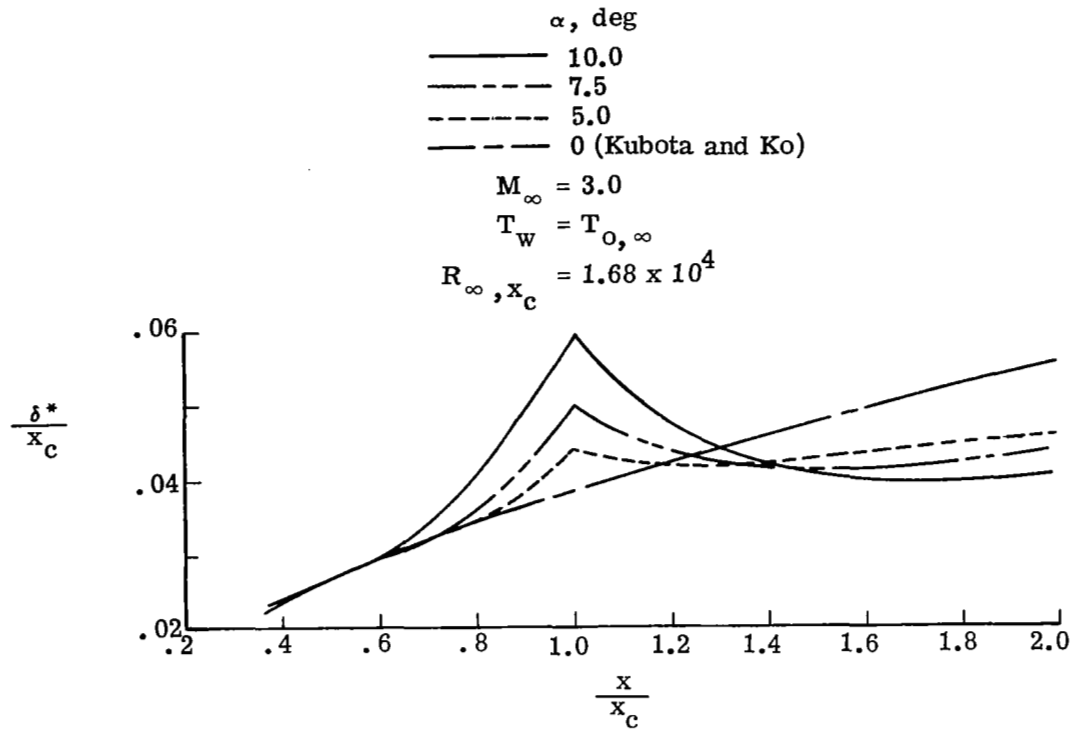

Figure 18.- Comparison of the displacement thickness measured normal to the surface for ramp angles of 5.0°, 7.5°, and 10.0°.

In figure 19, the wall skin-friction distributions for the ramp angles of 5.0°, 7.5°, and 10.0° are compared. At the corner, the skin friction is double-valued since at this point the shear stress is considered with respect to two surfaces. Also shown is the skin-friction coefficient predicted by the Lees and Probstein weak-interaction theory for a flat plate. The skin-friction distribution clearly shows the extent of the separation region for the 10.0° case. It is also seen that the 7.5° case for these flow conditions is that of incipient separation since the skin-friction coefficient is very close to zero at the corner. Comparison of figures 18 and 19 shows that the flat-plate weak-interaction estimate of the downstream skin-friction coefficient agrees with the computed results, whereas the estimated displacement thickness does not. This result is expected since, to first order, the skin-friction coefficient depends only on the square root of the Reynolds number, whereas the displacement thickness depends on both the square root of the Reynolds number and the square of the Mach number.

A computed flow-field map in the immediate region of the corner is shown in figure 20 for the $\alpha = 10.0^\circ$ case. The streamline pattern is shown inside as well as exterior to the separation bubble. There are approximately 17 grid points along the wall from separation to reattachment; thereby adequate resolution is given. In the separation bubble, the locus of $u = 0$ is shown to indicate the regions of forward and reverse flow.

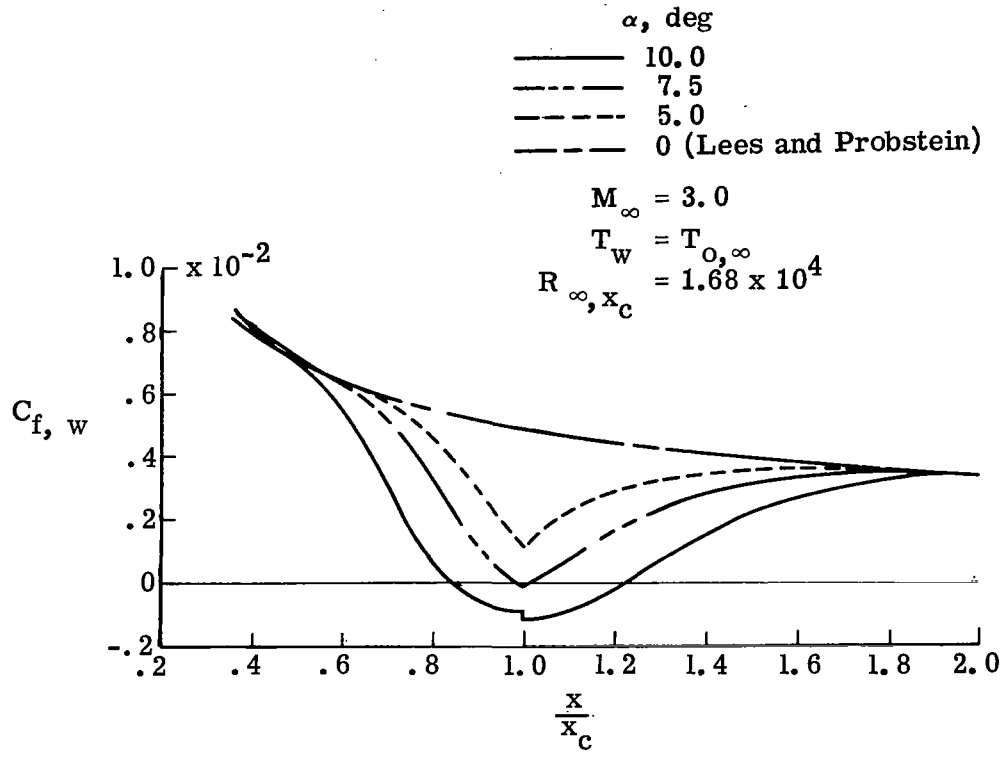

Figure 19.- Comparison of wall skin-friction distributions for ramp angles of 5.0°, 7.5°, and 10.0°.

Comparison of the values of the stream function indicate the low mass flow in the recirculation region. It is also observed that the points of separation and reattachment are not equidistant from the corner as the bubble extends farther downstream from the corner than it does upstream.

In the flow exterior to the recirculation region, the computed displacement thickness is plotted and is seen to be nearly parallel to the neighboring streamlines, which is consistent with the displacement body concept long used in boundary-layer theory. The pressure contours shown in figure 20 indicate that the pressure variations are small between the wall and the displacement thickness but larger between the displacement thickness and the boundary-layer edge. Outside the displacement thickness, the pressure contours quickly turn to follow the compression waves generated by the turning process. The pressure contours converge only slightly from the wall to the outer boundary of the computational box and hence the shock formation occurs exterior to the region of calculation.

Effect of suction.- A calculation was made for the $M_\infty = 3.0$ and $\alpha = 10.0^\circ$ case in order to determine the effect of wall suction on the compression-corner flow. Suction reduces the extent of the separated region by removing the section of the boundary layer with low total pressure; thus the boundary layer is thinned and the skin friction is

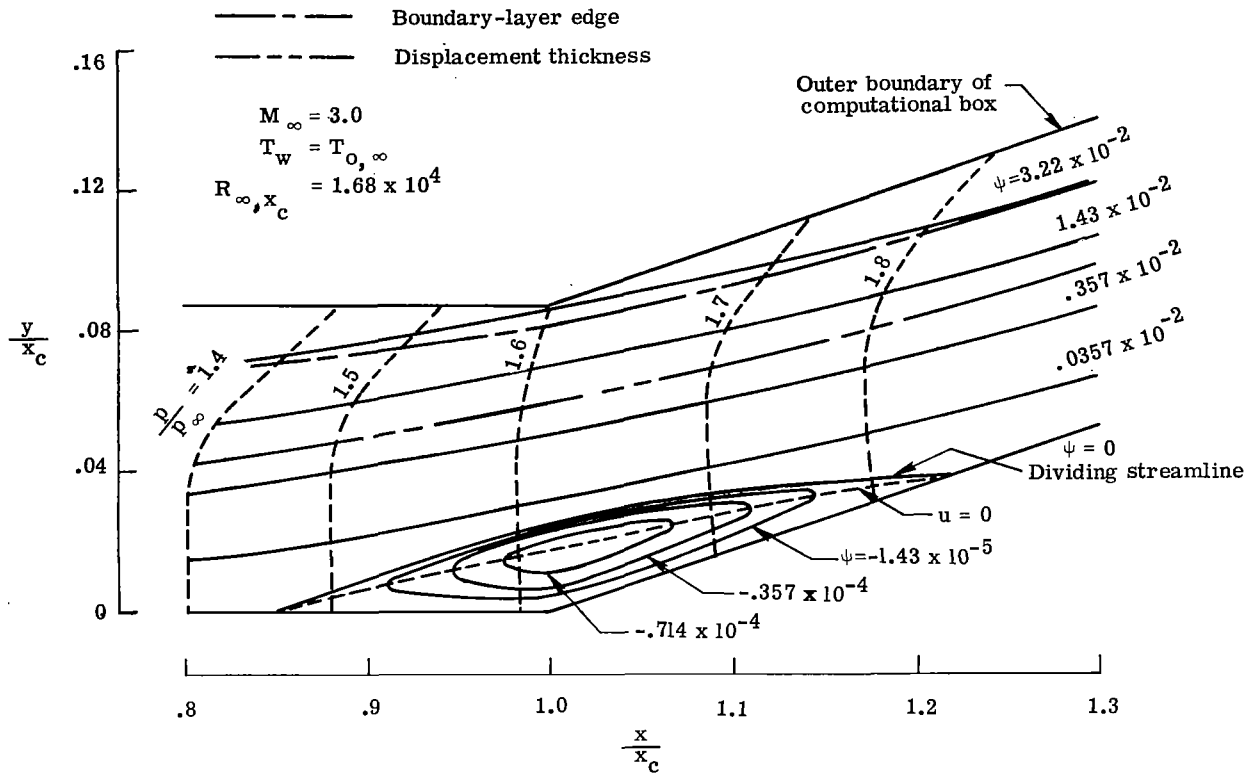

Figure 20.- Computed flow field over a 10° compression corner for $M_\infty = 3.0$.

increased. The wall suction velocity was set at $v/u_\infty = -0.01$ for $0.786 \leqq \frac{x}{x_c} \leqq 1.214$, which is a region comparable to the length of separated flow $0.84 \leqq \frac{x}{x_c} \leqq 1.22$, which was found for the same case with no suction.

The effects of the suction boundary condition are very evident in comparing the flow-field maps in figures 20 and 21. As a result of the mass removal, the pressure rise and streamline turning generated by the compression corner occur much closer to the corner. Examination of the skin-friction distribution shows that this arbitrary choice of suction velocity results in a case of incipient separation since $C_{f,w} = 0$ only at the corner. Comparison of the displacement thickness between figures 20 and 21 shows the boundary-layer thinning produced by the suction. The kinks in the streamlines at the initial station, where the suction is first applied, are nonphysical and are a numerical result of the discontinuity in the boundary conditions. It was found that with the 1-percent wall suction velocity, the amount of fluid removed in the corner region was 3.22 percent of that flowing through the upstream boundary.

Numerical tests of simple-wave extrapolation.- Several numerical tests were made to determine the errors introduced into the calculations by the simple-wave extrapolation that was used to update the boundary conditions along the outer boundary. First the tests

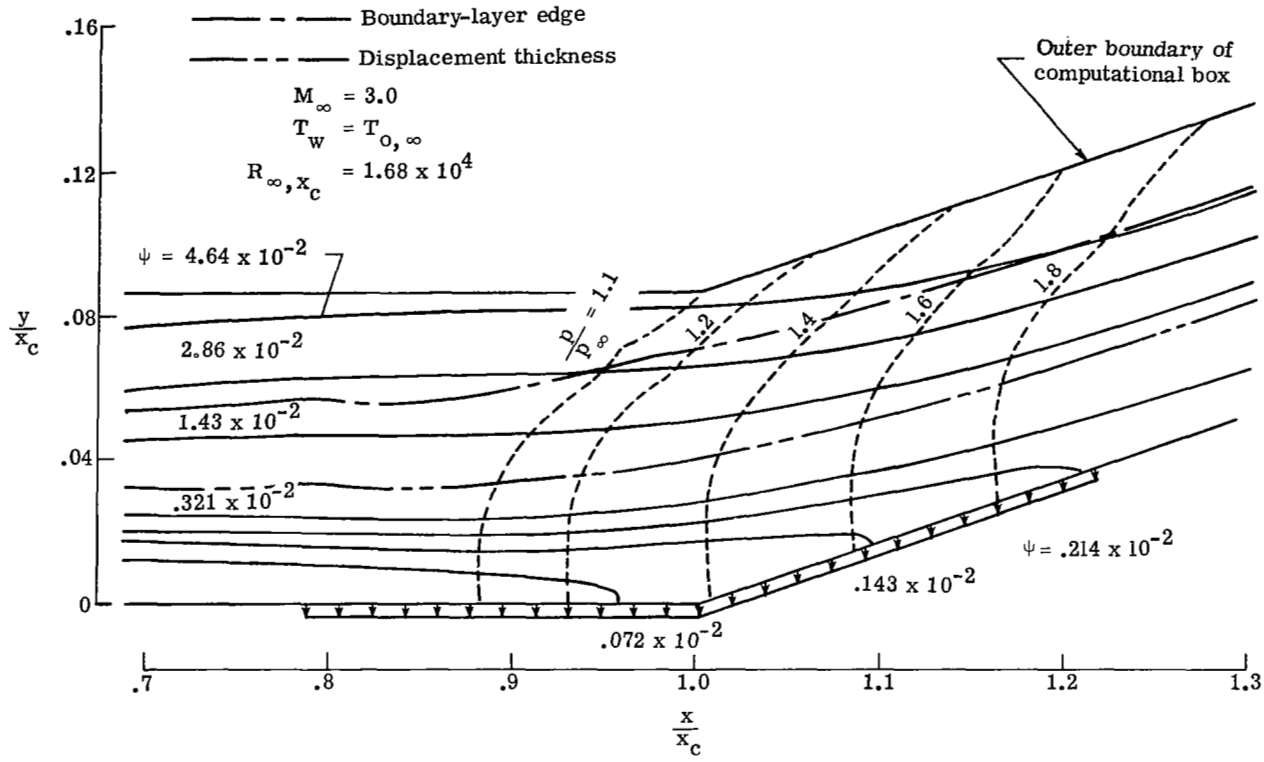

Figure 21.- Computed flow field over a 10° compression corner with a discontinuous wall-suction velocity of $v_w/u_\infty = -0.01$.

were performed on a known flow field, namely, the $M_\infty = 3.0$ flow over a flat plate shown in figure 10. Two different positions of the outer boundary, $y/L = 0.75$ and $y/L = 1.3$, were used, and the resulting pressure distributions along these lines are compared in figure 22 with the solution obtained with the outer boundary located in the free stream. In both cases, the calculations were extended upstream to $x/L = 2.0$ and downstream to $x/L = 5.0$. Several observations can be made about the results shown in figure 22. First, it is seen that the calculation with the outer boundary at $y/L = 0.75$ results in a pressure distribution (which is the extrapolated pressure) that is in excellent agreement with that given by the calculation with the exact outer boundary conditions. Comparison of the pressure distribution along $y/L = 1.3$ given by the simple-wave extrapolation with that found by using the exact outer boundary conditions indicates differences up to 5 percent. It is also seen in figure 22 that the errors introduced along $y/L = 1.3$ by the simple-wave extrapolation reflect back into the flow field as erroneous expansion waves as deduced from the pressure distribution given by this computational box along $y/L = 0.75$. The first point of influence of the outer boundary at $y/L = 1.3$ on the pressure along $y/L = 0.75$ is approximately at $x/L = 3.9$. It is seen that in the distance $3.9 \leqq \frac{x}{L} \leqq 5.0$, this calculation introduces larger errors than those accumulated by the calculation that used simple-wave extrapolation all along $y/L = 0.75$. It is not surprising that the calculation with the outer boundary at $y/L = 1.3$ introduces larger errors since, as seen in

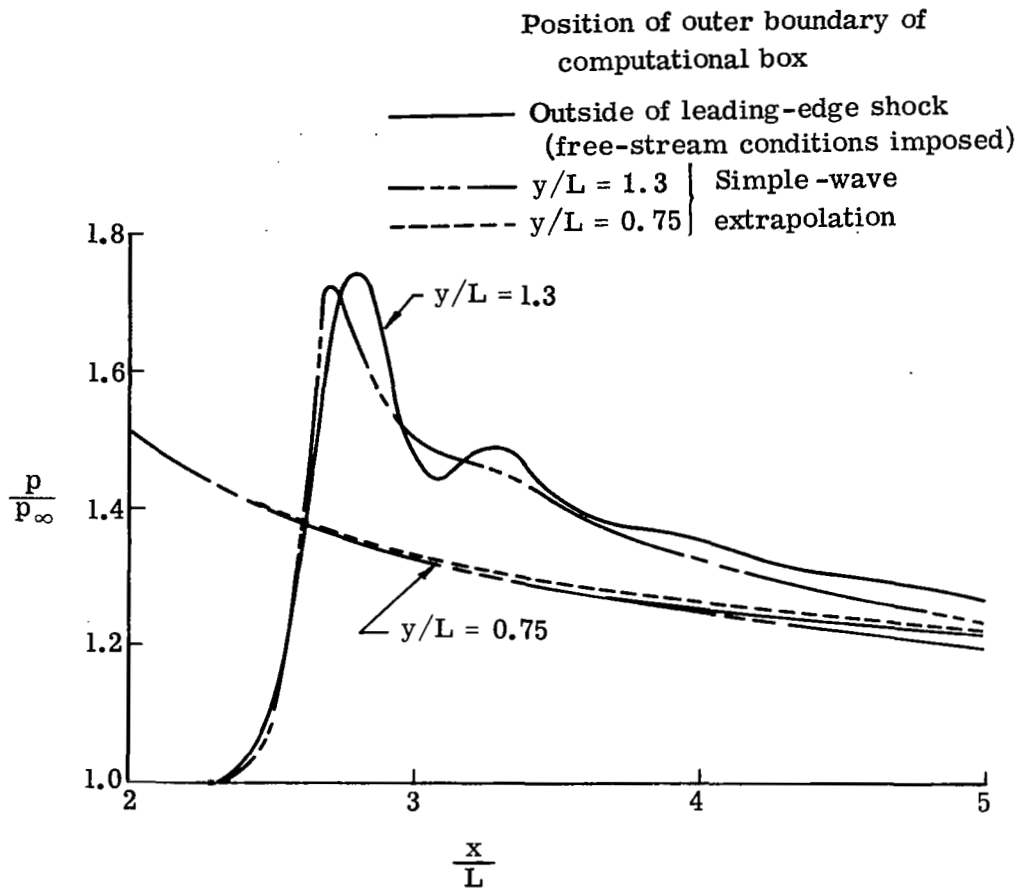

Figure 22.- Numerical tests on the use of simple-wave extrapolation at the outer boundary for a $M_\infty = 3.0$ flat-plate flow.

figure 10, this outer boundary crosses the leading-edge shock-transition region. The oscillations in the pressure distribution through the shock in figure 22 are typical of those produced by second-order finite-difference schemes. It is clear from the results that simple-wave extrapolation cannot be used successfully when the outer boundary is placed so that it crosses the shock-transition region.

Similar tests were conducted with the compression-corner calculations for $M_\infty = 3.0$ and $\alpha = 10.0^\circ$ to determine what differences result because of different positions of the outer boundary. Figure 23 shows the four computational boxes for which the calculations were made. The outer boundaries of the first two calculations were placed between the wall and the leading-edge shock, whereas the outer boundary of the third calculation was placed just outside the leading-edge shock at the upstream boundary. The outer boundary in the fourth calculation was placed further outside the leading-edge shock, and free-stream conditions were imposed up to the approximate position of the intersection of the leading-edge shock. Downstream of that point, simple-wave extrapolation was

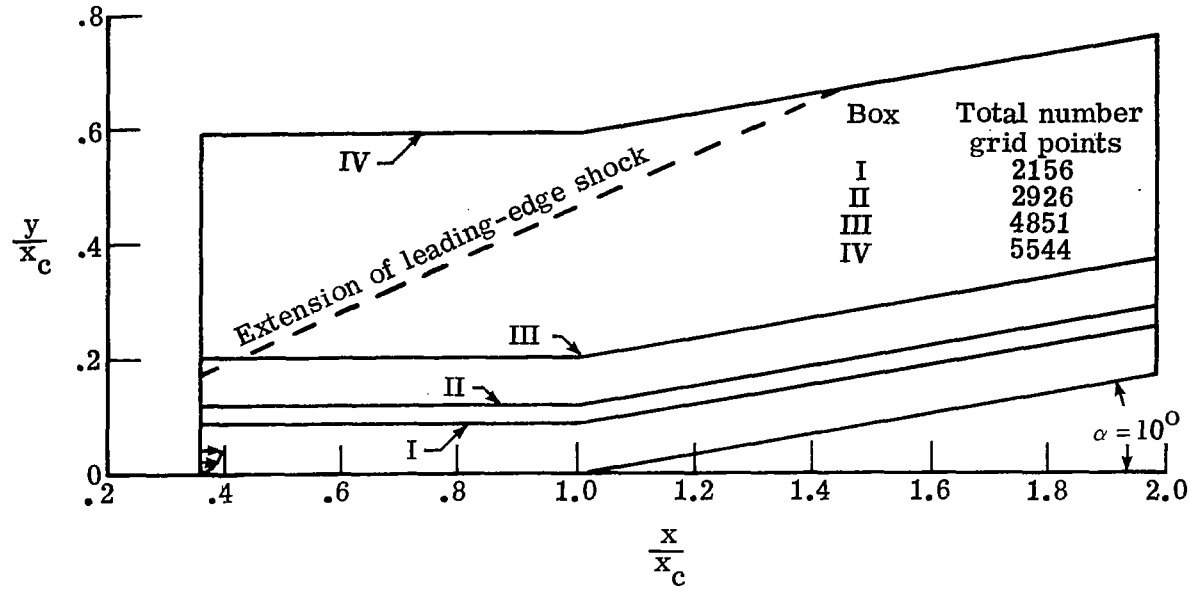

Figure 23.- Computational boxes used to test the simple-wave extrapolation for $M_\infty = 3.0$ and $\alpha = 10.0^o$.

used along the outer boundary. Any errors introduced by this extrapolation could not propagate upstream since no right-running Mach line intersected the sonic line in the boundary layer upstream of the downstream boundary. Since the boundary conditions are the most accurate in the fourth calculation, these results should be the most accurate. Box I was used for the calculations which were discussed previously. In the first three calculations the same grid spacing was used, but in the fourth calculation the following variable grid spacing was used in the y-direction in order to reduce the computer storage:

$$\left.\begin{aligned} &\frac{\Delta y}{x_c} = 0.00321 && \left(0 \leqq \frac{y}{x_c} \leqq 0.0868\right) \\ &\frac{\Delta y}{x_c} \text{ expands at 10 percent} && \left(0.0868 \leqq \frac{y}{x_c} \leqq 0.199\right) \\ &\frac{\Delta y}{x_c} = 0.0136 && \left(0.199 \leqq \frac{y}{x_c} \leqq 0.59\right) \end{aligned}\right\} \quad (39)$$

Figure 24 presents the wall pressure distributions which resulted from the four calculations. It is seen that the differences shown here are consistent with those found in the tests made with the flat-plate calculations. The pressure distribution produced by box III is clearly in error since the overall pressure rise is less than the inviscid value. The underestimation of the pressure also occurred in the flat-plate tests when simple-wave extrapolation was used in the shock-transition region. Without the fourth calculation to serve as a reference, it is not as simple to deduce which of calculations one or

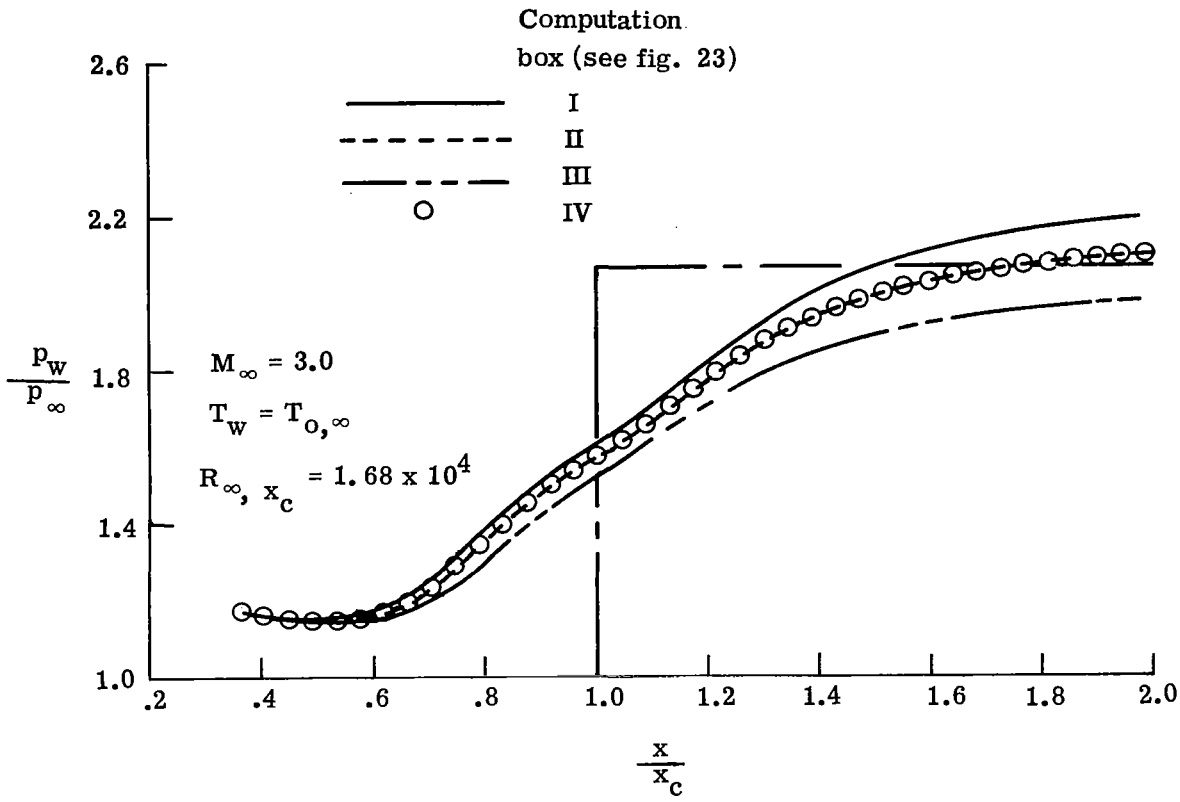

Figure 24.- Comparison of wall pressure distributions for three positions of the outer boundary of the computational box.

two is the more correct; hence, this difference is indicative of the uncertainty introduced into the calculations by the simple-wave extrapolation at the outer boundary.

$M_\infty = 4.0$ Compression-Corner Calculations

In this section, calculations are discussed that were made for the $M_\infty = 4.0$ flow over a 10^o adiabatic compression corner for which Lewis, Kubota, and Lees (ref. 11) experimentally obtained wall pressure distributions. The Reynolds number based on the free-stream conditions and the distance from the leading edge to the corner was $R_{\infty,x_c} = 6.8 \times 10^4$. Considerable care was taken in the experiment to insure that the flow was two dimensional and that transition to turbulence occurred downstream of reattachment.

The computational box which was used in the calculations extends from $x/x_c = 0.38$ to $x/x_c = 2.11$ with the outer boundary placed at a constant distance of $0.109x_c$ from the wall. In the x-direction 121 grid points were used and a grid spacing of $\Delta x/x_c = 0.01442$ was obtained; in the y-direction 36 grid points were used and a grid spacing of $\Delta y/x_c = 0.002885$ was obtained. An attempt was made to reduce the total number of

grid points by increasing Δx by 33 percent; however, the resulting calculation was unstable since large oscillations developed in the corner region.

The upstream boundary conditions were established by a series of calculations from the leading edge similar to those discussed previously for the $M_\infty = 3.0$ and $M_\infty = 6.06$ flow fields. Details of these calculations are discussed by Carter (ref. 18). The wall temperature was held constant at $\overline{T}_{aw}$ as determined by equation (38).

Comparison with experiment.- Comparison of the numerical wall pressure distributions with those measured by Lewis et al. are shown in figure 25. The experimental data is both from a flat-plate model which spanned the wind tunnel (no side plates) and from an axisymmetric model (stovepipe) which consisted of a cylinder-flare configuration. These two sets of experimental data agree very well except downstream of the reattachment region where the axisymmetric pressure distribution begins to drop toward the asymptotic cone pressure.

The agreement between the numerical calculation and the experiment is good although downstream of the corner it is seen that the theoretical values are higher. The theoretical solution overshoots the inviscid solution; this result is expected based on

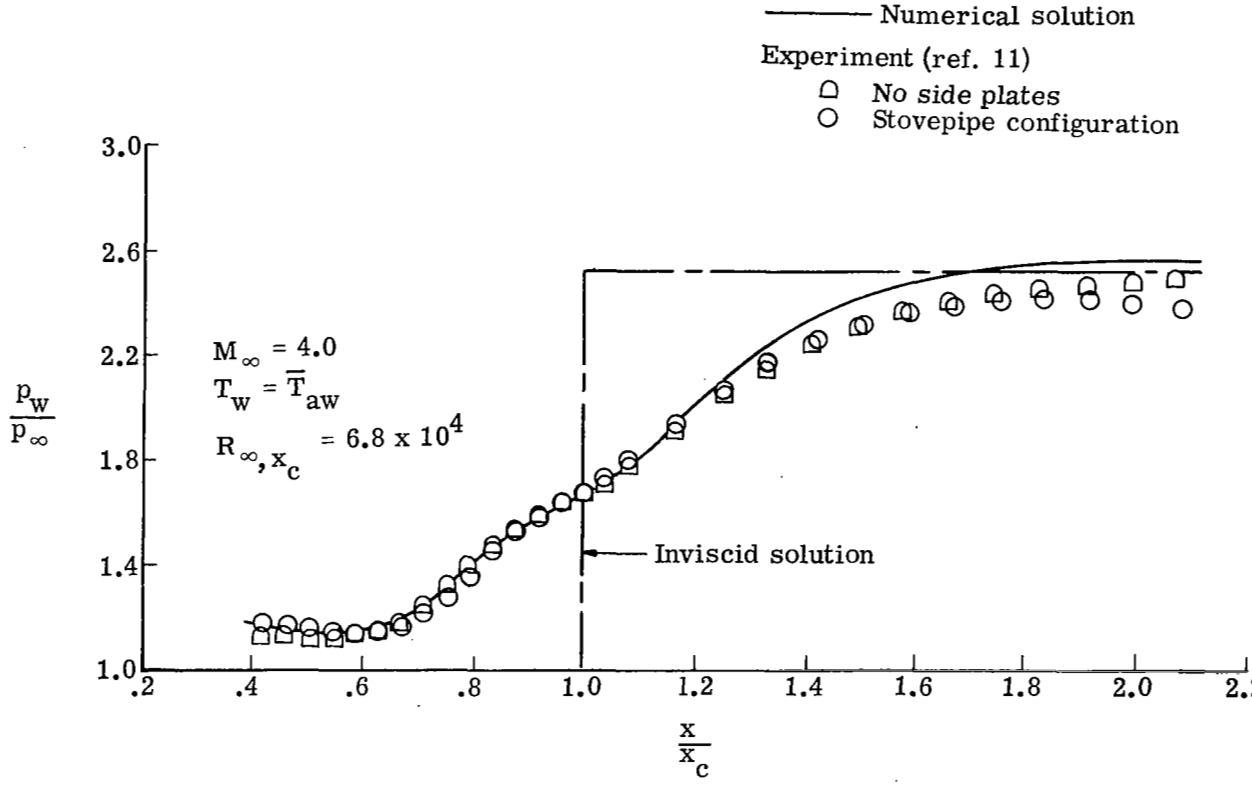

Figure 25.- Comparison of numerical and experimental wall pressure distributions.

previous discussion. Calculations were made for two other computational boxes to show that the errors introduced by the simple-wave extrapolation are of comparable magnitude to those found in the $M_\infty = 3.0$ calculations previously discussed. These calculations also verified that the upstream influence of the corner was contained in the computational box. For further details of these calculations, see Carter (ref. 18).

Figure 26 shows a flow-field map of the streamline and pressure contour pattern in the immediate vicinity of the corner. Comparison of figure 26 with the flow-field map for the $M_\infty = 3.0$ case shown in figure 20 shows that the outer boundary of the computational box was placed farther from the wall in the $M_\infty = 4.0$ case. The pressure contours near this outer boundary indicate that no shocks have formed interior to the computational field. However, in figure 26, the contours are converging and, judging from the relatively large distance between the 1.6 and 1.7 pressure contours, it appears that distinct separation and reattachment shocks are beginning to form. As was seen in the $M_\infty = 3.0$ case, the mass flow in the separation bubble is very small compared with that in the free-shear layer, although their thicknesses are comparable.

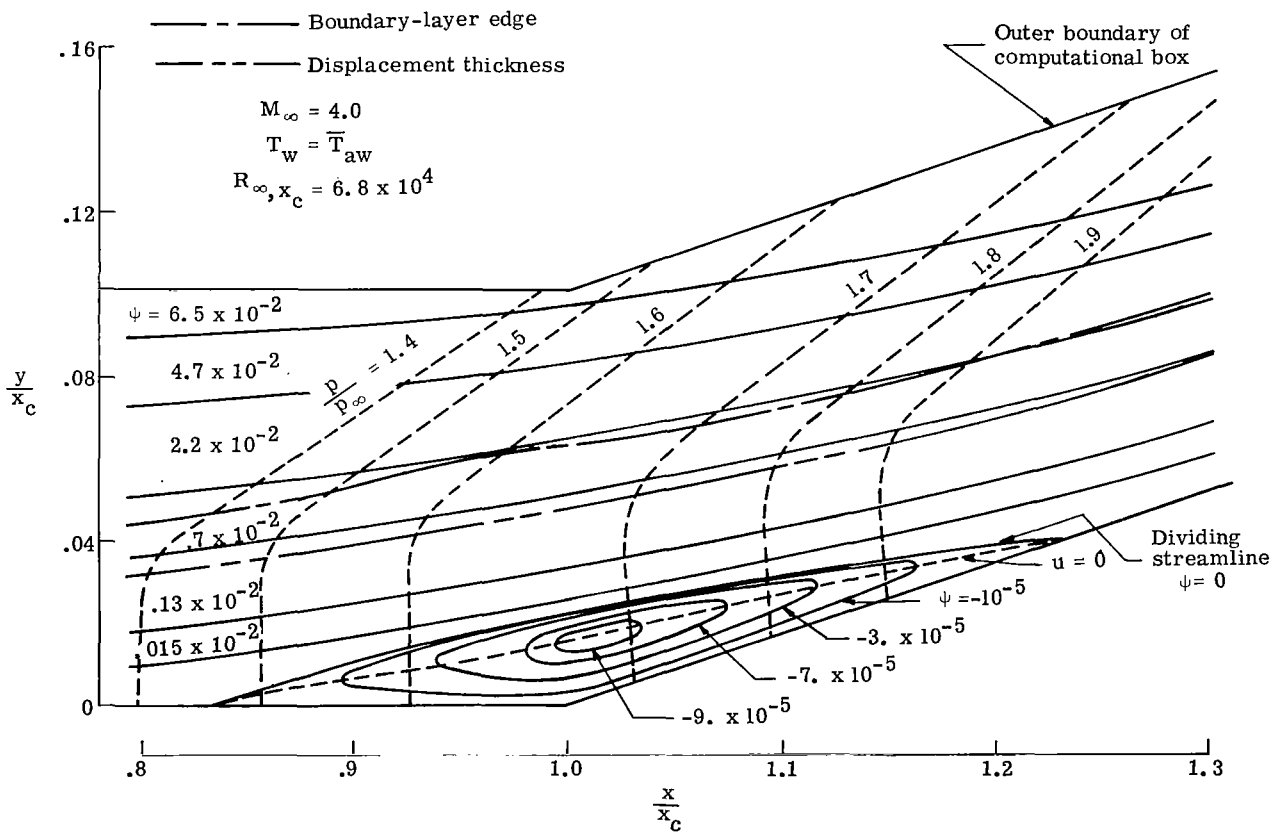

Figure 26.- Computed flow field over a 10° compression corner for $M_\infty = 4.0$.

Profiles of flow properties.- In figure 27, profiles of the two velocity components, temperature, and density are shown at three stations upstream and downstream of the corner. In each case, the profiles are normal to the surface with the velocity components parallel and perpendicular to the ramp denoted as u' and v', respectively. These profiles show the general characteristics of the compression-corner flow field. Figure 27(a) shows the large deceleration of the flow near the wall which results in flow separation at $x/x_c = 0.827$ as evidenced by the vertical slope of this profile at the wall. At the corner, it is seen that the maximum reverse-flow velocity is about 2 percent of the free-stream velocity. Also seen in figure 27(a) is the acceleration which occurs in the boundary layer after the corner as the flow returns to a normal state of weak interaction at the new Mach number. The traverse velocity profiles in figure 27(b) are indicative of the turning of the flow. The decrease in v in the outer part of the profile is due to the fact that the outer streamlines have not been turned as much as the streamlines closer to the surface.

Figure 27(c) shows that the temperature in the separation bubble differs only slightly from the wall temperature which is expected in view of the low velocities and small nor-

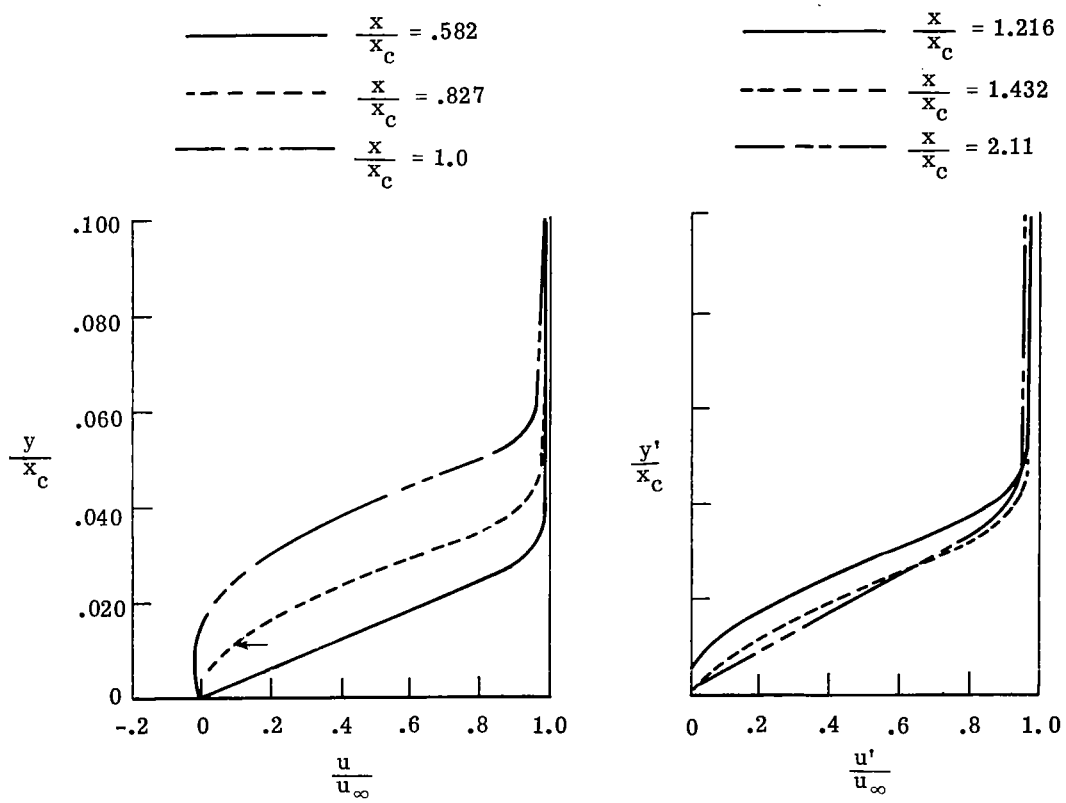

(a) u and u' component of velocity.

Figure 27.- Profiles of flow properties upstream and downstream of the corner. $M_\infty = 4.0$; $R_{\infty,x_c} = 6.8 \times 10^4$; $\alpha = 10.0^\circ$; and $T_w = \overline{T}_{aw}$. Arrow indicates thickness of Stewartson inner layer for the profile at $\frac{x}{x_c} = 0.827$.

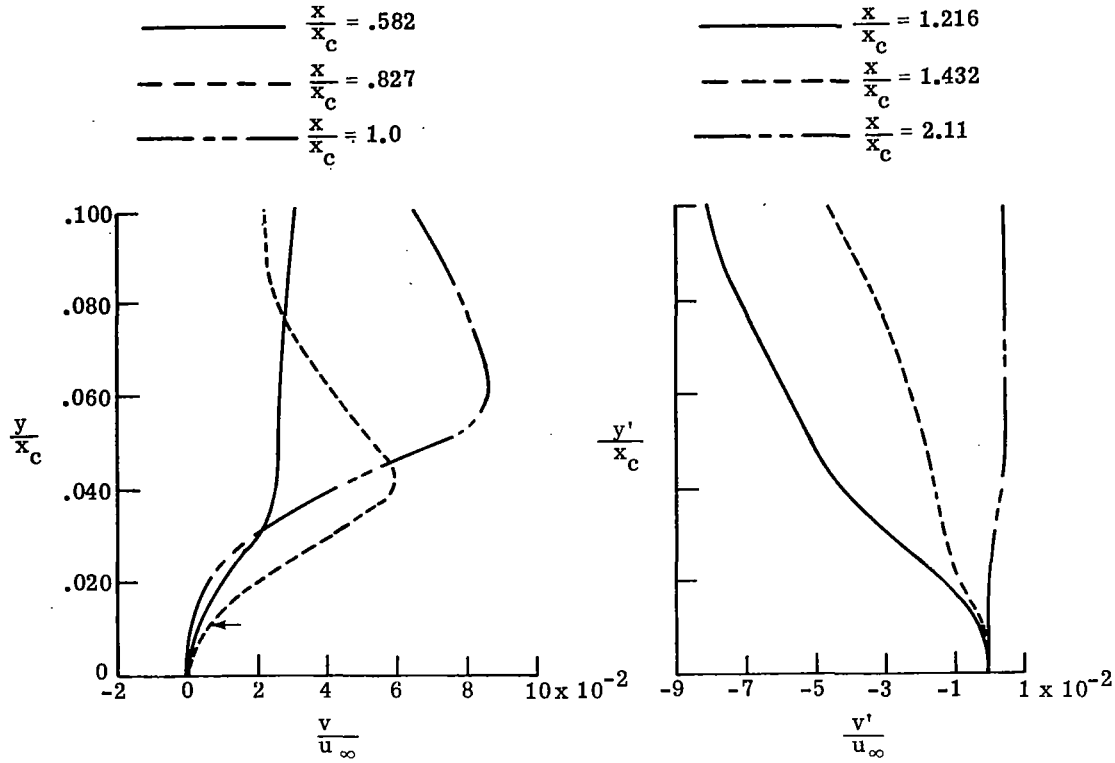

(b) v and v' component of velocity.

Figure 27.- Continued.

mal pressure gradient in this region. The use of a constant wall temperature for the approximate adiabatic wall condition is verified by the near-vertical slope of the temperature profiles in figure 27(c). The wall heat transfer for each profile is less than 1 percent of the maximum heat transfer in the boundary layer.

The profiles shown in figure 27 verify, qualitatively at least, the theoretical analysis of Stewartson and Williams (ref. 9) which was briefly discussed in the "Introduction." A key feature of their analysis is the existence of an inner boundary layer near the surface where the velocity change is substantial but density changes are small. The inner layer is adjacent to the main boundary layer where the u profile is similar in shape to that of the unperturbed boundary layer upstream of the ramp. Stewartson and Williams (ref. 9) found the thickness of the inner layer to be $0(\epsilon^5) = 0\left(R_{\infty,x_0}^{-5/8}\right)$ where R_{∞,x_0} is the Reynolds number based on free-stream conditions and the distance from the leading edge to the start of the interaction. In constructing a universal form of the variables for the inner region, an amplification of the effective value of ϵ, through a scaling dependent on Mach number, results in the thickness of the inner region being of the order

$$\frac{y}{x_o} \approx \frac{\left(\frac{T_w}{T_\infty}\right)^{3/2} R_{\infty,x_o}^{-5/8}}{(0.332)^{3/4}\left(M_\infty^2 - 1\right)^{1/8}} \tag{40}$$

Using equation (40) together with the present conditions and $x_o/x_c = 0.582$ results in an estimate of $y/x_c = 0.011$ for the inner region thickness. In figure 27(d), the density profile at $x/x_c = 0.827$, which is at separation and is within the region of applicability of the Stewartson and Williams analysis, shows that this estimate is the correct order of magnitude for the lateral extent of the constant-density inner region. Since the pressure changes are small, the temperature changes are also small in this region, as seen in figure 27(c). Thus, the numerical results tend to verify Stewartson and Williams' use of the incompressible boundary-layer equations in this inner region.

The streamwise velocity perturbation in the main boundary layer was estimated by Stewartson and Williams to be of the order

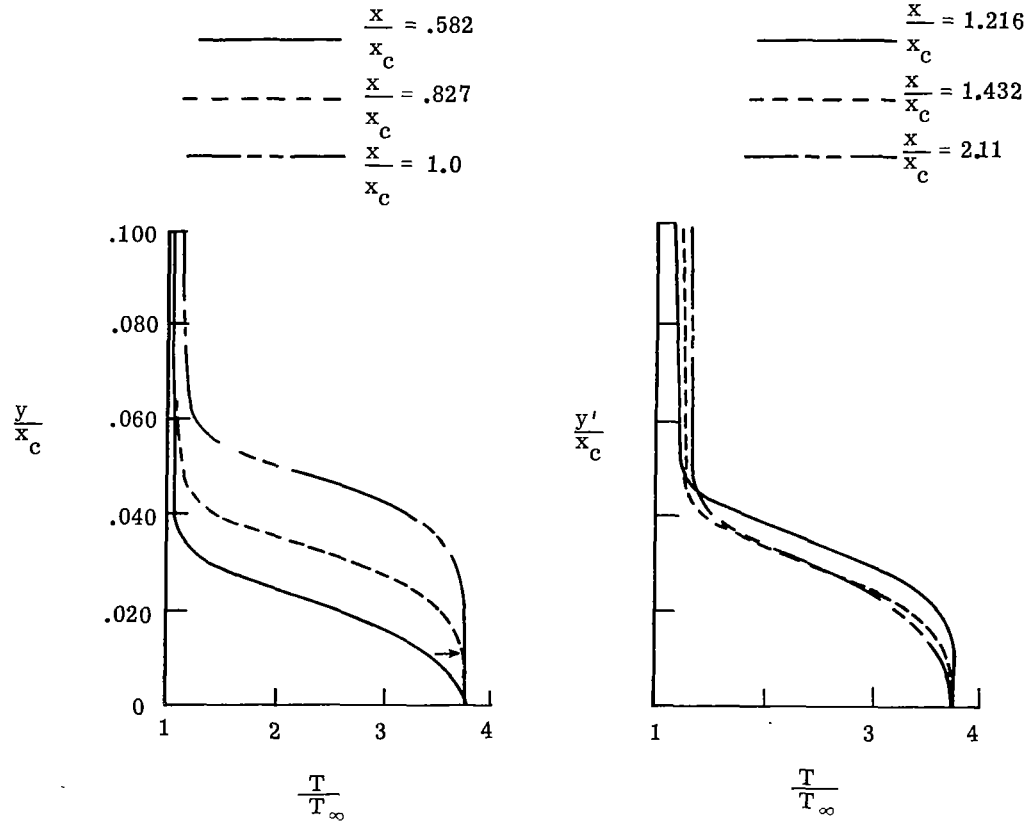

(c) Temperature.

Figure 27.- Continued.

$$\frac{\Delta u}{u_\infty} \approx \epsilon = R_{\infty,x_0}^{-1/8} \tag{41}$$

which for the present conditions results in $\Delta u/u_\infty \approx 0.27$. The amplification of the velocity scaling due to the Mach number dependence was small and therefore was deleted. Figure 27(a) shows this estimate to be the correct order of magnitude for the difference between the profile at separation ($x/x_c = 0.827$) and the profile at the upstream start of the interaction ($x/x_c = 0.582$). Similarly, the normal velocity at the outer edge of the inner region is of the order

$$\frac{v}{u_\infty} \approx \epsilon^3 = R_{\infty,x_0}^{-3/8} \tag{42}$$

whereas in the main boundary layer the normal velocity increases to

$$\frac{v}{u_\infty} \approx \epsilon^2 = R_{\infty,x_0}^{-1/4} \tag{43}$$

For $R_{\infty,x_0} = 3.93 \times 10^4$, equations (42) and (43) result in nondimensional normal velocities of the order of 0.02 and 0.07 at the outer edges of inner region and the main boundary layer, respectively. This estimate agrees well with the normal-velocity profile at separation shown in figure 27(b).

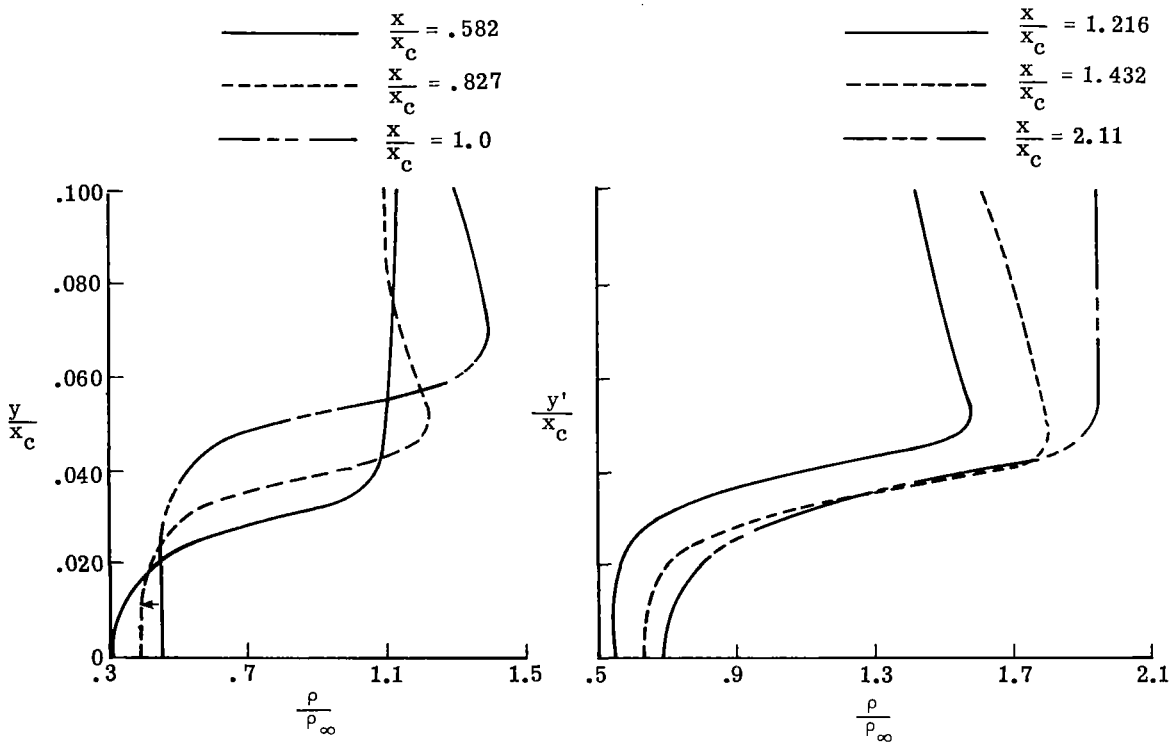

(d) Density.

Figure 27.- Concluded.

$M_\infty = 6.06$ Compression-Corner Calculations

Calculations were made for the $M_\infty = 6.06$ flow over a 10.25° adiabatic compression corner for which Lewis, Kubota, and Lees (ref. 11) also obtained experimental measurements for several Reynolds numbers. For $R_{\infty,x_c} = 1.5 \times 10^5$, Lewis et al. judged the flow to be laminar and established the repeatability of the surface pressure distribution within several percent. Therefore, this case was chosen for the present calculations.

The computational box used in the calculations extends from $x/x_c = 0.5$ to $x/x_c = 2.1$ and from the wall to $y/x_c = 0.105$. The x- and y-grid spacings were $\Delta x/x_c = 0.0125$ and $\Delta y/x_c = 0.003$, respectively, and resulted in 4644 grid points. It is observed that this grid spacing is comparable to that used in the $M_\infty = 4.0$ calculation. This spacing was used since the boundary-layer thickness is approximately the same in both cases because of the compensating effects of increasing the Mach number and Reynolds number. The position of the outer boundary of the computational box was far enough from the wall to allow for the boundary-layer growth, but did not cross the separation or reattachment shocks determined experimentally from pitot measurements. Simple-wave extrapolation was used along the outer boundary except in the region $0.5 \leqq \frac{x}{x_c} \leqq 0.667$ where the conditions were known from the flat-plate flow field determined in computational box V which is shown in figure 11. The flow along this part of the outer boundary is not influenced by the compression-corner flow field. Tests were not made on the simple-wave extrapolation since it was presumed that the errors would be comparable to those found previously.

Figure 28 shows a comparison of the wall pressure distribution determined from the present calculations with that found experimentally. Upstream of the corner, the present solution and the experiment predict approximately the same degree of compression when the upstream pressure difference is taken into account. Downstream of the corner, the agreement becomes better as the effects of the upstream pressure difference become smaller. Also shown for comparison is the theoretical result obtained by Klineberg and Lees (ref. 42) by using an integral method on the boundary-layer equations. Their result agrees well with the experiment at the start of the interaction, but downstream it falls below the experimental distribution; as a result, a longer interaction region is indicated.

In figure 29 a comparison between the present results and experiment is shown for Mach number profiles at various stations downstream of the corner. In the experiment, the boundary-layer thickness was defined on the basis of a pitot profile as is shown in figure 15. In order to be consistent, this definition was also used in plotting the present results in figure 29. The agreement obtained in figure 29 is reasonably good, particularly at $x/x_c = 1.2$, which is slightly upstream of reattachment, and at $x/x_c = 2.0$;

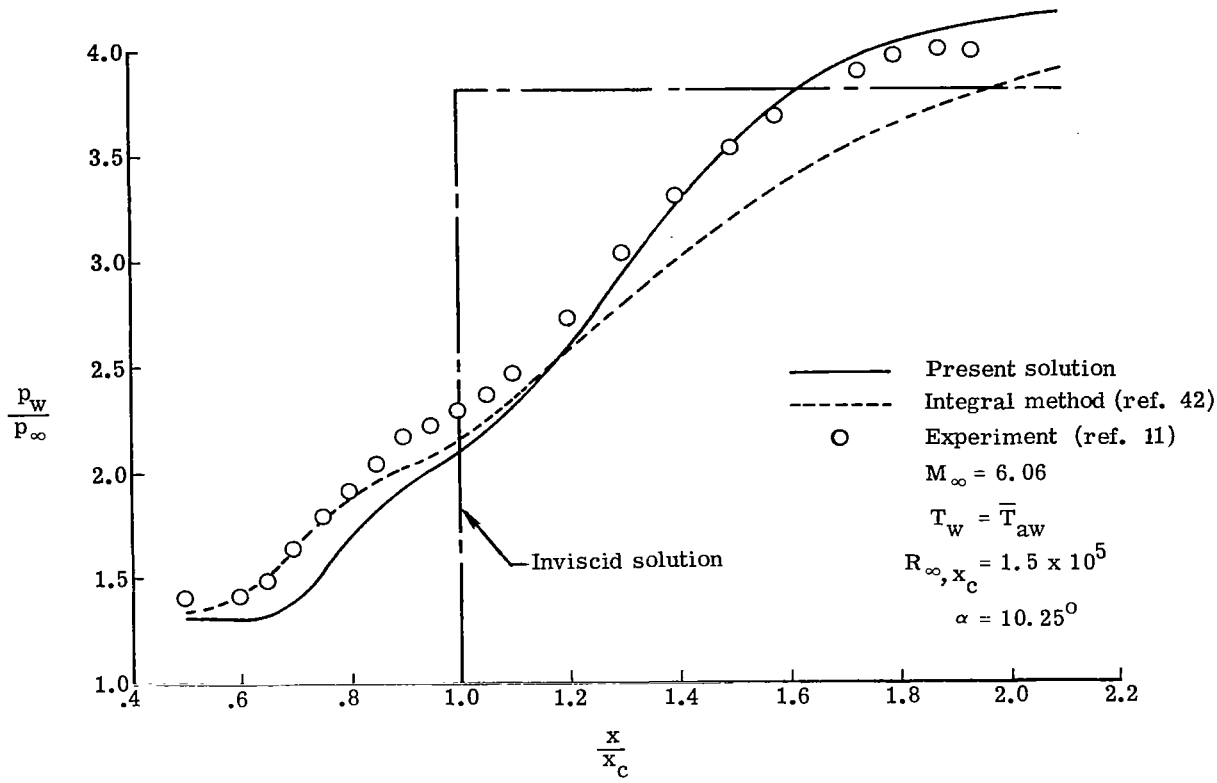

Figure 28.- Comparison of theoretical and experimental wall pressure distributions.

at $x/x_c = 1.6$ the differences in the experimental and theoretical profiles are greater. In the experiment, correction was made where necessary to the pitot measurements because of the effects of low Reynolds numbers.

In figure 30 the skin-friction distribution obtained in the present investigation is compared with that found by Klineberg (ref. 43) by using an integral method. The points of separation and reattachment predicted by these two approaches differ by about 5 percent of the distance from the leading edge. Their locations were not determined experimentally. Elsewhere, the agreement is reasonably good up to the reattachment region; however, downstream of that region, the two distributions differ considerably. The difference is consistent with that in figure 28 in that the integral approach shows the interaction to extend farther downstream than that found in the present investigation.

Murphy (ref. 7) found similar results in comparing the results of three boundary-layer approaches (including that of Klineberg and Lees) to experiment. For example, in comparing the wall skin friction with that measured by Hakkinen et al. (ref. 23) for the case of an incident shock onto a boundary layer for $M_\infty = 2.0$, it was found that the extent of the separated region was overpredicted by all three methods and that downstream of

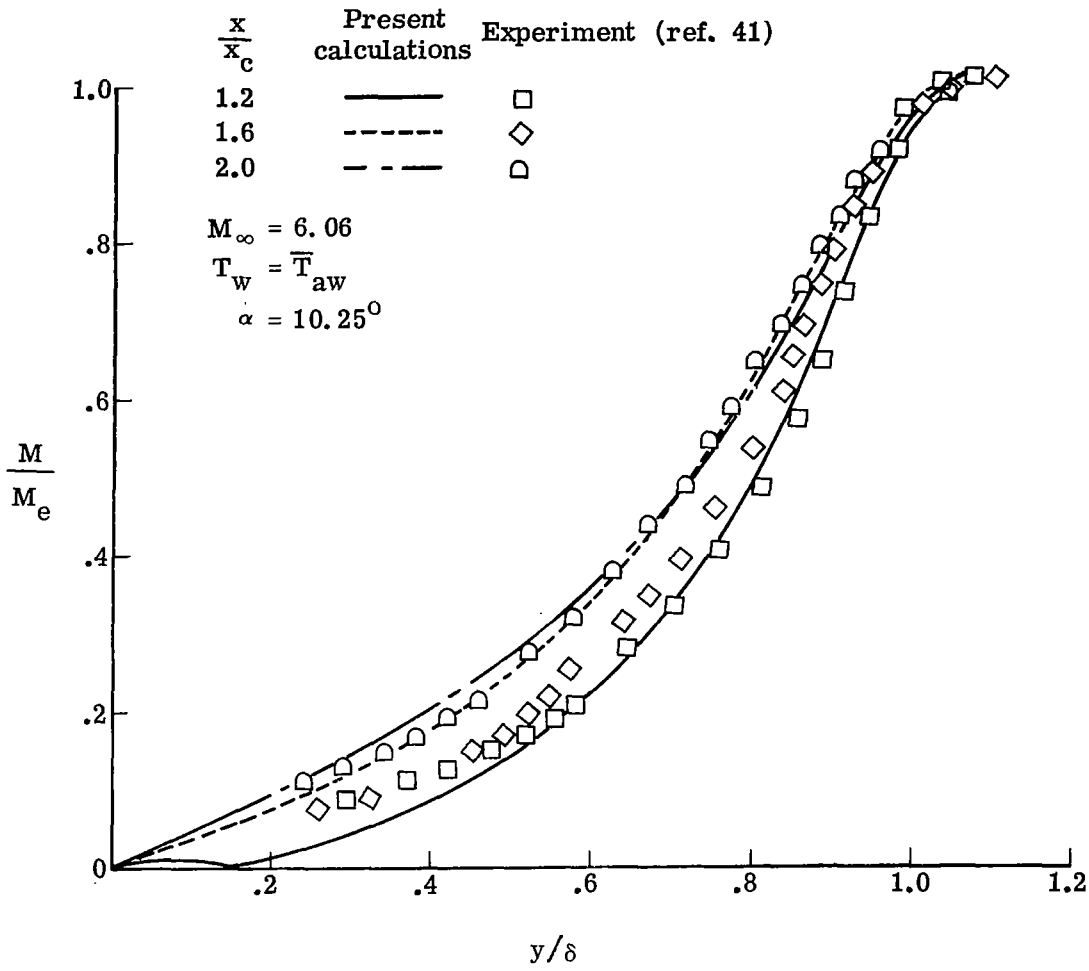

Figure 29.- Comparison of numerical and experimental Mach number profiles.

reattachment, the skin friction was underpredicted. Later calculations were made by MacCormack (ref. 21) by use of the Navier-Stokes equations for the same case and good agreement was obtained with the measured skin friction.

Comparison With Oswatitsch's Analysis

Oswatitsch (ref. 44) used Taylor series expansions of the Navier-Stokes equations in the vicinity of a separation point to show that the separation streamline (also referred to as the dividing streamline) leaves the surface at an angle given by

$$\beta_D = \tan^{-1} \frac{3\left|\frac{\partial \tau}{\partial x}\right|}{\partial p/\partial x} \tag{44}$$

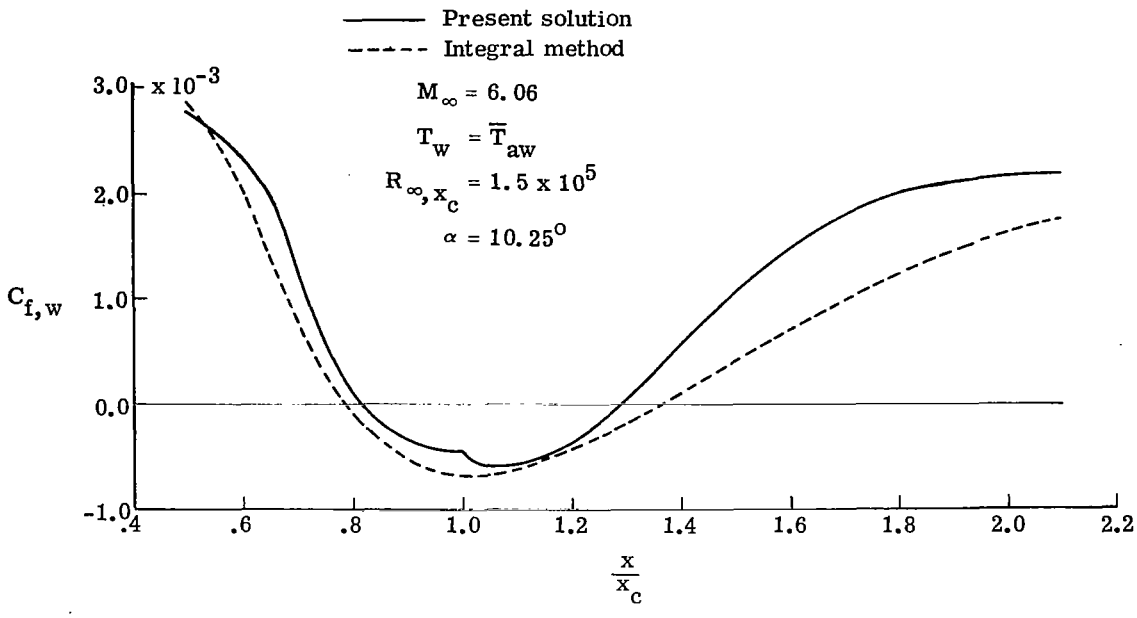

Figure 30.- Comparison of wall skin-friction coefficient obtained from the Navier-Stokes equations with that from the boundary-layer equations.

In addition, his analysis showed that the locus of $u = 0$ is a straight line near the separation point inclined to the surface by the angle

$$\beta_u = \tan^{-1} \frac{2\left|\frac{\partial \tau}{\partial x}\right|}{\partial p / \partial x} \tag{45}$$

Hence, for small angles, $\beta_u = \frac{2}{3} \beta_D$. Figure 31 shows a schematic diagram of the streamline pattern near separation with the angles β_u and β_D indicated. The analysis at reattachment is identical if the arrows in figure 31 are reversed.

Table I shows a comparison between the angles obtained from the calculation and those from equations (44) and (45), by use of the present numerical results to estimate the shear stress and pressure gradients. With a few exceptions, the differences are less than 10 percent; thereby, the results are verified to be consistent with Oswatitsch's analysis.

Free-Interaction Analysis

Lewis, Kubota, and Lees (ref. 11) correlated their data for the free-interaction region by using the scaling laws of Chapman, Kuehn, and Larson (ref. 10) and Curle (ref. 45). Curle's scaling is more general since it includes the effect of a nonadiabatic wall, but reduces to that of Chapman et al. in the adiabatic case. In Curle's scaling, the pressure is given by

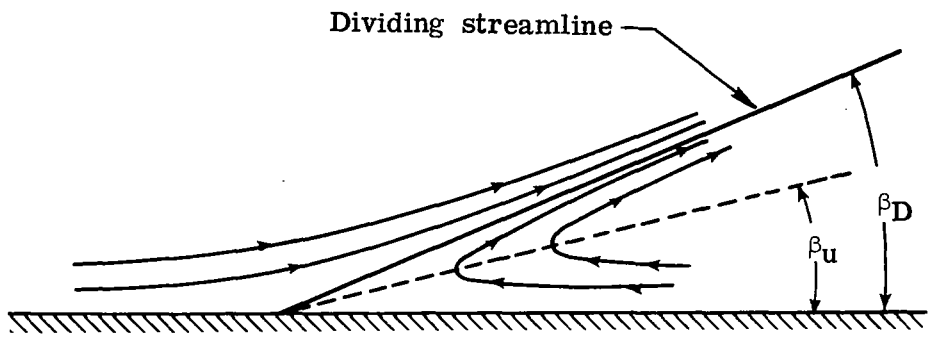

Figure 31.- Schematic diagram of the streamline pattern near separation identifying the Oswatitsch angles.

TABLE I.- COMPARISON OF CALCULATED ANGLES OF DIVIDING STREAMLINE AND $u = 0$ LINE WITH THOSE ESTIMATED BY OSWATITSCH'S THEORY FROM THE PRESENT NUMERICAL RESULTS

M_∞	β_D		β_u	
	Oswatitsch	Calculated	Oswatitsch	Calculated
Separation				
3.0	10.6	10.1	7.1	6.5
4.0	9.2	10.0	6.2	6.5
6.06	10.3	9.1	6.9	6.5
Reattachment				
3.0	9.0	11.0	6.0	7.4
4.0	7.6	7.0	5.1	4.2
6.06	6.0	6.5	4.0	4.1

$$P = \frac{C_{p,o}\left(M_o^2 - 1\right)^{1/4}}{\sqrt{C_{f,o}}} \tag{46}$$

and the length scale by

$$X \propto \frac{x - x_o}{x_o}\left(\frac{T_w}{T_e}\right)_o^{-1}\left(M_o^2 - 1\right)^{1/4} R_{o,x_o}^{1/4} \tag{47}$$

where the subscript o refers to the flow conditions at $x = x_o$. The flow conditions at $x = x_o$ differ from those at infinity due to the flat-plate weak interaction; hence, Lewis et al. used the Lees and Probstein weak-interaction analysis to relate the flow at $x = x_o$ to the free-stream values. As a result, equation (46) becomes

$$P = 1.752\,\frac{p - p_o}{p_o}\,\frac{1}{\sqrt{\bar{\chi}_{\infty,o}}}\left[1 + \frac{3\gamma - 1}{4} M_\infty\left(\frac{d\delta^*}{dx}\right)_o + O\left(M_\infty \frac{d\delta^*}{dx}\right)_o^2\right] \tag{48}$$

and equation (47) becomes, after inserting the same constant of proportionality used by Lewis et al.,

$$X = 0.311\,\frac{x - x_o}{x_o}\sqrt{\frac{1}{\bar{\chi}_{\infty,o}}}\,M_\infty^2\left(\frac{T_w}{T_\infty}\right)^{-1}\left[1 - \frac{5 - 3\gamma}{4} M_\infty\left(\frac{d\delta^*}{dx}\right)_o + O\left(M_\infty \frac{d\delta^*}{dx}\right)_o^2\right] \tag{49}$$

The variation of the displacement thickness is found from first-order boundary-layer theory which gives

$$\frac{\delta^*}{x}\sqrt{R_{\infty,x}} = \sqrt{C_\infty}\left(1.937\,\frac{T_w}{T_\infty} + 0.578\,\frac{\gamma - 1}{2} M_\infty^2 - 0.207\right) \tag{50}$$

Comparison of the experimental correlation found by Lewis et al. and the present results for $M_\infty = 3.0$, 4.0, and 6.06 is shown in figure 32. In converting the numerical results to the correlation plot, the definition of x_o used was that employed by Lewis (ref. 41), which is shown graphically in that reference. The agreement between the present results and the correlation is good, although the $M_\infty = 6.06$ pressure distributions are underpredicted by the $M_\infty = 3.0$ and $M_\infty = 4.0$ correlated results. This difference is probably due to the use of a linear pressure-deflection relationship used in deriving equation (46), which neglects terms of $O\left(M_\infty \frac{d\delta^*}{dx}\right)^2$.

A second comparison of the present results was made with the universal pressure distribution of Stewartson and Williams (ref. 9) for the free-interaction zone. In their analysis, the pressure is given by

$$\tilde{p}_2 = \frac{\left(M_o^2 - 1\right)^{1/4}\left(\frac{p}{p_o} - 1\right)}{\left(\frac{C_{f,o}}{2}\right)^{1/2} \gamma M_o^2} \tag{51}$$

and the length scale by

$$\tilde{X} = \frac{\left(M_o^2 - 1\right)^{3/8} R_{o,x_o}\left(\frac{C_{f,o}}{2}\right)^{5/4} \frac{x - x_o}{x_o}}{\left(\frac{T_w}{T_e}\right)_o^{3/2} C} \tag{52}$$

Figure 33 shows the comparison between the present results plotted in these coordinates and the numerical distribution obtained by Stewartson and Williams. The $\tilde{X}$-coordinate has been translated so that the separation point is at the origin. The start of the interaction x_o was defined in this comparison as the point upstream of the corner where the pressure was a minimum.

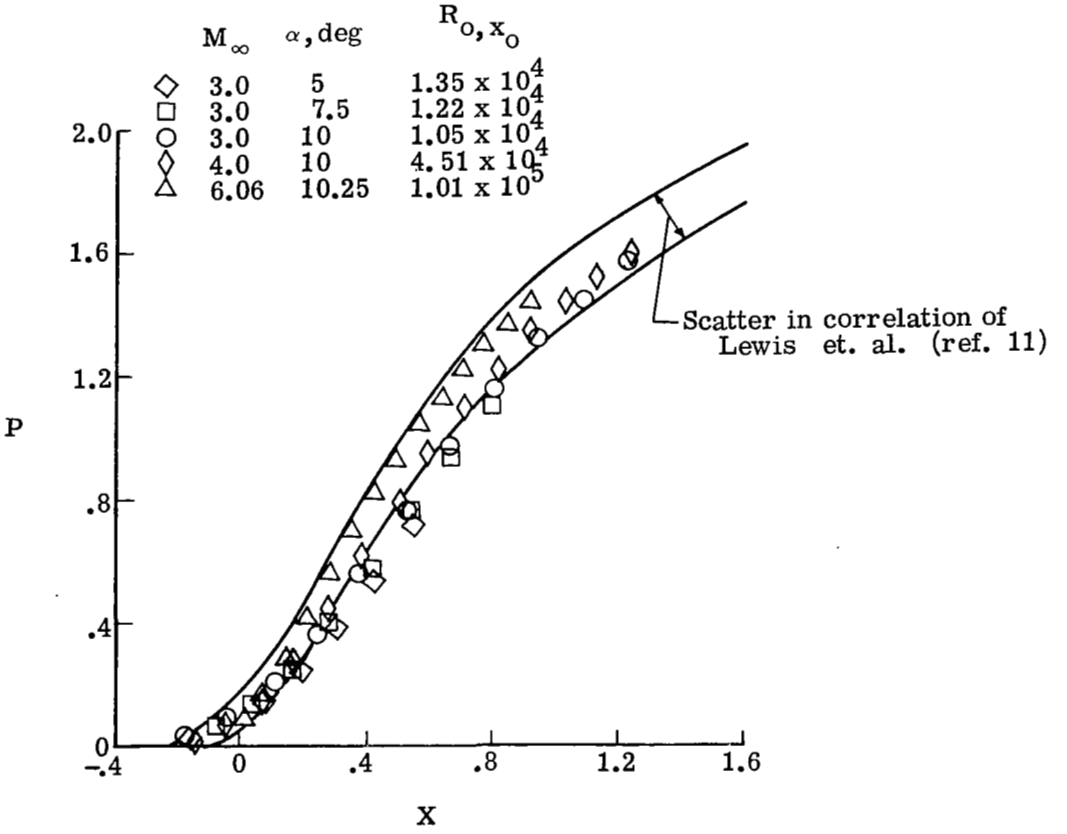

Figure 32.- Comparison of the present numerical results with the free-interaction pressure correlation of Lewis, Kubota, and Lees.

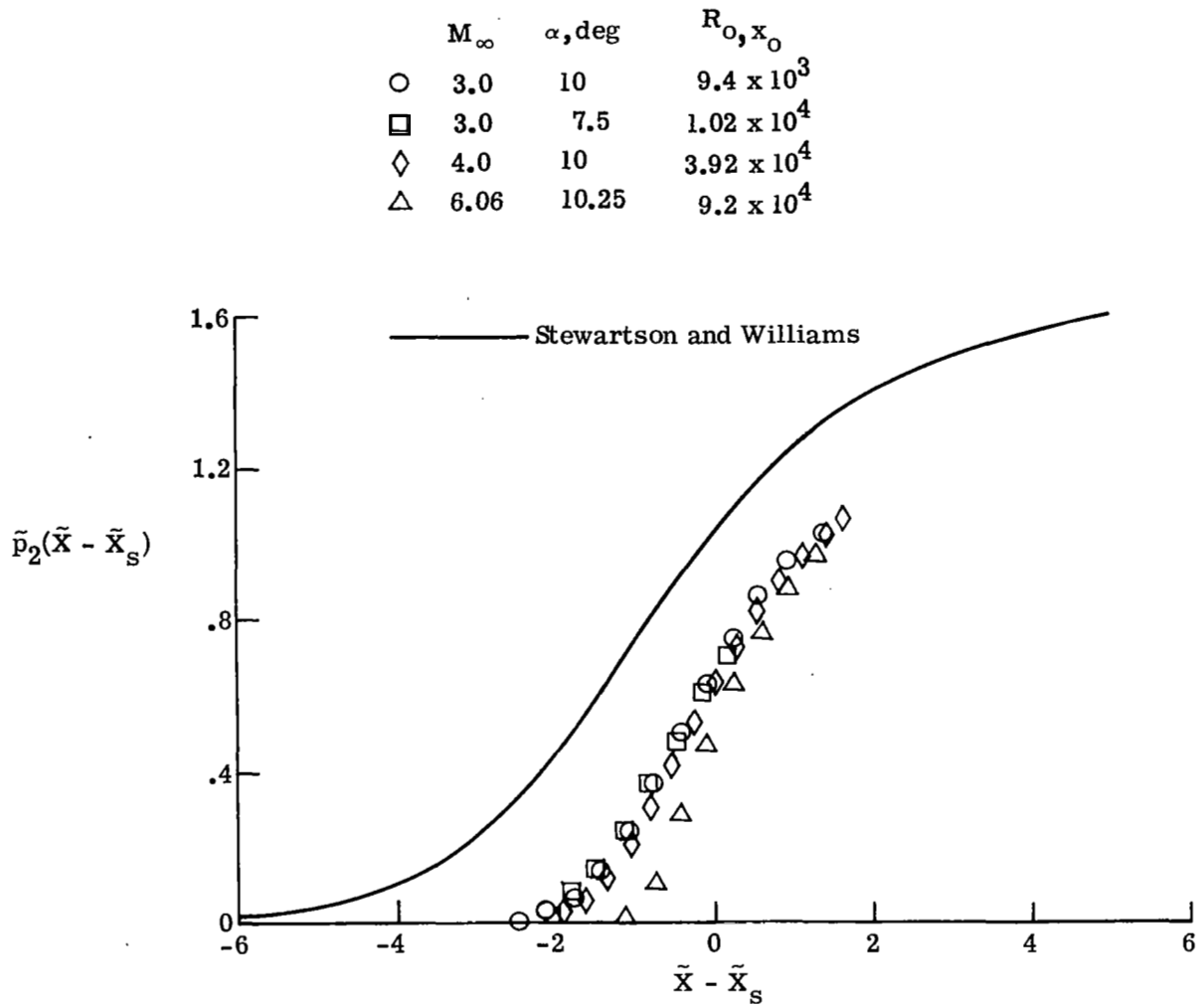

Figure 33.- Comparison of the pressure from the present numerical results with the free-interaction theoretical solution of Stewartson and Williams.

It is seen that the $M_\infty = 3.0$ and $M_\infty = 4.0$ results are well correlated by these coordinates and, as in Curle variables, the $M_\infty = 6.06$ results do not agree with this correlation. This latter result is expected since the Stewartson and Williams free-interaction analysis is also based on a linear pressure-deflection model which becomes inaccurate in hypersonic flow. Comparison of the present results with that of Stewartson and Williams shows that the pressure level is overpredicted by Stewartson and Williams by 20 percent. Also, the present results show a slightly greater slope. Stewartson and Williams (ref. 9), in comparing with the experimental data of Chapman et al. (ref. 10), found differences of comparable magnitude and sign to those found here. The cause of the error was unknown, although they suspected that it was due to the fact that their asymptotic theory is precise only as $\epsilon = R_{\infty,x_0}^{-1/8} \to 0$. Since the relative error is $0(\epsilon)$, the Reynolds number would have to be 10^8 in order for this error to be 0.1.

The correlation variables of Curle differ only in the length scale from those of Stewartson and Williams since it is seen that comparing equations (46) and (51) results in

$$\tilde{p}_2 = 2^{-1/2} P \tag{53}$$

In order to compare the x-scaling given in equations (47) and (52), the present results were replotted with the origin at the start of the interaction and by using the same definition of x_0, that being the point of minimum pressure. The same degree of correlation was obtained with the Curle scaling as that with the Stewartson and Williams scaling; thereby, a preference of these two similarity laws could not be made on the basis of the present results.

CONCLUSIONS

The Brailovskaya finite-difference scheme has been used to obtain steady-state solutions to the Navier-Stokes equations for the laminar, supersonic flow over a flat plate and a compression corner. In the compression-corner calculations, flows with and without separation were considered as well as the effect of wall suction in reducing flow separation. Comparison of the calculated results have been made with experimental data and with other theoretical solutions. In addition, numerical tests were performed to determine the errors introduced by approximate boundary conditions. The following conclusions can be made on the basis of the present investigation:

1. Good agreement between the present results and those from experiment for the compression-corner flow field indicates that the Brailovskaya method can be used to obtain accurate solutions to the laminar Navier-Stokes equations at high Reynolds numbers.

2. The good agreement between the solutions of the Navier-Stokes equations and similar solutions to the boundary-layer equations indicates that the damping mechanism,

which must be present in all explicit schemes in order to maintain stability, is not of such an extent for the Brailovskaya scheme that it alters the real viscosity effects.

3. Caution must be exercised in using approximate techniques (generally some type of extrapolation is used) to supply unknown boundary conditions. For example, it was found that the use of simple-wave extrapolation in the vicinity of the leading-edge shock resulted in erroneous expansion waves being reflected back into the computational region.

4. The effect of using too coarse a grid and neglecting the slip and temperature jump boundary conditions in the leading-edge region of a flat plate results only in a locally invalid solution. Downstream of this region in the weak-interaction region, good agreement was obtained with the weak-interaction theories of Lees and Probstein, and Kubota and Ko, except for the skin-friction distribution in the comparison with the analysis of Kubota and Ko.

5. Comparison of the present results at a free-stream Mach number of 6.06 with those obtained by Klineberg by an integral method of the boundary-layer equations shows that the integral method predicts a larger interaction region, particularly downstream of the corner.

6. Comparisons of the calculated angles between the dividing streamline and the wall, at separation and reattachment, and those found from equations derived by Oswatitsch, agreed, in general, to within 10 percent.

7. The scaling laws derived by Stewartson and Williams correlated the wall pressure distributions found in the present calculations up to the corner. The universal pressure distribution found numerically by Stewartson and Williams overpredicts the pressure level of this correlation by about 20 percent.

Langley Research Center,
National Aeronautics and Space Administration,
Hampton, Va., June 1, 1972.

APPENDIX A

STABILITY ANALYSIS OF THE FINITE-DIFFERENCE EQUATIONS

A von Neumann stability analysis is presented here of the Brailovskaya finite-difference scheme applied to the Navier-Stokes equations. This finite-difference scheme is explicit and will be conditionally stable provided that it contains a damping mechanism which prevents the growth of short wavelength solutions (on the order of a few grid spacings) to the difference equations. Since the finite-difference scheme is incapable of resolving such phenomena, it is necessary for the growth of such solutions to be retarded. The von Neumann analysis consists of examining different wavelength solutions to the difference equations to establish whether a finite-difference scheme amplifies or damps short wavelength solutions.

This analysis is approximate since only the linearized difference equations are used; however, the resulting stability criterion should be viewed as a necessary condition since the nonlinearities in the equations of motion would presumably enhance rather than retard the amplification of small disturbances. Furthermore, the von Neumann analysis does not take into account instabilities which may arise due to the imposition of certain boundary conditions. Clearly, the sufficiency of the resulting von Neumann stability criterion can only be determined by numerical experimentation.

As discussed by Richtmyer and Morton (ref. 46), the von Neumann condition for the nonconservation form of the governing equations is the same as that for the conservation form. Since the analysis is simpler for the nonconservation form, the following nondimensional system of approximate equations, which may be derived from equations (9) to (12), were considered:

$$\frac{\partial U}{\partial t} + A\frac{\partial U}{\partial x} + B\frac{\partial U}{\partial y} = E\left(\frac{\partial^2 U}{\partial x^2} + \frac{\partial^2 U}{\partial y^2}\right) \tag{A1}$$

where

$$U = \begin{Bmatrix} \rho \\ u \\ v \\ T \end{Bmatrix}$$

$$A = \begin{bmatrix} u & \rho & 0 & 0 \\ \frac{c^2}{\gamma\rho} & u & 0 & \frac{\gamma - 1}{\gamma} \\ 0 & 0 & u & 0 \\ 0 & c^2 & 0 & u \end{bmatrix}$$

$$B = \begin{bmatrix} v & 0 & \rho & 0 \\ 0 & v & 0 & 0 \\ \frac{c^2}{\gamma\rho} & 0 & v & \frac{\gamma - 1}{\gamma} \\ 0 & 0 & c^2 & v \end{bmatrix}$$

$$E = \begin{bmatrix} 0 & 0 & 0 & 0 \\ 0 & \frac{4}{3}\frac{\mu/\rho}{R_\infty} & 0 & 0 \\ 0 & 0 & \frac{4}{3}\frac{\mu/\rho}{R_\infty} & 0 \\ 0 & 0 & 0 & \frac{\gamma\frac{\mu}{\rho}}{N_{Pr}R_\infty} \end{bmatrix}$$

and c denotes the speed of sound given by

$$c = \sqrt{(\gamma - 1)T} \tag{A2}$$

In this system of equations, the viscosity coefficient μ has been assumed to be constant in view of the linearization of the von Neumann analysis. In addition, the mixed derivatives $\frac{\partial^2 v}{\partial x\,\partial y}$ and $\frac{\partial^2 u}{\partial x\,\partial y}$ have been deleted from the x- and y-momentum equations, respectively, and the dissipation function Φ given by

$$\Phi = \frac{4}{3}\mu\left[\left(\frac{\partial u}{\partial x}\right)^2 + \left(\frac{\partial u}{\partial x}\right)\left(\frac{\partial v}{\partial y}\right) + \left(\frac{\partial v}{\partial y}\right)^2\right] + \mu\left(\frac{\partial u}{\partial y} + \frac{\partial v}{\partial x}\right)^2 \tag{A3}$$

has been deleted from the energy equation. These last two approximations are based on an analysis by Kentzer (ref. 47) which showed that neither mixed derivatives nor terms quadratic in first-order derivatives enter into the linear stability consideration.

Application of the Brailovskaya scheme (16) to equation (A1) results in the following difference equation where the two steps have been combined by assuming that the coefficient matrices A, B, and E are constant:

$$U_{j,k}^{n+1} = U_{j,k}^{n} - \frac{A\,\Delta t}{2\,\Delta x}\left(U_{j+1,k}^{n} - U_{j-1,k}^{n}\right) + \left(\frac{A\,\Delta t}{2\,\Delta x}\right)^2\left(U_{j+2,k}^{n} - 2U_{j,k}^{n} + U_{j-2,k}^{n}\right)$$

$$+ \frac{AB\,\Delta t^2}{2\,\Delta x\,\Delta y}\left(U_{j+1,k+1}^{n} - U_{j+1,k-1}^{n} - U_{j-1,k+1}^{n} + U_{j-1,k-1}^{n}\right)$$

$$- \frac{AE\,\Delta t^2}{2\,\Delta x^3}\left(U_{j+2,k}^{n} - 2U_{j+1,k}^{n} + 2U_{j-1,k}^{n} - U_{j-2,k}^{n}\right)$$

$$- \frac{AE\,\Delta t^2}{2\,\Delta x\,\Delta y^2}\left(U_{j+1,k+1}^{n} - 2U_{j+1,k}^{n} + U_{j+1,k-1}^{n} - U_{j-1,k+1}^{n} + 2U_{j-1,k}^{n} - U_{j-1,k-1}^{n}\right)$$

$$- \frac{B\,\Delta t}{2\,\Delta y}\left(U_{j,k+1}^{n} - U_{j,k-1}^{n}\right) + \left(\frac{B\,\Delta t}{2\,\Delta y}\right)^2\left(U_{j,k+2}^{n} - 2U_{j,k}^{n} + U_{j,k-2}^{n}\right)$$

$$- \frac{BE\,\Delta t^2}{2\,\Delta y^3}\left(U_{j,k+2}^{n} - 2U_{j,k+1}^{n} + 2U_{j,k-1}^{n} - U_{j,k-2}^{n}\right)$$

$$- \frac{BE\,\Delta t^2}{2\,\Delta y\,\Delta x^2}\left(U_{j+1,k+1}^{n} - 2U_{j,k+1}^{n} + U_{j-1,k+1}^{n} - U_{j+1,k-1}^{n} + 2U_{j,k-1}^{n} - U_{j-1,k-1}^{n}\right)$$

$$+ \frac{E\,\Delta t}{\Delta x^2}\left(U_{j+1,k}^{n} - 2U_{j,k}^{n} + U_{j-1,k}^{n}\right) + \frac{E\,\Delta t}{\Delta y^2}\left(U_{j,k+1}^{n} - 2U_{j,k}^{n} + U_{j,k-1}^{n}\right) \tag{A4}$$

Substitution of one Fourier component of the solution

$$U(x,y,t) = U_0(t)\exp\left[i\left(k_1 x + k_2 y\right)\right] \tag{A5}$$

into equation (A4) gives the amplification matrix, which is defined as $U_{j,k}^{n+1} = GU_{j,k}^{n}$

$$G = I - \left(C^2 + 2D\right) - iC(I - 2D) \tag{A6}$$

where

$$C = \Delta t\left(\frac{A \sin\alpha}{\Delta x} + \frac{B \sin\beta}{\Delta y}\right) \tag{A7}$$

$$D = E\,\Delta t\left(\frac{1 - \cos\alpha}{\Delta x^2} + \frac{1 - \cos\beta}{\Delta y^2}\right) \tag{A8}$$

$$\left.\begin{aligned} \alpha &= k_1\,\Delta x \\ \beta &= k_2\,\Delta y \\ i &= \sqrt{-1} \end{aligned}\right\} \tag{A9}$$

and I is the identity matrix. The coefficients k_1 and k_2 denote Fourier components of the solution to the difference equations.

In the present application of the Brailovskaya scheme, calculations are made outside of the viscous regions and hence stability must be maintained independent of the magnitude of D. By setting D = 0, equation (A6) becomes

$$G = I - C^2 - iC \tag{A10}$$

If μ is an eigenvalue of C, the corresponding eigenvalue of G is

$$g = 1 - \mu^2 - i\mu \tag{A11}$$

The von Neumann necessary condition for stability requires that the magnitude of the eigenvalues of the amplification matrix be less than one, that is,

$$|g|^2 = 1 - \mu^2(1 - \mu^2) \leq 1 \tag{A12}$$

which will be satisfied provided $\mu^2 \leq 1$. Hence, the maximum eigenvalue of the matrix C determines the maximum allowable time increment Δt. Richtmyer (ref. 27) introduced a simple technique by which the eigenvalues of C may be found. Consider an axis inclined at an angle θ with respect to the x-axis where θ is given by

$$\cos\theta = \frac{\dfrac{\sin\alpha}{\Delta x}}{\sqrt{\left(\dfrac{\sin\alpha}{\Delta x}\right)^2 + \left(\dfrac{\sin\beta}{\Delta y}\right)^2}} \tag{A13}$$

$$\sin\theta = \frac{\dfrac{\sin\beta}{\Delta y}}{\sqrt{\left(\dfrac{\sin\alpha}{\Delta x}\right)^2 + \left(\dfrac{\sin\beta}{\Delta y}\right)^2}} \tag{A14}$$

and the velocity component u' along this axis is

$$u' = u\cos\theta + v\sin\theta \tag{A15}$$

By use of equations (A13) to (A15), matrix C may be written as

$$C = \Delta t\sqrt{\left(\frac{\sin\alpha}{\Delta x}\right)^2 + \left(\frac{\sin\beta}{\Delta y}\right)^2}\begin{bmatrix} u' & \rho\cos\theta & \rho\sin\theta & 0 \\ \frac{c^2\cos\theta}{\gamma\rho} & u' & 0 & \frac{\gamma-1}{\gamma}\cos\theta \\ \frac{c^2\sin\theta}{\gamma\rho} & 0 & u' & \frac{\gamma-1}{\gamma}\sin\theta \\ 0 & c^2\cos\theta & c^2\sin\theta & u' \end{bmatrix} \tag{A16}$$

whose eigenvalues are easily found to be

$$\mu = \Delta t\sqrt{\left(\frac{\sin\alpha}{\Delta x}\right)^2 + \left(\frac{\sin\beta}{\Delta y}\right)^2}\begin{Bmatrix} u' \\ u' \\ u' - c \\ u' + c \end{Bmatrix} \tag{A17}$$

By inserting equation (A15) for u', the stability criterion becomes

$$\left\{\Delta t\left[\frac{u\sin\alpha}{\Delta x} + \frac{v\sin\beta}{\Delta y} \pm c\sqrt{\left(\frac{\sin\alpha}{\Delta x}\right)^2 + \left(\frac{\sin\beta}{\Delta y}\right)^2}\right]\right\}^2 \leqq 1 \tag{A18}$$

which results in the following maximum allowable value for Δt:

$$\Delta t \leqq \frac{1}{\frac{|u|}{\Delta x} + \frac{|v|}{\Delta y} + c\sqrt{\left(\frac{1}{\Delta x}\right)^2 + \left(\frac{1}{\Delta y}\right)^2}} \tag{A19}$$

An approximate viscous stability criterion may be derived by neglecting the convection terms in the Navier-Stokes equations. This approximation is reasonable since, as shown by Carter (ref. 18) for Burger's equation, the viscous stability criterion was found to be insensitive to the magnitude of the inviscid terms. Setting C equal to zero in equation (A6) results in

$$G = I - 2D \tag{A20}$$

If g is an eigenvalue of G, then there results

$$g = 1 - 2\varphi \tag{A21}$$

where φ are the eigenvalues of D and are

$$\varphi = \Delta t\left(\frac{1 - \cos\alpha}{\Delta x^2} + \frac{1 - \cos\beta}{\Delta y^2}\right)\left\{\begin{array}{c} 0 \\ \frac{4}{3}\frac{\mu/\rho}{R_\infty} \\ \frac{4}{3}\frac{\mu/\rho}{R_\infty} \\ \frac{\gamma\frac{\mu}{\rho}}{N_{Pr}R_\infty} \end{array}\right\} \tag{A22}$$

the maximum of which is the fourth value since for gases $\frac{\gamma}{N_{Pr}} > \frac{4}{3}$. The von Neumann necessary condition for stability requires $|g| \leqq 1$ which results in $\varphi \leqq 1$ or

$$\Delta t \leqq \frac{0.5N_{Pr}R_{\infty,L}}{\gamma\frac{\mu}{\rho}\left(\frac{1}{\Delta x^2} + \frac{1}{\Delta y^2}\right)} \tag{A23}$$

The calculations were made with the minimum Δt of that given by equation (A19) or (A23). In most cases, equation (A19), which is the CFL (Courant-Friedrichs-Lewy) condition, gave the smallest Δt since the Reynolds number was usually large. In those cases in which the viscous stability criterion was used, a stable calculation resulted thereby suggesting that the approximation made in finding the viscous stability criterion is valid.

APPENDIX B

FINITE-DIFFERENCE EQUATIONS ALONG COORDINATE SYSTEM INTERFACE

Figure 34 shows a typical computational module centered at point 0 along the interface between a rectangular and skewed coordinate system. The grid spacing is variable

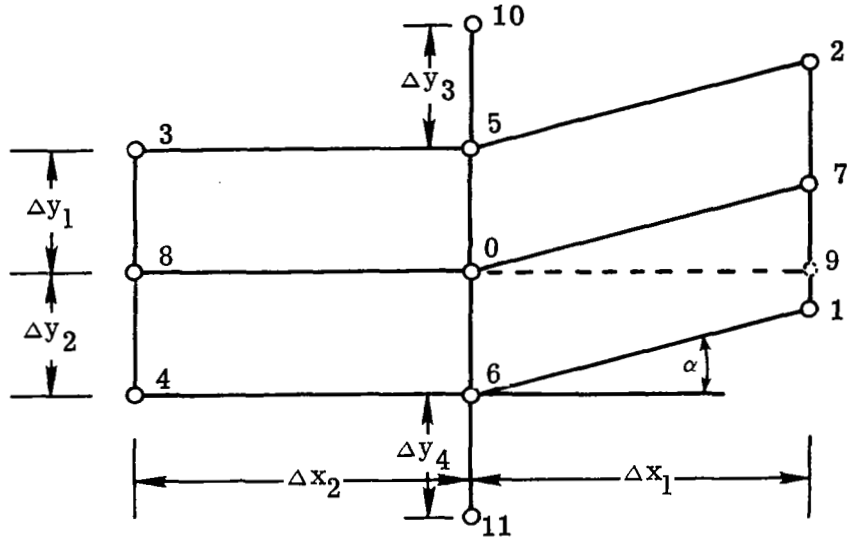

Figure 34.- Computational module along coordinate system interface.

in the x- and y-directions. Taylor series expansions about the central point to the neighboring points results in the following second-order difference expressions:

$$\left.\frac{\partial \varphi}{\partial x}\right|_o = \frac{1}{\Delta x_1 \, \Delta x_2 (\Delta x_1 + \Delta x_2)} \left[\Delta x_2^2 \left(\varphi_7 - \Delta x_1 \tan \alpha \left.\frac{\partial \varphi}{\partial y}\right|_o - \Delta x_1^2 \tan \alpha \left.\frac{\partial^2 \varphi}{\partial x \, \partial y}\right|_o \right.\right.$$

$$\left.\left. - \frac{1}{2}(\Delta x_1 \tan \alpha)^2 \left.\frac{\partial^2 \varphi}{\partial y^2}\right|_o \right) - \Delta x_1^2 \varphi_8 + \left(\Delta x_1^2 - \Delta x_2^2\right)\varphi_o \right] + 0(\Delta)^2 \qquad \text{(B1)}$$

$$\left.\frac{\partial^2 \varphi}{\partial x \, \partial y}\right|_o = \frac{\Delta x_2^2 \left.\frac{\partial \varphi}{\partial y}\right|_9 - \Delta x_1^2 \left.\frac{\partial \varphi}{\partial y}\right|_8 + \left(\Delta x_1^2 - \Delta x_2^2\right)\left.\frac{\partial \varphi}{\partial y}\right|_o}{\Delta x_1 \, \Delta x_2 (\Delta x_1 + \Delta x_2)} + 0\left(\Delta^2\right) \qquad \text{(B2)}$$

where

$$\left.\frac{\partial \varphi}{\partial y}\right|_9 = \frac{(b_o - a_o)\varphi_2 - (a_o + b_o)\varphi_1 + 2a_o\varphi_7 - (b_o a_1 - a_o b_1)\left.\frac{\partial^3 \varphi}{\partial y^3}\right|_9}{(b_o - a_o)\Delta y_1 + (a_o + b_o)\Delta y_2} + 0\left(\Delta^3\right)$$

$$
\left.
\begin{aligned}
a_o &= \frac{\Delta y_1^2 - \Delta y_2^2 + 2\,\Delta x_1 \tan\alpha(\Delta y_1 + \Delta y_2)}{2} \\
b_o &= \frac{\Delta y_1^2 + \Delta y_2^2 + 2\,\Delta x_1 \tan\alpha(\Delta y_1 - \Delta y_2)}{2} \\
a_1 &= \frac{\Delta y_1^3 + \Delta y_2^3 + 3\,\Delta x_1 \tan\alpha(\Delta y_1^3 - \Delta y_2^3) + 3\,\Delta x_1 \tan^2\alpha(\Delta y_1 + \Delta y_2)}{6} \\
b_1 &= \frac{\Delta y_1^3 - \Delta y_2^3 + 3\,\Delta x_1 \tan\alpha(\Delta y_1^2 + \Delta y_2^2) + 3\,\Delta x_1^2 \tan^2\alpha(\Delta y_1 - \Delta y_2)}{6}
\end{aligned}
\right\} \quad \text{(B3)}
$$

$$
\left.\frac{\partial^2\varphi}{\partial x^2}\right|_o = \frac{\Delta x_2\varphi_9 - (\Delta x_1 + \Delta x_2)\varphi_o + \Delta x_1\varphi_8}{\frac{\Delta x_1\,\Delta x_2}{2}(\Delta x_1 + \Delta x_2)} - \left(\frac{\Delta x_1 - \Delta x_2}{6}\right)\frac{\partial^3\varphi}{\partial x^3} + 0(\Delta^2) \quad \text{(B4)}
$$

where

$$
\begin{aligned}
\varphi_9 = \frac{1}{B_1\,\Delta y_1 + A_1\,\Delta y_2}\Bigg\{ & B_1\Big[(\Delta y_1 + \Delta x_1 \tan\alpha)\varphi_7 - \Delta x_1 \tan\alpha\,\varphi_2\Big] \\
& + A_1\Big[(\Delta y_2 - \Delta x_1 \tan\alpha)\varphi_7 + \Delta x_1 \tan\alpha\,\varphi_1\Big] \\
& + (A_2B_1 + A_1B_2)\left.\frac{\partial^3\varphi}{\partial y^2}\right|_9\Bigg\} + 0(\Delta^4)
\end{aligned}
$$

where

$$
\left.
\begin{aligned}
A_1 &= \frac{\Delta y_1\,\Delta x_1 \tan\alpha}{2}(\Delta y_1 + \Delta x_1 \tan\alpha) \\
B_1 &= \frac{\Delta y_2\,\Delta x_1 \tan\alpha}{2}(\Delta y_2 - \Delta x_1 \tan\alpha) \\
A_2 &= \frac{\Delta y_1\,\Delta x_1 \tan\alpha}{6}(\Delta y_1 + \Delta x_1 \tan\alpha)(\Delta y_1 + 2\,\Delta x_1 \tan\alpha) \\
B_2 &= \frac{\Delta y_2\,\Delta x_1 \tan\alpha}{6}(\Delta y_2 - \Delta x_1 \tan\alpha)(\Delta y_2 - 2\,\Delta x_1 \tan\alpha)
\end{aligned}
\right\} \quad \text{(B5)}
$$

The dependent variable φ represents any of the flow variables ρ, u, v, or T. In equations (B1) to (B5), the terms $\left.\frac{\partial\varphi}{\partial y}\right|_0$, $\left.\frac{\partial\varphi}{\partial y}\right|_8$, and $\left.\frac{\partial^2\varphi}{\partial y^2}\right|_0$ are approximated by the usual three-point difference equations given by equations (22) and (23), respectively. The term $\left.\frac{\partial^3\varphi}{\partial y^3}\right|_9$ needs only to be approximated to first order,

$$\left.\frac{\partial^3\varphi}{\partial y^3}\right|_9 = \left.\frac{\partial^3\varphi}{\partial y^3}\right|_0 + 0(\Delta)$$

To evaluate $\left.\frac{\partial^3\varphi}{\partial y^3}\right|_0$ to first order, four points are required, which causes a minor dilemma as to which four points to use. The scheme used here is a weighted combination of difference expressions obtained from two different staggered sets of points,

$$\left.\frac{\partial^3\varphi}{\partial y^3}\right|_0 = (1 - \beta)\left.\overline{\frac{\partial^3\varphi}{\partial y^3}}\right|_0 + \beta \left.\overline{\overline{\frac{\partial^3\varphi}{\partial y^3}}}\right|_0$$

where β is a weighting factor which varies linearly from zero at the wall to unity at the outer boundary of the computational box, and

$$\left.\overline{\frac{\partial^3\varphi}{\partial y^3}}\right|_0 = \frac{N_1}{D_1}$$

$$N_1 = d_o\,\Delta y_1\varphi_{10} - \left[d_o(\Delta y_1 + \Delta y_3) + c_o\,\Delta y_2\right]\varphi_5 - c_o\,\Delta y_1\varphi_6 + \left[d_o\,\Delta y_3 + c_o(\Delta y_1 + \Delta y_2)\right]\varphi_o$$

$$D_1 = d_o\,\frac{\Delta y_1(\Delta y_1 + \Delta y_3)}{6}\left[(\Delta y_1 + \Delta y_3)^2 - \Delta y_1^2\right] - c_o\,\frac{\Delta y_1\,\Delta y_2}{6}\left(\Delta y_1^2 - \Delta y_2^2\right) \qquad \text{(B6)}$$

with

$$c_o = \frac{\Delta y_3}{2}(\Delta y_1 + \Delta y_3)$$

$$d_o = \frac{\Delta y_2}{2}(\Delta y_1 + \Delta y_2)$$

(Equations continued on next page)

$$\left.\begin{aligned}
&\left.\frac{\overline{\overline{\partial^3 \varphi}}}{\partial y^3}\right|_o = \frac{N_2}{D_2} \\
&N_2 = -g_o\,\Delta y_2 \varphi_{11} + \left[g_o\left(\Delta y_2 + \Delta y_4\right) + f_o\,\Delta y_1\right]\varphi_6 + f_o\,\Delta y_2 \varphi_5 \\
&\qquad - \left[f_o\left(\Delta y_1 + \Delta y_2\right) + g_o\,\Delta y_4\right]\varphi_o \\
&D_2 = \frac{g_o\,\Delta y_2\left(\Delta y_2 + \Delta y_4\right)}{6}\left[\left(\Delta y_2 + \Delta y_4\right)^2 - \Delta y_2^2\right] + \frac{f_o\,\Delta y_1\,\Delta y_2}{6}\left(\Delta y_1^2 - \Delta y_2^2\right)
\end{aligned}\right\} \qquad \text{(B7)}$$

with

$$f_o = \frac{\Delta y_4}{2}\left(\Delta y_2 + \Delta y_4\right)$$

$$g_o = \frac{\Delta y_1}{2}\left(\Delta y_1 + \Delta y_2\right)$$

REFERENCES

1. Van Dyke, Milton: Higher-Order Boundary-Layer Theory. Annual Review of Fluid Mechanics, Vol. 1, William R. Sears and Milton Van Dyke, eds., Annual Reviews, Inc., 1969, pp. 265-292.

2. Brailovskaya, I. Yu.: A Difference Scheme for Numerical Solution of the Two-Dimensional, Nonstationary Navier-Stokes Equations for a Compressible Gas. Sov. Phys. – Doklady, vol. 10, no. 2, Aug. 1965, pp. 107-110.

3. Crocco, Luigi: A Suggestion for the Numerical Solution of the Steady Navier-Stokes Equations. AIAA J., vol. 3, no. 10, Oct. 1965, pp. 1824-1832.

4. Lees, Lester; and Reeves, Barry L.: Supersonic Separated and Reattaching Laminar Flows: I. General Theory and Application to Adiabatic Boundary Layer/Shock-Wave Interactions. AIAA J., vol. 2, no. 11, Nov. 1964, pp. 1907-1920.

5. Nielsen, Jack N.; Goodwin, Frederick K.; and Kuhn, Gary D.: Review of the Method of Integral Relations Applied to Viscous Interaction Problems Including Separation. Viscous Interaction Phenomena in Supersonic and Hypersonic Flow, Univ. of Dayton Press, c.1970, pp. 31-82.

6. Reyhner, T. A.; and Flügge-Lotz, I.: The Interaction of a Shock Wave With a Laminar Boundary Layer. Int. J. Non-Linear Mech., vol. 3, no. 2, June 1968, pp. 173-199.

7. Murphy, John D.: A Critical Evaluation of Analytic Methods for Predicting Laminar-Boundary-Layer Shock-Wave Interaction. Analytic Methods in Aircraft Aerodynamics, NASA SP-228, 1970, pp. 515-539.

8. Hill, William G., Jr.: A Comparison of Theory and Experiment for Laminar Separation Ahead of a Compression Corner at Supersonic and Low Hypersonic Speeds. Res. Dep. Rep. RE-401, Grumman Aerosp. Corp., Dec. 1970.

9. Stewartson, K.; and Williams, P. G.: Self-Induced Separation. Proc. Roy. Soc. London, ser. A, vol. 312, no. 1509, Sept. 2, 1969, pp. 181-206.

10. Chapman, Dean R.; Kuehn, Donald M.; and Larson, Howard K.: Investigation of Separated Flows in Supersonic and Subsonic Streams With Emphasis on the Effect of Transition. NACA Rep. 1356, 1958.

11. Lewis, John E.; Kubota, Toshi; and Lees, Lester: Experimental Investigation of Supersonic Laminar, Two-Dimensional Boundary-Layer Separation in a Compression Corner With and Without Cooling. AIAA J., vol. 6, no. 1, Jan. 1968, pp. 7-14.

12. Gadd, G. E.: A Theoretical Investigation of Laminar Separation in Supersonic Flow. J. Aeronaut. Sci., vol. 24, no. 10, Oct. 1957, pp. 759-771.

13. Lighthill, M. J.: On Boundary Layers and Upstream Influence. II. Supersonic Flows Without Separation. Proc. Roy. Soc. (London), ser. A, vol. 217, no. 1131, May 21, 1953, pp. 478-507.

14. Cheng, S. I.: Numerical Integration of Navier-Stokes Equations. AIAA J., vol. 8, no. 12, Dec. 1970, pp. 2115-2122.

15. Allen, J. S.; and Cheng, S. I.: Numerical Solutions of the Compressible Navier-Stokes Equations for the Laminar Near Wake. Phys. Fluids, vol. 13, no. 1, Jan. 1970, pp. 37-52.

16. Ross, B. B.; and Cheng, S. I.: A Numerical Solution of the Planar Supersonic Near-Wake With Its Error Analysis. Proceedings of the Second International Conference on Numerical Methods in Fluid Dynamics. Vol. 8 of Lecture Notes in Physics, Maurice Holt, ed., Springer-Verlag, 1971, pp. 164-169.

17. Roache, Patrick J.; and Mueller, Thomas J.: Numerical Solutions of Laminar Separated Flows. AIAA J., vol. 8, no. 3, Mar. 1970, pp. 530-538.

18. Carter, James Edward: Numerical Solutions of the Supersonic, Laminar Flow Over a Two-Dimensional Compression Corner. Ph. D. Thesis, Virginia Polytech. Inst. and State Univ., Aug. 1971.

19. Victoria, Keith J.; and Steiger, Martin H.: Exact Solution of the 2-D Laminar Near Wake of a Slender Body in Supersonic Flow at High Reynolds number. IAF Paper 55, Oct. 1970.

20. Batt, Richard G.; and Kubota, Toshi: Experimental Investigation of Laminar Near Wakes Behind 20° Wedges at $M_{\infty} = 6$. AIAA J., vol. 6, no. 11, Nov. 1968, pp. 2077-2083.

21. MacCormack, Robert W.: Numerical Solution of the Interaction of a Shock Wave With a Laminar Boundary Layer. Proceedings of the Second International Conference on Numerical Methods in Fluid Dynamics. Vol. 8 of Lecture Notes in Physics, Maurice Holt, ed., Springer-Verlag, 1971, pp. 151-163.

22. MacCormack, Robert W.: The Effect of Viscosity in Hypervelocity Impact Cratering. AIAA Paper No. 69-354, Apr.-May 1969.

23. Hakkinen, R. J.; Greber, I.; Trilling, L.; and Abarbanel, S. S.: The Interaction of an Oblique Shock Wave With a Laminar Boundary Layer. NASA MEMO 2-18-59W, 1959.

24. Vincenti, Walter G.; and Kruger, Charles H., Jr.: Introduction to Physical Gas Dynamics. John Wiley & Sons, Inc., c.1965.

25. Thommen, H. U.: A Method for the Numerical Solution of the Complete Navier-Stokes Equations for Steady Flows. GDC-ERR-AN733, General Dynamics/Convair, Apr. 1965.

26. Allen, John S., Jr.: Numerical Solutions of the Compressible Navier-Stokes Equations for the Laminar Near Wake in Supersonic Flow. Ph. D. Diss., Princeton Univ., June 1968.

27. Richtmyer, Robert D.: A Survey of Difference Methods for Non-Steady Fluid Dynamics. NCAR Tech. Notes 63-2, Nat. Center Atmos. Res., Aug. 27, 1962.

28. Skoglund, Victor J.; Cole, James K.; and Staiano, Edward F.: Development and Verification of Two-Dimensional Numerical Techniques for Viscous Compressible Flows With Shock Waves. SC-CR-67-2679, Sandia Lab., Aug. 1967.

29. Cebeci, Tuncer; Smith, A. M. O.; and Mosinskis, G.: Calculation of Compressible Adiabatic Turbulent Boundary Layers. AIAA J., vol. 8, no. 11, Nov. 1970, pp. 1974-1982.

30. Burstein, Samuel Z.: Numerical Methods in Multi-Dimensional Shocked Flows. AIAA J., vol. 2, no. 12, Dec. 1964, pp. 2111-2117.

31. McCroskey, W. J.; Bogdonoff, S. M.; and McDougall, J. G.: An Experimental Model for the Sharp Flat Plate in Rarefied Hypersonic Flow. AIAA J., vol. 4, no. 9, Sept. 1966, pp. 1580-1587.

32. Waldman, George D.; and Probstein, Ronald F.: An Analytic Extension of the Shock-Expansion Method. J. Aerosp. Sci., vol. 28, no. 2, Feb. 1961, pp. 119-132.

33. Holden, Michael S.: Boundary-Layer Displacement and Leading Edge Bluntness Effects on Attached and Separated Laminar Boundary Layers in a Compression Corner. Pt. I: Theoretical Study. AIAA J., vol. 8, no. 12, Dec. 1970, pp. 2179-2188.

34. Kurzrock, John W.: Exact Numerical Solutions of the Time-Dependent Compressible Navier-Stokes Equations. CAL Rep. No. AG-2026-W-1, Cornell Aeronaut. Lab., Inc., Feb. 1966.

35. Thommen, Hans U.; and Magnus, Richard J.: Numerical Calculation of Separated Flow Fields. Separated Flows, Pt. 1, AGARD CP No. 4, May 1966, pp. 187-205.

36. Lees, Lester; and Probstein, Ronald F.: Hypersonic Viscous Flow Over a Flat Plate. Rep. No. 195 (Contract AF 33(038)-250), Aeronaut. Eng. Lab., Princeton Univ., Apr. 20, 1952. (Also, Hayes, Wallace D.; and Probstein, Ronald F.: Hypersonic Flow Theory, Academic Press, Inc., 1959, pp. 333-374.)

37. Kubota, Toshi; and Ko, Denny R. S.: A Second-Order Weak Interaction Expansion for Moderately Hypersonic Flow Past a Flat Plate. AIAA J., vol. 5, no. 10, Oct. 1967, pp. 1915-1917.

38. Low, George M.: The Compressible Laminar Boundary Layer With Heat Transfer and Small Pressure Gradient. NACA TN 3028, 1953.

39. Chapman, Dean R.; and Rubesin, Morris W.: Temperature and Velocity Profile in the Compressible Laminar Boundary Layer With Arbitrary Distribution of Surface Temperature. J. Aeronaut. Sci., vol. 16, no. 9, Sept. 1949, pp. 547-565.

40. Callens, E. Eugene, Jr.: A Time-Dependent Approach to Fluid Mechanical Phenomenology. AIAA Paper No. 70-46, Jan. 1970.

41. Lewis, John Eldon: Experimental Investigation of Supersonic Laminar, Two-Dimensional Boundary Layer Separation in a Compression Corner With and Without Cooling. Ph. D. Thesis, California Inst. Technol., 1967.

42. Klineberg, John M.; and Lees, Lester: Theory of Laminar Viscous-Inviscid Interactions in Supersonic Flow. AIAA J., vol. 7, no. 12, Dec. 1969, pp. 2211-2221.

43. Klineberg, John Michael: Theory of Laminar Viscous-Inviscid Interactions in Supersonic Flow. Ph. D. Thesis, California Inst. Technol., 1968. (Available from DDC as AD 671 883.)

44. Oswatitsch, K.: Die Ablösungsbedingung von Grenzschichten. Boundary Layer Research, H. Görtler, ed., Springer-Verlag, 1958, pp. 357-367.

45. Curle, N.: The Effects of Heat Transfer on Laminar-Boundary-Layer Separation in Supersonic Flow. Aeronaut. Quart., vol. XII, pt. 4, Nov. 1961, pp. 309-336.

46. Richtmyer, Robert D.; and Morton, K. W.: Difference Methods for Initial-Value Problems. Second ed., Interscience Publ., c.1967.

47. Kentzer, Cz. P.: Stability of Finite Difference Methods for Time Dependent Navier-Stokes Equations. Fluid Dynamics Transactions, Vol. 4, W. Fiszdon, P. Kucharczyk, and W. J. Prosnak, eds., PWN – Polish Sci. Publ., 1969, pp. 45-51.

"The aeronautical and space activities of the United States shall be conducted so as to contribute . . . to the expansion of human knowledge of phenomena in the atmosphere and space. The Administration shall provide for the widest practicable and appropriate dissemination of information concerning its activities and the results thereof."

—NATIONAL AERONAUTICS AND SPACE ACT OF 1958

NASA SCIENTIFIC AND TECHNICAL PUBLICATIONS

TECHNICAL REPORTS: Scientific and technical information considered important, complete, and a lasting contribution to existing knowledge.

TECHNICAL NOTES: Information less broad in scope but nevertheless of importance as a contribution to existing knowledge.

TECHNICAL MEMORANDUMS: Information receiving limited distribution because of preliminary data, security classification, or other reasons.

CONTRACTOR REPORTS: Scientific and technical information generated under a NASA contract or grant and considered an important contribution to existing knowledge.

TECHNICAL TRANSLATIONS: Information published in a foreign language considered to merit NASA distribution in English.

SPECIAL PUBLICATIONS: Information derived from or of value to NASA activities. Publications include conference proceedings, monographs, data compilations, handbooks, sourcebooks, and special bibliographies.

TECHNOLOGY UTILIZATION PUBLICATIONS: Information on technology used by NASA that may be of particular interest in commercial and other non-aerospace applications. Publications include Tech Briefs, Technology Utilization Reports and Technology Surveys.

Details on the availability of these publications may be obtained from:

SCIENTIFIC AND TECHNICAL INFORMATION OFFICE

NATIONAL AERONAUTICS AND SPACE ADMINISTRATION

Washington, D.C. 20546